Tectonics Observatory

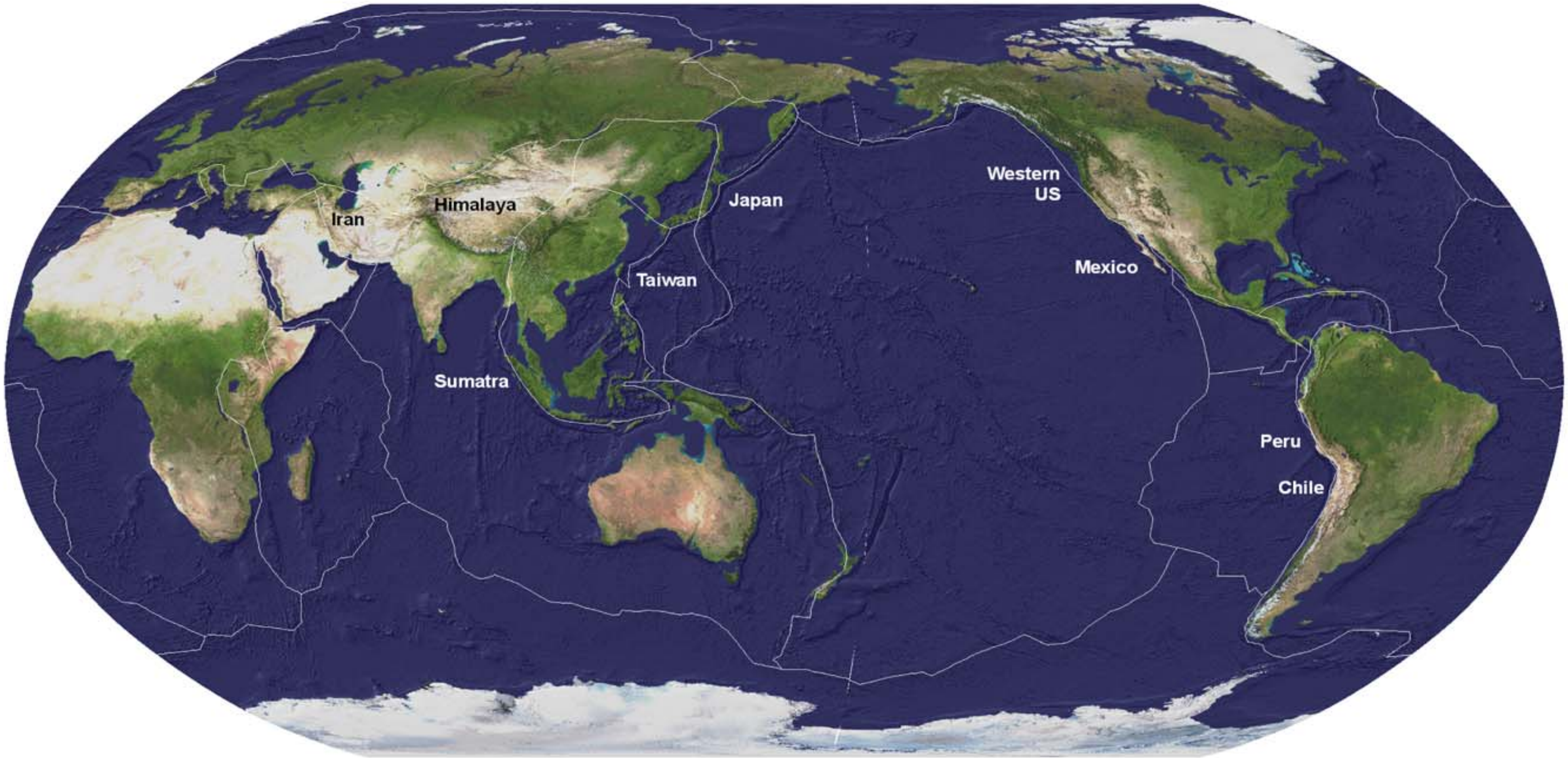

Annual Meeting 2006

Poster Session

^{3}He Cosmogenic Dating in Zircon, Apatite and Titanite

William Amidon[1], Kenneth Farley,[1] Douglas Burbank[2]
1) California Institute of Technology
2) UC Santa Barbara

What is cosmogenic dating?

Cosmogenic isotopes are produced in rock by the interaction of energetic particles with "target" nuclei in the rock. By measuring the abundance of ^{3}He (or ^{10}Be, ^{21}Ne, ^{26}Al, ^{36}Cl), the exposure age of surfaces in the landscape can be calculated.

How does it apply to active tectonics?

Knowing the *age* of surfaces in the landscape allows the calculation of the *rate* at which the surface is deformed by tectonic or erosional processes. This includes; faulted and folded terraces, alluvial fans, offset moraines, bedrock and basin-scale erosion, the age and rate of soil development, and more!

Why develop ^{3}He dating in these phases?

Conventional cosmogenic dating using ^{10}Be, ^{26}Al or ^{36}Cl requires time consuming and expensive preparation, and measurements on an accelerator mass spectrometer. In contrast, ^{3}He is measured cheaply and easily on a noble gas mass spectrometer. Previous use of ^{3}He has been primarily in olivine and pyroxene in volcanic rocks. ^{3}He dating in zircon, apatite and titanite will allow fast, cheap cosmogenic dating of more common rock types.

Our approach...

Our goal is to determine the production rate of ^{3}He in zircon and apatite by direct cross calibration to the known production rate of ^{10}Be in quartz. We separated minerals and measured He in glacial moraine boulders from the Nepal Himalaya, which were previously dated by ^{10}Be.

Methods

1) 5-25 mg of mineral is degassed under vacuum by heating of a platinum packet with a Nd-YAG laser.

2) Gas is purified in a vaccum line before ^{4}He and ^{3}He intensities are measured by peak switching between a faraday cup and an electron multiplier using an MAP-250 noble gas mass spectrometer.

3) ^{3}He Concentrations are calculated by comparison with a He standard.

Analytical concerns

1) **Pressure broadening of the 4He peak**: to address this concern, samples of thorianite (ThO_2) were used to generate high pressures of pure ^{4}He. It was found that the ^{4}He peak was not "tailing" onto the ^{3}He peak at high pressures.

2) **Space-charge effects**: because machine sensitivity is calibrated with standards at low He pressures, it may not reflect the true sensitivity for higher pressures induced by the sample gas. This problem is solved by introducing a "spike" of ^{3}He rich standard during the analysis to evaluate the sensitivity during each analysis.

Previous Work:

Farley et al., 2006 calibrated the production rate of ^{3}He against ^{21}Ne in a Bolviian tuff. A production rate of 80 at/g/yr was found for zircon, 105 at/gyr in apatite and 90 at/g/yr in titanite. These depth profiles show exponential decay of ^{3}He with depth in the rock, confirming a cosmogenic source for the ^{3}He.

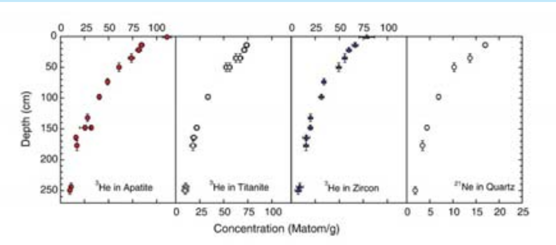

Direct comparison of ^{3}He and ^{10}Be

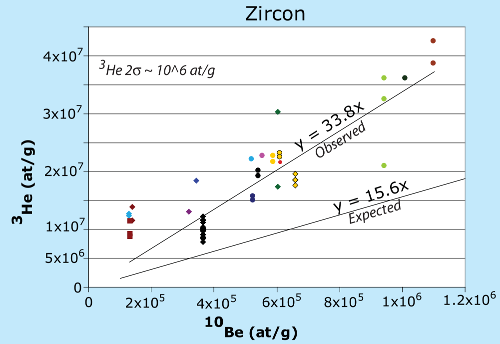

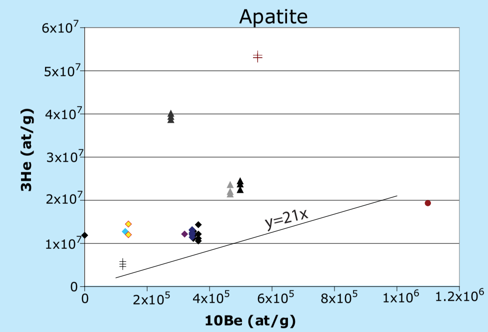

Plotting ^{3}He/^{10}Be against elevation

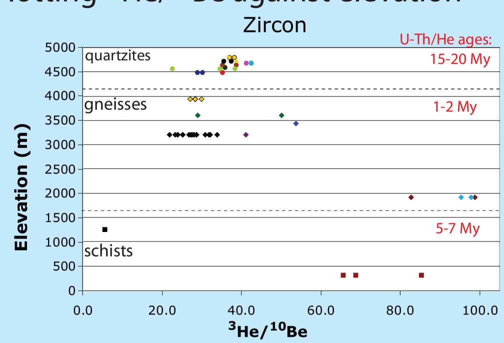

Is overproduction increasing with elevation?

Because ^{3}He and ^{10}Be are both produced by neutron spallation, it has often been assumed that both production rates scale with elevation according to the attenuation length of the fast neutron flux. However, because ^{3}He has a lower energy threshold for spallation reactions, its production rate may scale differently with elevation than ^{10}Be. One possibility is that, because the neutron energy spectrum is more energetic at high elevations and low latitudes, neutrons could engage in a primary spallation event, creating additional lower energy neautrons with enough energy to spall a ^{3}He nucei, but not enough to spall a ^{10}Be nuclei. This production pattern would appear as a lower attenuation length for ^{3}He, similar to that observed by Gayer et al., 2004 who measured cosmogenic ^{3}He in Himalayan garnets and found a pattern similar to what we observe in zircon.

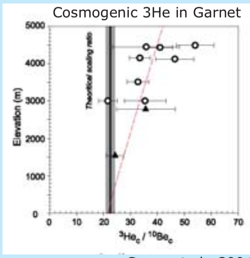

Gayer et al., 2004

Other explanations for overproduction?

It is important to consider non-cosmogenic sources of ^{3}He, produced by a variety of "nucleogenic" reactions, including thermal neutron capture by ^{6}Li:

^{6}Li(n,α)->^{3}H->^{3}He

To evaluate the importance of this reaction, a model was constructed which considers; 1) thermal neutron flux from slowing of fast neutrons near the surface and from radiogenic sources below the surface, 2) the U-Th/He closure age and cosmogenic exposure age of the sample, and 3) Li content in the crystal of interest as well as in the "host" mineral surrounding it. Point 3 is particularly important because ^{3}H produced via ^{6}Li can be injected from a high Li host into the zircon or apatite.

Some Neutron Processes in Rock

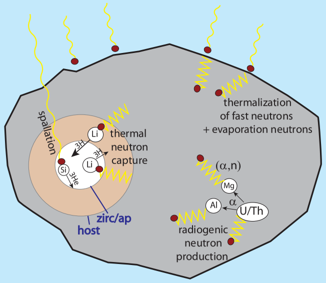

Measuring Li:

Li contents have been measured on apatites using the ICPMS at Caltech. Results show good reproducibility, suggesting Li can be accurately measured by this technique. Observed values range from ~1-3 ppm, with similar or lesser values expected for zircon.

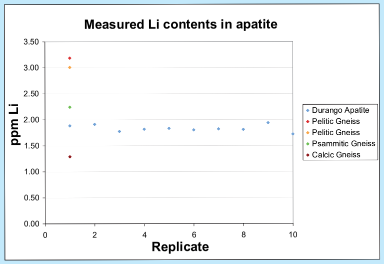

Model Results:

A.

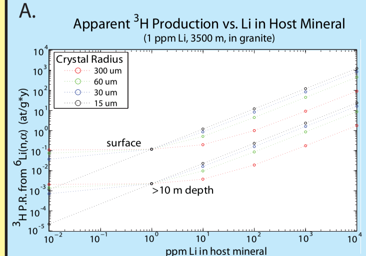

B.

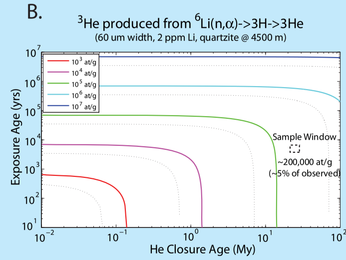

Plot A shows the importance of grain size in determining the production of ^{3}He from ^{6}Li. Production in small grains is dominated by implanted ^{3}He, and is linearly related to Li content in the host. Larger grains have most of their 3He produced internally, and thus the apparent production rate from Li flattens when the host Li content becomes very low. Plot B shows the expected ^{3}He produced from ^{6}Li as a function of exposure age and U-Th/He closure age. This result is for a 1 ppm zircon/apatite embedded in a quartzite at 4500 m, and shows that production from 6Li is <5% of the total observed 3He.

Conclusions and future work:

1) Based on the work of Farley et al., 2006 it appears that this technique is ready to be applied to low-Li samples, in settings outside of Nepal.

2) It is likely that a problem exists with the currently accepted scaling models when applied in the Nepal Himalaya. To confirm this we plan to:
 a) measure Li in more samples of zircon and apatite
 b) explore hand sample petrgraphy to determine "host" minerals
 c) measure 3He and closure age in Li-rich phases to estimate thermal neutron flux in the rock

Sedimentary record of erosion and deformation rates in the northern Tianshan as constrained from magnetostratigraphic sections in the Junggar basin, western China

J. Charreau[1], J.P Avouac[2], Y. Chen[1], K.A. Farley[2], S. Domingez[3], S. Gilder[4]
1. Institut des Sciences de la Terre d'Orléans, France; 2. California Institute of Technology, USA; 3. Université de Montpellier II, France; 4. Institut de

Abstract

The Junggar flexural basin which flank the Tianshan range to the north, has recorded the history of erosion and overthrusting of the range. We combine detailed magnetostratigraphic section from the fold-and-thrust piemont belts, seismic data on subsurface structures and cooling ages from detrital minerals. These data indicate that the flux of sediment eroded from the Tianshan has increased first about 15 ago and again around 11Myr ago to reach a plateau of ~50 km3/Myr (with correction for sediment compaction). Given the area of the Tianshan presently drained by this basins, the sedimentary flux imply erosion rates of the order of 0.3-0.5 mm/yr over the last 10Myr. The uppermost formation in both forelands, the Xiyu formation, consist of a dark coarse gravel often thought to mark the beginning of the Pliocene. This formation is shown to be highly diachronous: the gravel sheet has prograded over the underthrusting forelands at rates of 2.5mm/yr in the north, suggesting a shortening rate across the Central Tianshan (at 83°E) of at most 2.5mm/yr, comparable to the present 3mm/yr shortening rate. Our study shows that the shortening rate across the central Tianshan probably didn't change much over the last 8Myr and that the present tectonic regime was established between about 10 and 12Ma. There is no indication of an increase in sedimentary flux at 4-2Myr, as proposed in some earlier studies and taken to reflect enhanced erosion rates driven by a global climate change. We conclude that the Tianshan may have been reactivated by about 20-24Ma. The sedimentary flux increased by about 15Ma and again by 11Myr, probably reflecting a coeval increase of tectonic rates which lead to the creation of the topography of the modern Tianshan. The 10Myr time lag between the earliest deformation of the range and the increase in sedimentary flux might reflect the time needed to create sufficient topography to enhance surface processes and for the development of the drainage

Introduction

The growth of a mountain range results primarily from crustal thickening driven by horizontal shortening. As mountain grows surface processes become more active and operate mass transfer from the uplifted zone to the flanking lowlands. This transfer depends on climate and topography. Mountain building is therefore a complex process resulting from coupling between tectonic deformation, surface processes and climate. The redistribution of mass at the surface are key factors determining tectonic deformation. In Central Asia the high Tianshan mountains are flanked by the Tarim and the Junggar that are two large closed intracontinental basins where eroded material is shed from the Tianshan. Folding and thrusting along both the northern and southern piedmont have exposed sections of the sediment fill. This setting is particularly appropriate to quantify sediment flux into the basins and analyze the sedimentary record of thrusting.

(1) Kinematic framework

To describe the evolution of the Tianshan range we used the kinematic frame work of Figure 1.
We thus combine (1) structural model of the piedmont and the foreland basin, (2) chronological constraints on the stratigraphy derived from magnetostratigraphic sections of Neogene sediments and (3) thermochronologicals and cosmonucleid dating respectively of detrital grains and actual river sand, to determine:
- sediment flux history Fe
- timing and rate of deformation Vi of the piedmont thrust fault
- erosion rates
- sediment propagation rates Vpr

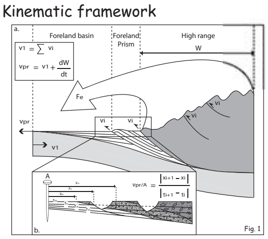

Fig. 1: schematic sketch defining the kinematic framework used in this study; V1 is the underthrusting velocity of the foreland; Vi are the shortenning rates of the various thrust that composed the piedmont and the range; Vpr is the sediment propagation rate in the foreland, Fe is the eroded material flux.

(2) Geological setting and magnetostratigrahy

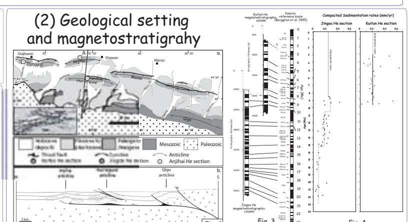

Fig. 2 : (a) geological map of the northern piedmont with localisation of the Kuitun He and the Jingou He section; (b) schematic cross section of the northern piedmont at the Jingou He longitude.
Fig. 3: magnetostratigraphic column of the Jingou He and the Kuitun He section and their correlation to the reference scale.
Fig. 4: Compacted sedimentation rates in the Jingou He and the Kuitun He section deduced from the magnetostratigraphic correlation, 1Tuncertaintie in white.

The Tianshan is a 2500-km-long range with an average altitude of 2500 m with summit up to 7000 m high. The range was originally built during Devonian to Carboniferous. During Oligocene to late Miocene ancient structures were reactivated by the India-Asia collision giving most of the living topography. The main northern Tianshan piedmont is about ~240 km-long from the Urumqi province capital to the Dushanzi city (Fig. 2a). It is constituted by three main rows of thrust fault and fold belt. Folds are mainly fold-bend fault and detachment fold. Folded and faulted sediments in the foreland present a large age span from Permien to Quaternary time and are well exposed along several north-south flowing rivers. But because sediments are mainly continental in origin their ages are poorly constrained. We thus carried out two magnetostratigraphic sections in Neogene sediments in order to better contsraint the sedimentary history related to the reactivation of the range.

(3) Sedimentary flux reconstruction

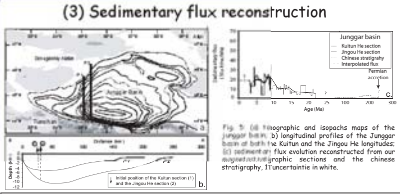

Fig. 5: (a) topographic and isopachs maps of the Junggar basin; (b) longitudinal profiles of the Junggar basin at both the Kuitun and the Jingou He longitudes; (c) sedimentary flux evolution reconstructed from our magnetostratigraphic sections and the chinese stratigraphy, 1Tuncertaintie in white.

Assuming that the relative thickness is uniform throughout the basins the volume Vi above a i layer in the whole basin may be expressed as follow: $v_i = v_O.(z_i/z_O)$.
Where z_i is the true depth of the i layer at a given vertical profile, z_O is the depth of basin basement at the same profile and V_O is the total volume of the basin. Yet, horizontal section along river in the piedmont may be considered as vertical profiles as drill hole. We thus reconstruct the sediment flux accumulation in the Junggar basin based on the stratigraphy constrained by our magnetostratigraphic dating along the two Kuitun and Jingou He sections (Fig. 6c).
We calculated V_O of both the Junggar and the Kuche basin by digitalizing isopachs map of the basement (Fig. 6a) and found a total volume of ~430.10^3 km3. Z_i is obtained from the magnetostratigraphic thickness (giving the depth of the top of the section) and the necessary compaction correction. z_O must be estimated giving the initial position of the sedimentary column before shortening and incorporation within the piedmont (Fig. 6b).

(4) Deformation rates across the Anjihai detachement fold

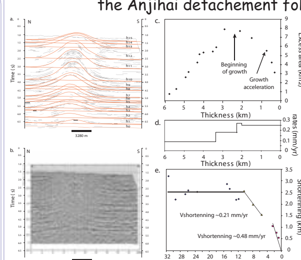

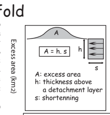

Considering a given deformed horizon of a detachement fold such as the Anjihai anticline (Fig. 6a), one can calculate the 'excess area' (Fig. 6g). between the deformed horizon and its initial geometry obtained by interpolating the horizon linearly across he fold.
Across such detachment fold, in the hypotheses that no bed parallel shear occur, pregrowth strata should be characterized by a linear relationship between excess area and thickness while growth strata should present a non-linear relationship (Fig. 6d).

Fig. 6: (a) line drawing of a seismic line ran arcoss the Anjihai anticline and localisation of the 15 horizons used to calculate the Excess area; (b) original seismic line (from Dengfa et al., 2005); (c) Excess area agianst thikcness of the 15 horizons; (d) sedimentation rates agianst thickness deduced from the magnetostratigraphic correlation; (e) Shortenning across the Anjihai antcline with respect to time, 1Tuncertaintie in white

(6) Preliminary results of U-Th/He thermochronology

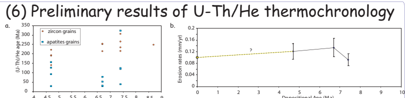

Fig. 8: (a) plot of U-Th/He of detrital grains ages versus depositional ages ; (b) Evolution of the erosion rates deduced from the Lag-time concept with respect to time, yellow circle represent erosion rates calculated from cosmonucleid dating of actual river sand of the Kuitun He river

In order to decipher the late exhumation history of the Tianshan mountains, we carried out U-Th/He dating on both apatite and zircon detrital grains collected in the Kuitun section. Results are summuraized on Figure Xa. From the youngest apatite ages providing the sediment depositional age from our magnetostratigraphic study, we also calculated the erosion rates using the lag-time concept. We found an average rates of ~0.1 mm/yr average

(5) The conglomerate Xiyu formation and its propagation rates

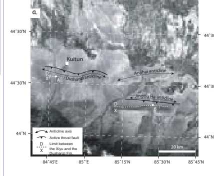

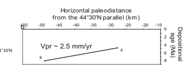

The Cenozoic stratigraphy is characterized by a gradual coarsening upward with the dark conglomerate Xiyu formation at the top underlying the Dushanzi formation. The Xiyu formation is widely distributed along the margin of the Tianshan and have been assigned to be Plio-Pleistocene in age. From our magnetostratigraphic study we found that the basal age of the Xiyu formation at the Jingou He section is ~8.3 Ma in age while at the Kuitun section it is ~4.8 Ma in age. From these basal ages and satelit images analyses, we calculated a propagation rate of sediments Vpr of ~2.5 mm/yr, providing the initial position of the section before shortenning.
We carried out a similar analyses in the south Tianshan that give a propagation rate Vpr of ~6 mm/yr.

Fig. 7: (a) landsat image of the Dushanzi area with localisation of the Kuitun He and the Jingou He section and the limit between the Dushanzi and the Xiyu formation; (b) plot of the basal ages of the Xiyu formation versus the distance from the 44°30'N parallel

Discussion

From the sediment flux reconstruction we believe that, by ~15 Ma and by ~11 Ma, the Tianshan range may have underwent rapid uplift acceleration with a rising topography that is rapidly stabilized as compensated by heightened erosion rates that give higher sediment fluxes delivered to the basin. These ages are consistent with other previous studies carried out in the Tianshan.
Giving the constant sedimentary flux of ~50.10^3 km^3 during the last ~10 Ma, the geometry of the range probably did not significantly change with an equilibrium between erosion and uplift. Thus the area of the Tianshan presently drained by the Junggar basin remains probably the same over the last 10 Myr giving an average erosion rates of ~0.3-0.4 mm/yr. Moreover as the geometry of the range may have been constant, according to our kinematic model the total shortenning accross the range (V1) was of ~2.5 mm/yr during the last ~8 Myr which is consitent with the present day rates of ~3 mm/yr. This reinforces the idea that that the present tectonic regime was established between about 10 and 12Ma.
Some authors have interpreted the Xiyu formation as reflecting directly tectonic uplift (e.g., Zheng et al, 2000) while others assign it to a global effect of climate change on erosion rates (Peizhen et al, 2001). Our interpretation is that this gravel sheet was prograded over the foreland as it was underthrusting beneath the orogenic wedge. We reject the common assumption that these conglomerates would reflect climate change or a particular episode of thrusting and uplift of the Tian Shan.

New constraints on the kinematics of mountain-building in Taiwan.

M. Simoes*, J.P. Avouac, O. Beyssac, B. Goffé, K. Farley, Y.-G. Chen

[Simoes et al, subm. to JGR]

* martine.simoes@univ-rennes1.fr

The Taiwanese range.

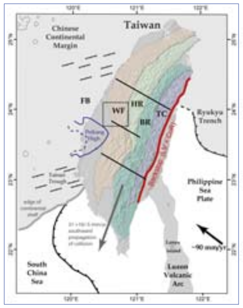

Figure: Geodynamical setting of the arc-continent collision of Taiwan Thick arrow shows the convergence of the Philippine Sea Plate relative to the Chinese Continental Margin predicted from the global plate geodetic model REVEL [Sella, et al., 2002]. Main structural units of Taiwan: CoR: Coastal Range - LV: Longitudinal Valley - TC: Tananao Complex - BR: Backbone Range - HR: Hsueshan Range - WF: Western Foothills - FB: Foreland Basin. Peikang Basement High after [Lin, et al., 2003]. Black lines indicate the three transects investigated by Beyssac *et al* [subm.]. box shows where the kinematics of shortening have been quantified (e.g. Simoes *et al*, 2006).

- Southward propagation of mountain growth
- High rates of deformation and erosion
- Tropical climate

How does the coupling between tectonics, erosion and climate influence mountain-building processes ??

Re-appraising mountain-building in Taiwan: geological data

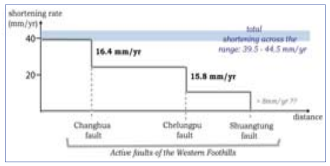

Figure: Long-term horizontal velocity (Simoes *et al*, 2006) and slip on major faults (Simoes *et al*, in press-a; Simoes *et al*, in press-b) relative to the backstop. This indicates that most (if not all) shortening is absorbed on the most frontal faults of the foothills, leaving little (if any) internal shortening within the Central Range. This kinematics holds for the last 2 Myr.

- Shortening localized on the most frontal faults
- Sustained exhumation below HR and TC in the Central Range.

The Taiwan range grows essentially by underplating below the Central Range.

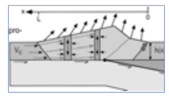

Figure: Schematic view of a critical-wedge growing by frontal accretion, from Willet *et al* (2001). In this case shortening is distributed within the range.

New data on long term evolution of the range: RSCM, (U-TH)/He on Zr (Beyssac *et al*, subm.)

↓

Documents where exhumation (and underplating) occurs

The well-accepted model of a critical-wedge growing by frontal accretion **does not apply** to Taiwan.

↓

New scenario proposed

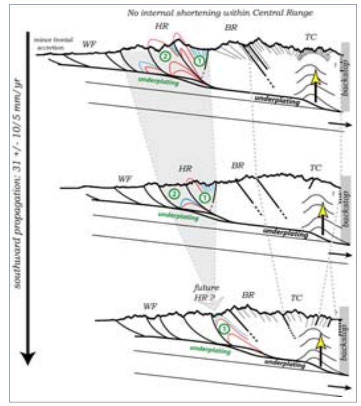

Figure: Kinematics of mountain-building in Taiwan. Shortening is localized on the thrus faults of the foothills (WF) indicating that range growth is sustained by underplating (Simoes et al, 2006). Previous and new constraints on the thermal evolution of the range (e.g. Beyssac *et al*, subm.) indicate that underplating occurs beneath the HR and the TC. These constraints are provided by RSCM thermometry and by LT thermochronology. The three sections are reported on the map to the left.

Results:

Constraints for future investigations on the parameters controlling mountain-building (tectonics, erosion....)

- Fluxes of rocks

Erosion rate averaged over the range: ~3mm/yr

Erosion rates of ~ 4 to 6 mm/yr over HR and TC, but ~0.5 mm/yr over BR where high topography.

only 23 % of the underthrusted crust participates to the range growth.

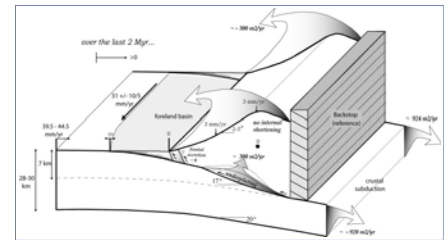

Figure: Sketch summarizing the kinematics of Taiwan quantified in this study. An average erosion rate of 3 mm/yr balances underplating below the internal portions of the range. Only a small portion of the underthrusted crust participates the range growth. The flux of material lost by subduction into te mantle is significant. See also Simoes *et al* (2006). This holds for the last 1.5 to 2 Myr.

- Major readjustments by 1.5 to 2 Myr ago.

To fit both gradient of peak metamorphic temperatures and LT ages over the TC (east Central Range) need to widen the underplating window beneath TC 1.5 - 2 Myr ago.

→ consistent with increase in sedimentation rates in LV basin to the east

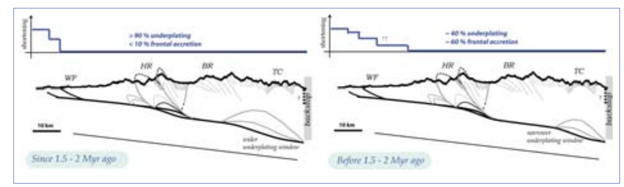

This implies... → changes in the kinematics of deformation
→ changes in the proportion of underplating / frontal accretion

Why ?

- Metamorphism, topography and dynamics of the wedge

Densities predicted for the PT conditions computed in the model can account for the observed topography and Bouguer anomaly.

Kinematics modeled from all available data therefore reflect the internal dynamics of the wedge

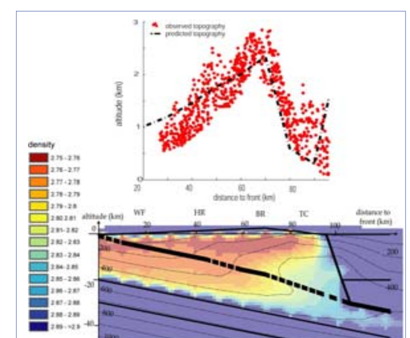

Figure : Predicted densities (bottom) and topography (top) in the case of the northern transect. Densities are calculated after Bousquet *et al* (1997) from the rock composition and from the PT conditions computed in our model. Fine lines indicate the isotherms of the computed thermal structure. The topography is predicted from the distribution of densities by assuming local isostasy and compensation within the asthenosphere (procedures described in Henry *et al* (1997). The observed topography (red dots) is taken within a 30 km wide swath across the northern transect.

Thermo-kinematic modeling

Integration of all available geological constraints with the 2D finite-element code FEAP (Zienkiewicz & Taylor, 1989; Henry *et al*, 1997).

Kinematics prescribed

topography assumed steady state

Not initially prescribed:
- geometry of the basal detachment
- location and width of underplating windows.

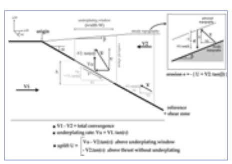

Forward model adjusted to fit RSCM and LT thermochronological data (Beyssac *et al*, subm.)

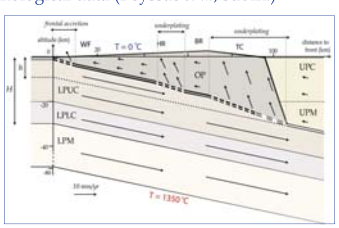

Figure:Geometry of our thermo-kinematic model, with the different domains of homogeneous thermal and kinematic properties: lower plate mantle (LPM), lower plate lower crust (LPLC), lower plate upper crust (LPUC), orogenic prism (OP), upper plate mantle (UPM) and upper plate crust (UPC). The basal decollement is taken as the reference for the velocity field. I is represented by a thick line, which is dashed where the different underplating windows are located. The velocity field computed for the lat 2 Myr is shown. Only the thickness h of the undurthrusted margin is incorporated into the range, the rest is subducted beneath the Philippine Sea plate.

Good fit to all available data along the three transects: model is therefore able to account for the temporal evolution of the range, as seen along-strike

Along a transect, variations in exhumation rates between the different structural units.

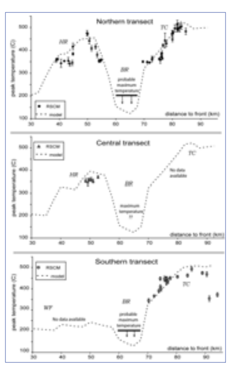

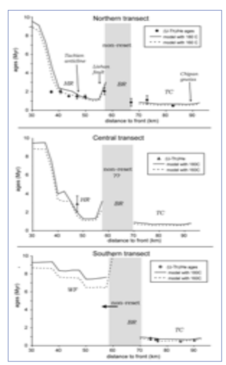

Figure (right) : Peak metamorphic temperatures retrieved from RSCM (Beyssac *et al*, subm) and predicted by our thermo-kinematic model for the three ransects across the range. Observed temperatures below 330 °C within the BR are not reported since this value represents the lower limit of applicability of the method (Beyssac *et al*, 2002). alternatively a probable maximum temperature of ~ 200 °C may be inferred for this area based on the non-resetting of (U-Th)/He ages on detrital zircons (Beyssac *et al*, subm) . Error bars represent a 2-σ interval.

Figure (left): (U-Th)/He ages on detrital zircon (Beyssac *et al*, subm.) with 2-σ error bars, and predictions from our thermo-kinematic model by assuming a closure temperature of 180 and 160 °C. Shaded area indicates where the ages are partially or non- reset over the BR. Where predicted ages are non-reset, no model predictions are shown.

Thermal structure derived for the three transects

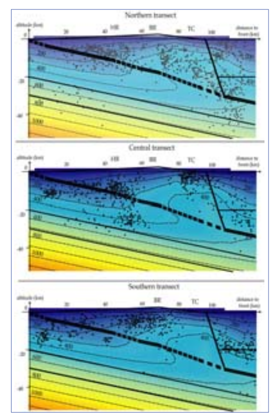

Figure : Predicted thermal structures for the three transects investigated . Temperatures do not change significantly laterally, supporting our 2D approach. Isotherms are represented every 100 °C contour. Also represented is the seismicity from the CWB (Central Weather Bureau) catalog, retrieved along a 30km swath around each one of the three transects. Only earthquakes of magnitudes over 3.5, from 1991 to 2000, have been plotted. No particular structure may be derived from this seismicity to support our derived deep geometry of the Taiwanese range. Interestingly, the seismic gap within the CR coincides quite well with the high topography, mostly for the northern and central transects, as well as with the 350 to 400 °C isotherms. This is also valid over the easternmost boundary of the prism.

The Izu-Bonin-Mariana and Costa Rican Subduction Factories Modeled by GyPSM-S: Evidence for a Low-Viscosity Channel

Laura Baker*, Paula Smith, Michael Gurnis, and Paul Asimow

Tectonics Observatory
California Institute of Technology, Pasadena, CA 91125
**labaker@gps.caltech.edu*

Abstract:

We use GyPSM-S, a model that fully couples the petrological model pHMELTS with ConMan, a 2D thermal and variable viscosity flow model, to describe and compare fundamental processes occurring within the Izu-Bonin-Mariana and Costa Rican subduction zones. By prescribing forcing functions within GyPSM-S we are able to establish the thermal state and phase equilibria of the subducting oceanic slab and adjacent mantle wedge and constrain fluid flux specific to different subduction zones. This allows us to describe the process of hydration of the mantle wedge adjacent to the slab, which leads to the development of a low-viscosity channel. We discuss the impact of the low-viscosity channel on geophysical observables such as dynamic topography and gravity. Also, we define regions of melting, and discuss melt and residue chemistry. This leads to predictions of major and trace element chemistry of arc volcanics.

Parallel computing within the context of GyPSM-S uses a Lagrangian particle distribution to perform thousands of thermodynamically equilibrated calculations during each timestep, allowing for a continuously updating chemical dataset, and a strong feedback mechanism with the fluid dynamics. Allowing the viscosity to be both compositionally and thermally dependent permits a consistent linkage between the effect of water addition to the mantle wedge and the wedge velocity field, leading to large-scale changes in the flow field of the hydrated wedge relative to the anhydrous example and predictions as to the fate of the hydrated material as subduction proceeds. Additionally, we account for chemical feedback in the energy balance by introducing latent heat effects using the isentropic capability of pHMELTS. The flexibility of pHMELTS allows fractional melting to be included and for the calculation of a realistic compositional buoyancy term.

We present four cases, encompassing the Costa Rican and Izu-Bonin-Mariana subduction zones (Southeastern Costa Rica, Central Costa Rica, Northern Izu-Bonin, and Northern Marianas), and compare our model results with geophysical and geochemical observables from these localities. Among these examples, model-specific changes in potential temperature, slab dip, slab thermal age, subduction velocity, and overriding lithospheric thickness allow us to discuss results in a comparative way. The full coupling between the chemistry and the dynamics results in notable behaviors previously unresolved by geodynamic models of subduction. A continuous, slab-adjacent low-viscosity channel defined by hydrous mineral stability and higher concentrations of water in nominally anhydrous minerals develops.

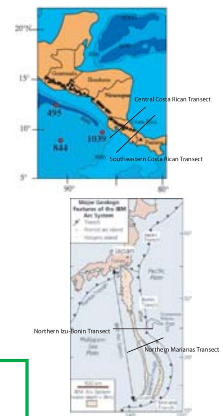

Parallel-computing structure allows thousands of pHMELTS calculations to occur at each iteration:

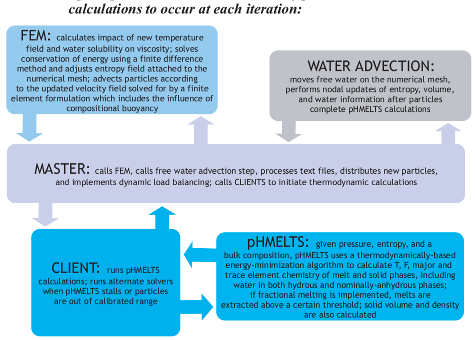

Method:

GyPSM-S (Geodynamic and Petrological Synthesis Model for Subduction) couples two models: ConMan, a 2-D thermal and variable viscosity flow model (King et al., 1990), and pHMELTS, a thermodynamic minimization algorithm for chemical analyses of melts, solids, and water solubility in nominally-anhydrous minerals (via a text-driven interface adiabat_1ph, Smith & Asimow, 2004) with governing Perl scripts. GyPSM-S is built to run in a parallel environment on CITerra.

GyPSM-S is a fully-coupled formulation, whereby iterative transfer of pHMELTS-solved particle data to the finite element nodal mesh resolves the dynamic feedbacks between the dynamics and the chemistry that are unobserved in other, more simplistic models.

The evolution of the pressure-temperature state of the down-going slab produces free water via dehydration reactions as per Hacker et al. (2003). The water is vertically advected and then reacted with surrounding material by a pHMELTS calculation, producing hydrous phases, or an increase in hydrogen concentration in nominally-anhydrous minerals.

Modifications to ConMan include the use of an entropy advection scheme to allow for latent heat effects, as well as a compositional component to the viscosity formulation.

Central Costa Rica:
18 Ma subducting slab age
87.0 mm/yr convergence rate
45 degree slab dip
30 km over-riding lithosphere

SE Costa Rica:
15 Ma subducting slab age
90.0 mm/yr convergence rate
30 degree slab dip
30 km over-riding lithospherer

Northern Izu-Bonin:
135 Ma subducting slab age
50.0 mm/yr convergence rate
45 degree slab dip
20 km over-riding lithosphere

Northern Marianas:
165 Ma subductin slab age
47.5 mm/yr convergence rate
60 degree slab dip
20 km over-riding lithosphere

Low-Viscosity Channel:

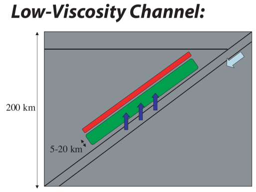

Dehydration reactions within the downgoing slab (in the altered basalt, and serpentinite layers) release free water (Hacker et al. (2003), which rises into the overlying mantle wedge and reacts with the peridotite to form hydrous phases, and to hydrate nominally-anhydrous minerals, such as olivine.

The influence of elevated hydrogen concentrations in olivine on the mantle rheology is to decrease viscosity, an effect accounted for in the coupled formulation (Hirth & Kohlstedt (1996). The relatively thin layer of hydrated nominally-anhydrous minerals is bounded by the slab and the partially-hydrated solidus.

Water rises from the slab, through the hydrated olivine layer (green), and into the hotter mantle wedge, where it crosses its solidus and melts(red). The water is taken up by the melt phase, leading to a low-viscosity channel, of approximate width of tens of kilometers. This hydrated channel will advect with the slab-adjacent material into the deep mantle.

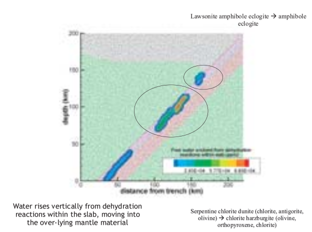

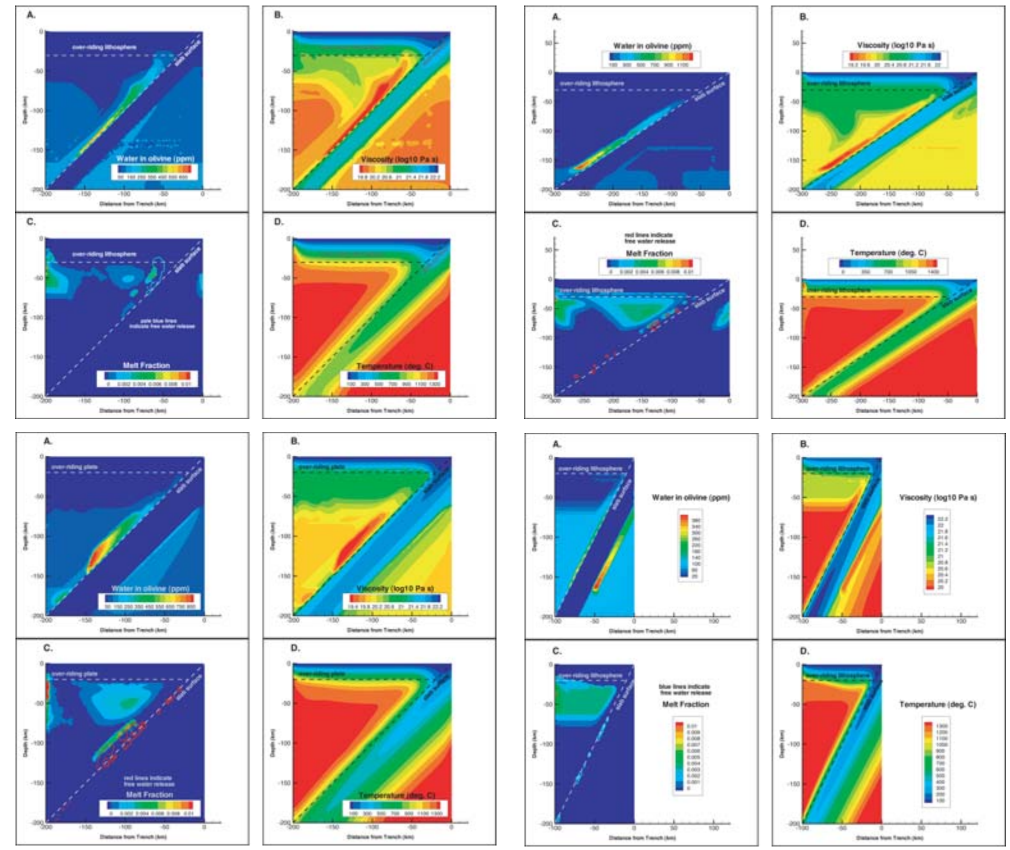

The Costa Rican and Izu-Bonin-Mariana subduction zones: (top left) Central Costa Rica (top right) Southeastern Costa Rica (bottom left) Northern Izu-Bonin (bottom right) Northern Marianas; (A) zone of hydrated nominally-anhydrous minerals defined by elevated water solubility in olivine; (B) lowering of slab-adjacent mantle viscosity due to the chemical dependence in the viscosity formulation; (C) zone of melting, lines indicate the location of free water release from dehydration reactions within the slab; (D) coupled temperature structure.

Conclusions:

GyPSM-S is a powerful, flexible technique that allows for the discovery of new phenomena that can only be observed within the setting of a fully-coupled model integrating both chemistry and dynamics.

The presence of the low-viscosity channel is not a transient feature within subduction zones, being defined by the water release from dehydration reactions and by the partially-hydrated peridotite solidus. It has dynamic implications for evolution of slab dip, as the slab is allowed to decouple from the mantle wedge.

References:

Smith & Asimow (2003); Hacker et al. (2003); Billen & Gurnis (2001); Hirth & Kohlstedt (1996); King et al. (1990); Mosenfelder et al. (2006); Workman & Hart (2005); Ghiorso & Sack (1995)

Elastic versus permanent deformation above the Sunda megathrust

Rich Briggs[1], Willy Amidon[1], Kerry Sieh[1], John Galetzka[1], Bambang Suwargadi[2], Danny Natawidjaja[2], Nugraha Sastra[2], Dudi Prayudi[2]

[1]Tectonics Observatory, Division of Geological and Planetary Sciences, California Institute of Technology
[2]Research Center for Geotechnology, Indonesian Institute of Sciences (LIPI), Bandung, Indonesia.

2005 coseismic uplift measurements

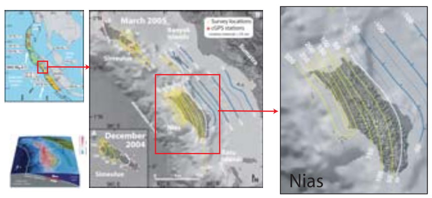

Location of study area and contour map of 2005 coseismic uplift. Notice that on Nias island, the welt of maximum uplift -- 2.5 to 3 m -- runs along the NW coast, while the line of zero uplift is nearly aligned along the east coast.

Geomorphic domains on Nias

Areas in red are < 12 m elevation and roughly correspond to Holocene surfaces. These fringe nearly the entire island.

The blue tint (< 120 m elevation) is at the highest elevation of uplifted reefs on the east coast. Highlighting this elevation illuminates the main geomorphic domains on Nias. The NW corner of the island, nearly all in blue, is low elevation and low relief with relict surfaces and structures, and this area lacks the older uplifted corals observed along the east coast. The southern half of the island in grey is rugged, with high relief associated with active faulting and folding. Note that the southern half of the island has a deeply embayed western coastline.

Anti-correlation of coseismic and long-term uplift?

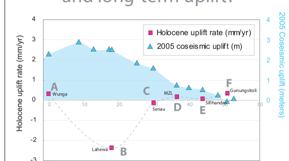

A comparison of coseismic uplift (blue) to Holocene uplift (pink) along a profile across the north of Nias (left) shows that long-term uplift rates do not scale with 2005 coseismic uplift. Rather, maximum uplift in 2005 corresponds to sites that are apparently subsiding in the longer term.

Summary

The 2005 Sunda megathrust rupture provides a rare opportunity to explore the relationship between slip on the megathrust and permanent uplift along the outer arc.

Fossil head at Sifihandro (site E to right)

We compare our measurements of 2005 coseismic uplift (above) to longer term deformation as recorded by Holocene fossil coral reefs on the outer arc island of Nias (right). A reasonable hypothesis might be that long-term deformation mimics the 2005 coseismic signal, such that recent uplift is concentrated along the island's northwest coast. This is not the case, and instead a transect across northern Nias (right) shows that Holocene deformation appears to be nearly anti-correlated with the 2005 uplift pattern. In fact, the region of maximum uplift -- nearly 3 m in 2005 -- appears to have been subsiding during most of the Holocene. And surprisingly, long-term uplift rates are highest on the east coast of the island, where uplift in 2005 was nearly zero.

A survey of Holocene surfaces around the remainder of the island, for which U/Th dates of fossil corals are in progress, confirms that Holocene uplift is concentrated along the east coast of the island, with differential offsets apparent across active upper plate faults. Thus it appears that recent deformation of Nias occurs in two distinct domains. Elastic strain accumulation and release due to 2005-type megathrust ruptures causes very little net uplift, and even subsidence, of the northwest coast. Along the east coast, active faults in the upper plate appear to be responsible for the highest rates of permanent uplift. The partitioning of deformation modes between the northwest (megathrust dominated) and east/southeast (upper plate dominated) is reflected in the gross geomorphology of the island.

Nug measuring and chopping at La'aya (site h to right)

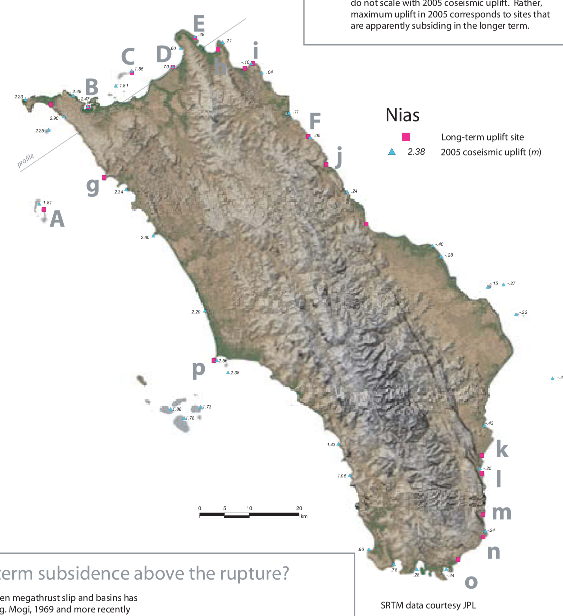

SRTM data courtesy JPL

A complication: the mid-Holocene sea level high

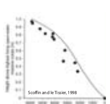

Example of Holocene sea level curve for the Malaysian peninsula

In general, sea level has risen worldwide since ~21 ka due to the melting of glacial ice. But glacial unloading also caused global isostatic adjustments, resulting in a spatially and temporally variable mid-Holocene sea level transgression at lower latitudes.

The timing and magnitude of this sea level high is not well determined for Nias. At present we use model data (right) to apply a correction for the mid-Holocene sea level rise. Our observations so far suggest that the magnitude of the model rise is reasonable, but the timing of the model maximum seems several thousand years too late. At present this is the largest source of uncertainty (at worst, up to 1 m but more typically tens of centimeters) in our uplift measurements.

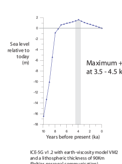

Why long-term subsidence above the rupture?

A correlation between megathrust slip and basins has long been noted (e.g. Mogi, 1969 and more recently Wells et al., 2003 and Song and Simons, 2003) but the causal explanation for this correlation is unclear. It may be that during the long interseismic period of subsidence above the future megathrust rupture, strain accumulation is not entirely elastic and a significant portion of plastic, non-recoverable deformation takes place. This might be through a bulk mechanism such as regional pressure solution. Alternatively, some type of basal erosion may take place coseismically (e.g. von Heune and Scholl, 1991). At right we schematically show the possible interplay of shortening along brittle upper fault structures and subsidence controlled by the earthquake cycle on the megathrust.

Do splay faults plus megathrust ruptre explain the uplift pattern?

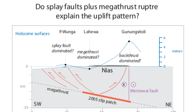

Funded by the National Science Foundation and a grant from The Gordon and Betty Moore Foundation to the Tectonics Observatory, California Institute of Technology

Topographic profiles of uplifted Holocene surfaces

We compare uplifted fossil coral heads, which are reliable recorders of paleo-low tide, to present-day low tide to determine total apparent uplift. From this raw number we subtract 2005 coseismic uplift, and also the appropriate mid-Holocene sea level transgression to calculate net tectonic uplift. U/Th dates of the uplifted corals allow us to calculate uplift rates. All profiles below show raw uplift values. Locations on Nias are shown on the map at left.

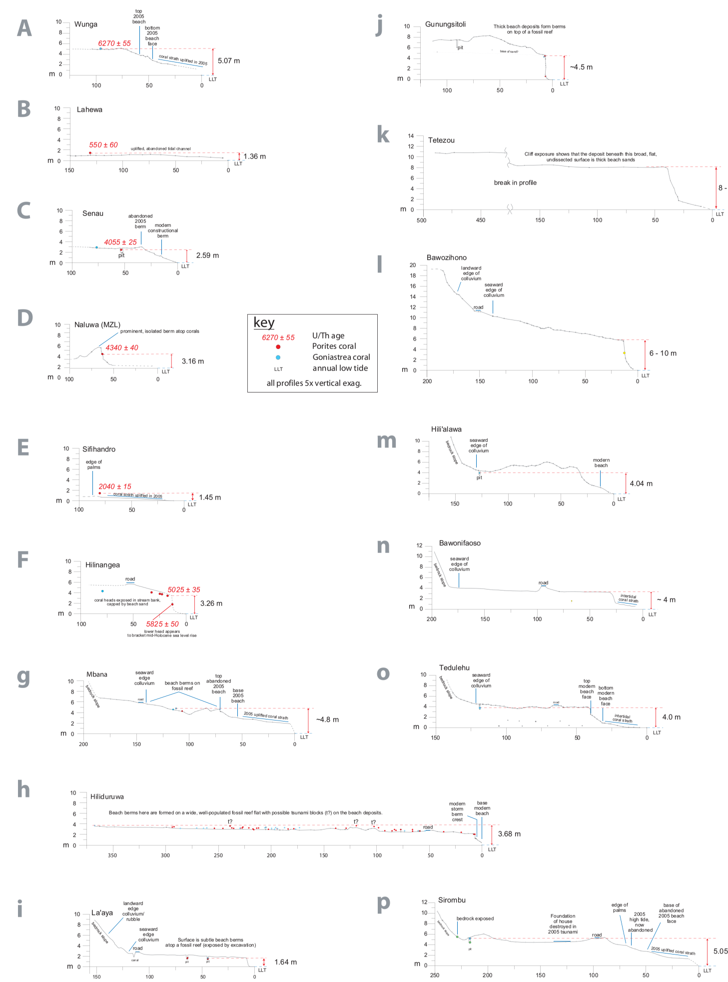

The origin of high-Ca annuli in garnets from the Rand schist of the San Emigdio Mountains, southern California

Alan D. Chapman, Peter Luffi, and Jason B. Saleeby

Division of Geological and Planetary Sciences, California Institute of Technology, Pasadena, CA

ABSTRACT

Intergranular element transfer-controlled garnet growth is a recently suggested explanation for high-Ca annuli in chemically zoned garnets from a wide range of bulk compositions. However, little is known regarding the source of requisite elemental fluxes responsible for such Ca disequilibrium during garnet growth. The Rand schist of the San Emigdio Mountains permits testing between two potential sources: (1) fluid enhanced disequilibrium breakdown of metastable plagioclase during metamorphism, and (2) hydrous partial melting. X-ray imagery of garnets from the Rand schist shows distinct zonation patterns in major and trace elements that cannot be reproduced by classical closed system modeling. In several grains displaying typical prograde zonation (core-to-rim Mg# increase and sharp Mn decrease) pronounced high-Ca annuli coincide with markedly decreased concentrations of Ti, Y, and Na. These annuli are also distinguished by abundant zircon inclusions absent from other zones. Calculations based on muscovite – biotite – plagioclase – garnet geobarometry and garnet – biotite geothermometry yield two clusters of P-T conditions at 9.5 kbar and 650°C and at 12 kbar and 740°C, indicating local disequilibrium. Thermodynamic equilibrium considerations corroborated by textural features of the samples favor the higher temperature results as peak conditions. Based on combined evidence from X-ray imagery, thermobarometry, petrography, and inclusion distribution in garnets, a model for garnet growth involving a stage of anatexis is preferred. These observations yield important insight into allochemical processes controlling garnet zonation patterns and into the application of detrital zircon thermochronology to the Rand schist.

BACKGROUND: DISEQUILIBRIUM ELEMENT INCORPORATION MODEL

Thermodynamic models of rocks with MORB composition (Konrad-Schmolke et al., 2005) and garnet zonation patterns from micaceous quartzites (Chernoff and Carlson, 1997) show evidence for disequilibrium incorporation of Ca during garnet growth. These studies show that high-Ca annuli in garnets can be produced during sporadic porphyroblast growth in localized chemical inhomogeneities (figure 1). Zoning profiles from garnets found in the Rand schist of the San Emigdio Mountains, southern California, display similar zonation patterns. However, the observed Ca zonation patterns are ubiquitous at the outcrop scale and coincide with pronounced fluctuations in trace element concentrations. Open system processes such as fluid-fluxed partial melting and/or catastrophic breakdown of Ca-bearing phases may account for observed variations in garnet composition.

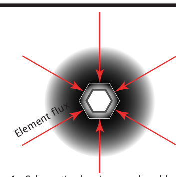

Figure 1. Schematic showing porphyroblast growth within a concentration gradient. Garnet zonation patterns are the result of disequilibrium element flux toward the surface of the porphyroblast. Redrawn after Konrad-Schmolke, 2005

GEOLOGY OF THE SAN EMIGDIO MOUNTAINS

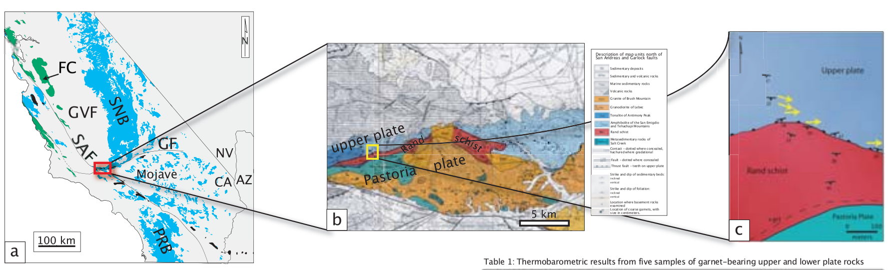

Figure 2. Geologic context of the San Emigdio Mountains. (a) Map of arkosic schist distribution throughout southern California and adjacent areas. Major Late Cretaceous to Early Tertiary schist bodies are colored black. Cretaceous and older batholithic and associated metamorphic rocks are shown in light blue. Rocks of the Franciscan Complex (FC) are colored green. GF=Garlock fault, GVF=Great Valley forearc basin, PRB=Peninsular Ranges batholith, SAF=San Andreas fault, SNB=Sierra Nevada batholith, redrawn after Kidder and Ducea, 2006. (b) Geologic map after Ross, 1989 of the crystalline basement of the San Emigdio Mountains, which are overlain to the north by younger sedimentary and volcanic rocks. (c) Geologic map of a ridge studied in detail. Yellow arrows show the observed shear sense between batholithic rocks which constitute a regional upper plate and the lower plate Rand schist. Garnet abundance and size increases north of the +grt isograd.

Table 1: Thermobarometric results from five samples of garnet-bearing upper and lower plate rocks

Sample	Unit	T (°C)	P (kbar)
04SE1a	upper plate	660 (Holland and Blundy, 1994)	7.1 (Kohn and Spear, 1990)
06SE16a	upper plate	642 (Ganguly et al., 1996)	7.1*
04SE1b	Rand schist	696 (Ganguly et al., 1996)	11.9 (Hoisch, 1991)
06SE9	Rand schist	595 (Ganguly et al., 1996)	9.1 (Hoisch, 1991)
06SE23	Rand schist	737 (Ganguly et al., 1996)	11.4 (Hoisch, 1991)

* Temperature calculated assuming P = 7.1 kbar

GARNET ZONING

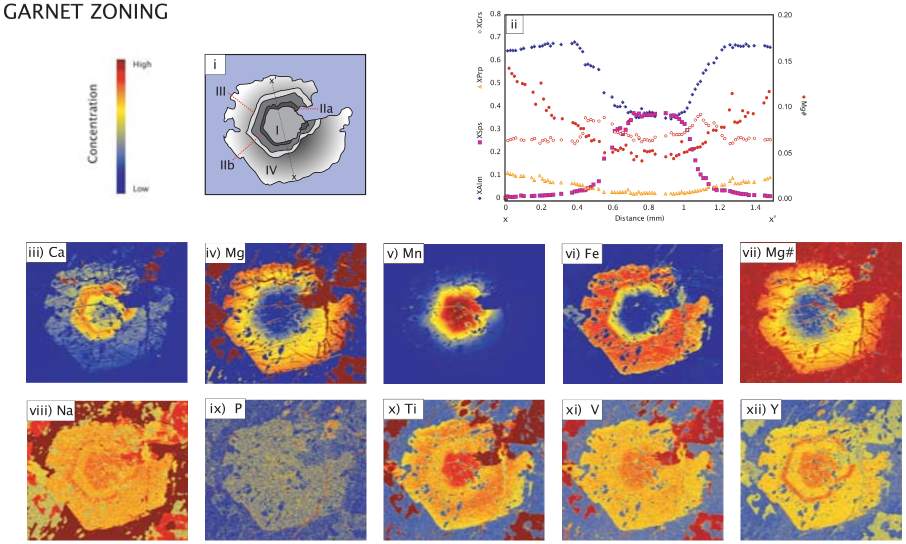

Figure 3. X-ray compositional maps and zoning profiles in garnet from sample 06SE23. Hot colors in X-ray images represent relatively high concentration with red for the highest and blue for the lowest. (i) Schematic diagram showing major garnet zones and the location of the profile in (ii). Zircon inclusions are restricted to zone IIb. (ii) Quantitative zoning profiles of Mg# (Mg/(Fe+Mg)), almandine, spessartine, pyrope, and grossular content along the line drawn in (i). (iii) Ca map: the origin of high-Ca annuli in garnets from the Rand schist of the San Emigdio Mountains is the subject of ongoing research. (iv) Mg map. (v) Mn map: shows typical prograde zonation (core-to-rim decrease in X_{Sps}) without evidence of a Mn "kick-up" (Kohn & Spear, 2000) at rims. (vi) Fe map (vii) Mg# map: note continuously increasing Mg# from core to rim. This suggests continually increasing temperature during garnet growth without evidence for cooling during exhumation. (viii-xii) Trace element maps. In general, measured trace elements show the same, but inverted, zonation pattern as Ca.

CONCLUSIONS

- **Garnet growth history**
  X-ray imagery, thermobarometry, petrography, and zircon inclusion distribution in garnets suggest a model for garnet growth involving a stage of hydrous partial melting.
- **Schist ascent from depth**
  If the Rand schist of the San Emigdio Mountains underwent anatexis, melts may have lubricated the margins of the schist and facilitated its exhumation from depth.

FUTURE WORK

- **Zr-in-rutile thermometry**
  to correctly interpret the thermal evolution of the schist, it is critical to have an independent check on the peak temperatures experienced by the schist (figure 4).
- **Equilibrium thermodynamic modelling**
  of mineral assemblages and compositions using THERIAK-DOMINO.
- **Garnet $\delta^{18}O$ profiles**
  to assess the nature of fluid-rock interaction in the Rand schist of the San Emigdio Mountains.

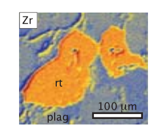

Figure 4. X-ray compositional map of Zr content in rutile from sample 06SE23. Qualitative scale is the same as in figure 3. Temperature has a strong positive correlation with the Zr content in rutile. Note a narrow zone of high Zr near the rim of each rutile grain. This zone may have been the result of a late stage of heating.

Waveform Modeling of the Slab underneath Japan

Min Chen, Jeroen Tromp, Don Helmberger & Hiroo Kanamori
Seismological Laboratory, California Institute of Technology, mchen@gps.caltech.edu

Abstract

We study 3-component seismograms from more than 600 Japan Hi-net stations produced by two earthquakes in the Japan subduction zone, which occurred in the down-going Pacific Plate at depths greater than 400 km. We simulate body-wave propagation in the 3-D P-wave model (Zhao, et al., 1994) using 2-D finite-difference (FDM) and 3-D spectral-element (SEM) methods. As measured by cross-correlation between synthetics and data, Zhao et al.'s P-wave model (1994) typically explains about half of the traveltime anomaly and some of the waveform complexity, but fails to predict the extended SH wavetrain. In this study we take advantage of the densely distributed Hi-net stations and use 2-D FDM modeling to simulate the P-SV and SH waveforms. Our 2-D model suggests a thin, elongated low-velocity layer (LVL) exists atop the slab, extending down to a depth of 300 km with an S-wave velocity reduction of 14% if a thickness of 20 km is assumed. Further 3-D SEM simulations confirm that this model explains a strong secondary arrival which can not easily be imaged with standard tomographic techniques. The low-velocity layer could explain the relatively weak coupling associated with most subduction zones at shallow depths (<50 km), generally involving abundant volcanic activity and silent earthquakes, and it may also help to further our understanding of the water-realted phase transition of ultra-mafic rocks, and the nature of seismicity at intermediate depths (~70 - 300 km).

3-D P-wave models

Figure 1. **Cross-sections** trough the regional and global tomographic P-wave models derived by Zhao et al. (1994) and Zhao (2001). Colors indicate P-wave velocity anomalies relative to 1-D Earth model IASPEI91. (a) The regional model. (b) Comparison between the global and regional P-wave models.

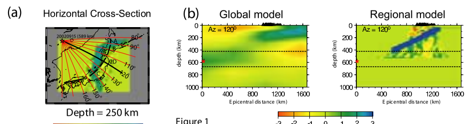

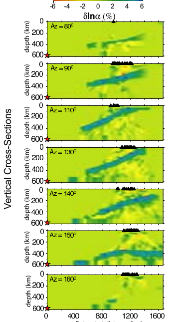

Figure 1

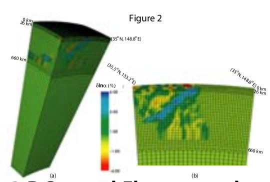

Figure 2

3-D Spectral-Element mesh

Figure 2. P-wave velocity anomalies are superimposed on the mesh. For parallel computing purposes, the one-chunk SEM simulations are subdivided in terms of 25 slices. The center of the chunk is at (38.5° N, 137.5°E), and the lateral dimensions are 30° X 30°. (a) Full view of two neighboring slices. (b) Close-up view of the upper mantle mesh.

Events and Stations

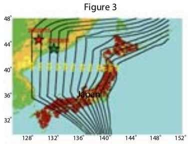

Figure 3

Figure 3. Map view of the study area : Hi-net stations are indicated by red triangles and contours of the upper plate boundary of the Pacific are indicated by black lines. The location of event 20020915 is marked by the red star and event 20030831 is indicated by the green star.

Data selection and model testing

Figure 4. P waveforms. (a) Az = 120° - 130°. (b) Az = 130° - 140°.

Figure 5. P-wave data-synthetics cross-correlation.

Figure 6. S-wave data-synthetics comparison. (a) Radial S waves. (b) Vertical S waves.

f = δln β / δln α . β : S-wave velocity. α : P-wave velocity. Preferred scaling factor : f = 1.5 - 2.0.

Figure 4

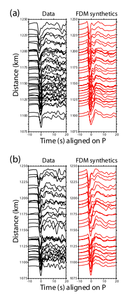

Figure 5

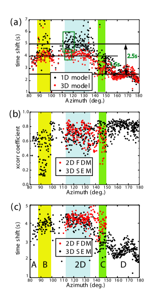

Figure 6

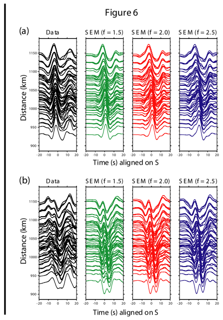

Figure 9. S-wave data-synthetics cross-correlation.

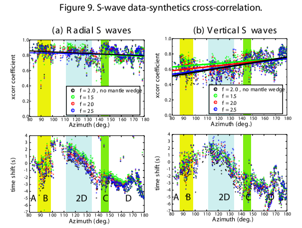

Figure 8. Map of Japan subduction zone area

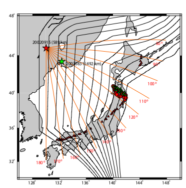

Figure 9. Azimuthal profile

Stations indicated by red triangles in Figure 8

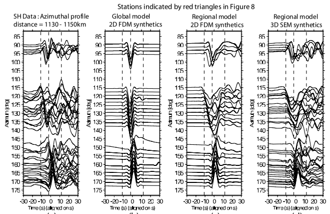

Figure 10. Distance profile

Stations indicated by red circles in Figure 8

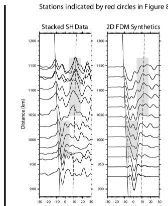

FDM simulations

Figure 11. Base models with a slab inside the transition zone

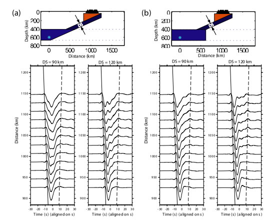

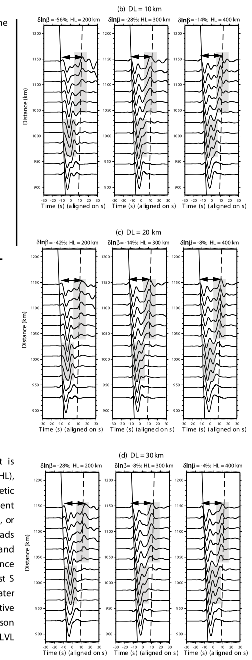

Figure 12. Slab models with a low velocity layer

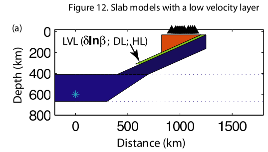

The LVL is indicated by the green polygon in (a). It is characterized by its thickness (DL), its maximum depth (HL), and its relative velocity perturbation (δlnβ). (b, c, d) Synthetic waveforms calculated for nine models with different thickness DL (10, 20, or 30 km), and depths HL (200, 300, or 400 km). The length of the bar with two-way arrow-heads indicates the largest separation between the first arrival and the later arriving up-swing phase, which is 23 s at a distance of 1150 km. The solid lines indicate the approximate first S arrival and the dashed lines align with the peak of the later arriving up-swing phases in the data. The waveforms sensitive to the LVL are highlighted by the gray boxes. The comparison between data and synthetics indicates models with a LVL extending over a depth of 300 km are preferable.

Figure 13. Three models with different types of mantle wedges

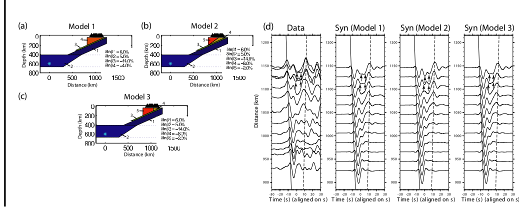

3-D SEM Verification

Figure 14 Three-component S-waveform and vertical P-waveform comparison bewteen data (black lines) and 3-D SEM synthetics (red lines). SEM synthetics are calculated for Model 2 in Figure 13 . Both data and synthetics for S waves are filtered between 6 - 29 s, and for P waves between 3 - 29 s. (a) Event 20020915 (depth 589 km). (b) Event 20030831 (depth 492 km). Model 2 is our preferred model and fits the data for both events on all three components adequately.

Figure 14

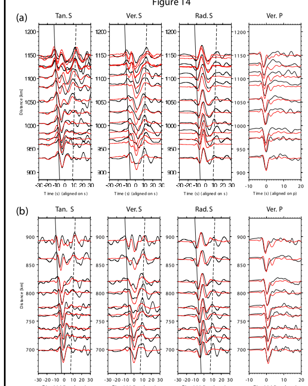

Figure 15

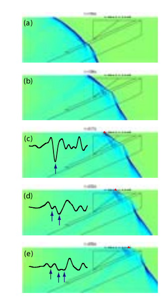

Figure 15. 2-D FD snapshots of SH-wave propagation.

Figure 16

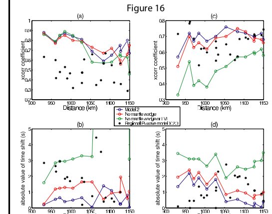

Figure 16. Comparison of cross-correlation coefficients (upper panel) and traveltime anomalies (bottom panel) between data and SEM synthetics for four different models.

Black stars : Regional model.

Blue circles : Model 2.

Red circles : Model 2 without a slow mantle wedge but with a LVL.

Green circles : Model 2 without a slow mantle wedge and a LVL.

Conclusion

The 2-D slab model indicates there is an elongated low velocity layer above the slab extending down to a depth about 300 km, with an S-wave velocity reduction of 14% compared to the normal mantle if the thickness of the LVL is 20 km. However, the thickness of the LVL trades off to some extent with the low S-wave velocity in the LVL. We interpret the LVL beneath NE Japan to be composed of hydrated mafic and/or ultramafic rocks : above a depth of 150 km the LVL could be composed of hydrous mafic crust and serpentinized peridotite above and/or below the descending crust; below a depth of 150 km this hydrous layer is more likely composed of serpentinized peridotite (or at the greatest depth, phase A) above or below the fully eclogitized oceanic crust. Water released from the dehydration reactions in this hydrous zone could cause the abundant arc volcanism, the intermediate intra-slab seismicity (70 - 300 km), and possible silent slip events, which have been observed in other subduction zones.

Body Wave Attenuation Structure in Southern Mexico

Ting Chen[1], Robbert W. Clayton[1]

1. California Institute of Technology, Seismological Laboratory 252-21, Caltech, Pasadena, CA 91125

Abstract

The 2-D model of attenuation structure is determined along a 550 km trench-perpendicular profile in southern Mexico. Velocity spectra from 14 moderate earthquakes recorded by the Meso American Subduction Experiment (MASE) array which consists of 100 broadband sensors from Acapulco to Tampico are used. By assuming a Brune-type source, a path-averaged frequency-independent Q is obtained for each seismogram in the frequency band 0.5 Hz to 7-30 Hz, depending on the signal quality. These measurements are then inverted for spatial variations in Q. The 1-D tomography result shows a pattern of Q qualitatively similar to other subduction zones, with low attenuation crust (Q ~ 1000), and high attenuation in the mantle wedge beneath the Trans-Mexico-Volcanic-Belt (Q < 250). The location of the low-Q region and the variation of the Q value also provides some constraints on the geometry of the subducting slab, or with the structure provided by other methods such as receiver functions, the Q estimates can be used to estimate variations in viscosity.

Method

Spectral Analysis

The Fourier velocity spectral amplitude of a body wave from event j, recorded at station i, can be written as [e.g. Garcia, 2004]

$$A_{ij}(f) = CS_j(f)I_i(f)\exp(-\pi f t_{ij}^*) \quad (1)$$

where S(f) is the source spectra, I(f) is the instrument response, C is the frequency-independent amplitude term associated with geometric spreading, seismic moment, radiation pattern, and other static effects. The exponential term describes the attenuation effect. The term t* can be expressed as t* = t/Q, where t is the travel time, and Q is the quality factor.

Assuming a Brune-type source [Brune, 1970], the source velocity spectrum of event j, can be written as

$$S_j(f) = \frac{f M_{0j}}{1+(f/f_c)^2} \quad (2)$$

where M_{0j} is the signal moment, and fc is the corner frequency.

Since only data in the flat portion of the pass band of the recording system is used in this study, I(f) can be neglected. The corner frequency is estimated based on the result given by Daniel Garcia (2004) for central Mexico, which takes the form of

$$f_c = 1.956\times10^7 M_0^{-0.297} \quad (3)$$

where M_0 is the seismic moment in dyne-centimeters. This result is actually for shear waves, so (3) needs to be modified in this study by taking the P - S wave corner frequency ratio to be 1.5 [Boatwright, 1985], which means the corner frequency for P wave has the form of

$$f_c = 2.934\times10^7 M_0^{-0.297} \quad (4)$$

Now we can rewrite (1) as

$$A_{ij}(f) = \frac{Cf}{1+(f/f_c)^2}\exp(-\pi f\frac{t_{ij}}{Q}) \quad (5)$$

where C is a frequency independent term.

Taking the logarithm of equation (5), we obtain

$$\log A_{ij} = \log C + \log f - \log(1+(f/f_c)^2) - \pi f t_{ij}/Q \quad (6)$$

We then solve this equation by a least-squares method to obtain the average frequency-independent Q for each ray path.

Data and Analysis

We used moderate earthquakes with magnitudes ranging from 4.5 to 5.0. The dataset is shown in Figure 1, and consists of 14 local earthquakes recorded by the instruments of MASE from February 2005 to May 2006.

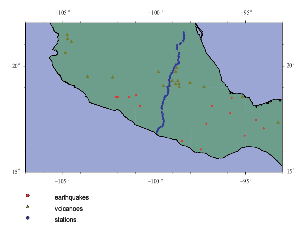

Figure 1

The smoothed spectra of the vertical velocity-component for P wave is calculated from a 3.5 s time window, beginning 0.5 s before the arrival pick, after 5% cosine taper is applied. A smoothed spectra of noise is also calculated from a 3.5 s time window immediately preceding each signal window in the same way. Tests show that changing the window length from 2 - 5 s does not produce significantly different spectra in the frequency band used, so a constant 3.5 s window length was used for all the events. The signal is kept for further analysis if the signal-to-noise ratio is greater than 2, in a frequency band 0.5 to 7-30 Hz.

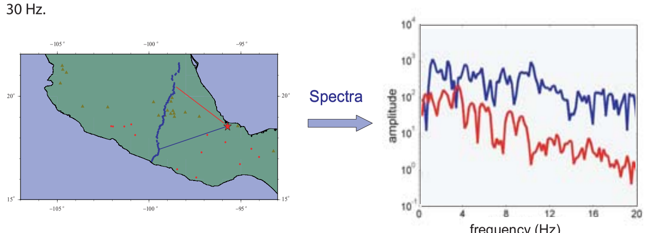

Figure 2

In Figure 2, two velocity spectra are calculated for two paths with the same distance from an event. The blue one is mainly through the crust, and the red one is mainly through the mantle wedge. From figure 2, we can see that the wave passing through the mantle wedge attenuates more than the wave passing through the crust.

A complete set of path-average Q determined for one event is provided in Figure 3 for example.

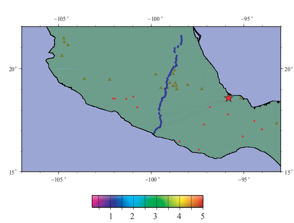

Figure 3

We can see that the average Q for the wave path through the mantle wedge is smaller than that for the path through the crust. This indicates that the mantle wedge is characterized by higher attenuation property than the crust.

Tomographic Inversion

One-dimensional tomographic inversion is used to determine the attenuation structure. Based on the data coverage, the study region is divided into eight blocks parallel to the trench, and each block is assumed to have constant Q. The observed t^* for the ith ray path is

$$t_i^* = \sum_j t_{ij}(Q_j)^{-1} \quad (7)$$

where t is the travel time in block j for the ith ray, and Q is the quality factor of block j. To compute the travel time, we currently assume that the ray path is a straight line connecting the source and station.

The inversion problem can be written in matrix form as

$$[t]_{NM}[Q^{-1}]_M = [t^*]_N \quad (8)$$

where M is the number of blocks and N is the number of data.

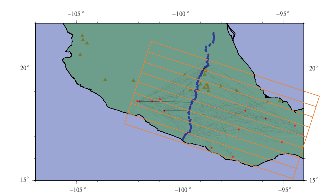

Figure 4

Inversions show high Q in the first four blocks, low Q in the next three blocks, and a slightly higher Q again in the last block (Figure 5). The low Q blocks correspond to the Trans-Mexico-Volcanic-Belt on the map. We interpret the low-Q region as the mantle wedge, as has been shown in attenuation studies of other subduction zones.

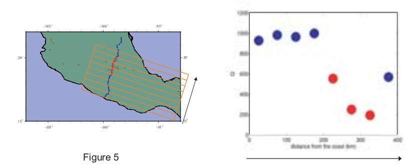

Figure 5

Our results indicate that the mantle wedge begins about 200 km, and ends about 350 km from the coast, and gradually transitions to normal upper mantle beyond that (Figure 6).

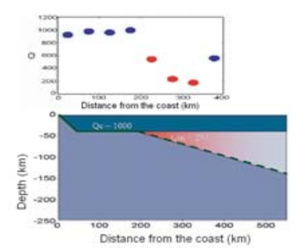

Figure 6

Summary

We have studied the attenuation structure in southern Mexico using the spectral decay method. The results show a low-Q zone beneath the Trans-Mexico-Volcanic-Belt, which we interpret to correspond to the mantle wedge. We suggest that the mantle wedge lies between about 200 km and 350 km from the coast, and has a low Q value less than about 250. The attenuation structure obtained in this study is similar to that of many subduction zones.

Our future work is to obtain a more detailed 3-D tomographic attenuation model, which takes Q variation in depth and varying subducted slab geometry into consideration. This work may involve earthquake relocation and ray tracing. Then, we can convert the attenuation model into viscosity model by using the approximation $\eta'/\eta = (Q/Q_0)^{1/\alpha}$ [Billen and Gurnis, 2001]. The viscosity value obtained will help us to conduct a more realistic geodynamic modeling in southern Mexico.

Coseismic Slip and Afterslip of the Great (Mw9.15) Sumatra-Andaman Earthquake of 2004.

Mohamed Chlieh[1], Jean-Philippe Avouac[1], Vala Hjorleifsdottir[1], Teh-Ru Alex Song[1], Chen Ji[1,2], Kerry Sieh[1], Anthony Sladen[3], Helene Hebert[3], Linette Prawirodirdjo[4], Yehuda Bock[4], and John Galetzka[1]

1.Tectonics Observatory, Division of Geological and Planetary Sciences, California Institute of Technology, Pasadena, CA 91125, USA.
2.Laboratoire de Détection et de Geophysique, CEA, Bruyère-leChatel, France
3.Cecil H. and Ida M. Green Institute of Geophysics and Planetary Physics, Scripps Institution of Oceanography, University of California San Diego, La Jolla, CA 92093, USA.

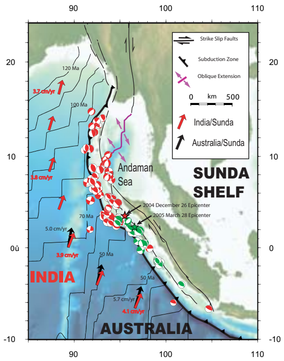

Figure 1: Neotectonic setting of the great Sumatra-Andaman earthquake. Plate velocities of Australia (~5.7cm/yr) and India (~3.8cm/yr) relative to Sunda were computed from the regional kinematic model of Bock et al. [2003] and Socquet et al. [2003]. Age of the sea floor [Cande and Kent 1995; Gradstein et al. 1994] increases northwards from about 50 Ma in the epicentral area to 90Ma near Andaman Islands. The red star indicates the epicenter of the 26 December, 2004 Sumatra-Andaman Mw9.15 earthquake and the green star the epicenter of the 28 March, 2005 Nias Mw8.7 earthquake. CMT associated to the aftershocks of the 2004 Sumatra-Andaman earthquake and in red and to the aftershocks of the 2005 Nias earthquake in green.

We determine coseismic and the first-month postseismic deformation associated with the Sumatra-Andaman earthquake of December 26, 2004 from near-field Global Positioning System (GPS) surveys in northwestern Sumatra and along the Nicobar-Andaman islands, continuous and campaign GPS measurements from Thailand and Malaysia, and in-situ and remotely sensed observations of the vertical motion of coral reefs. The coseismic model shows that the Sunda subduction megathrust ruptured over a distance of about 1500 km and a width of less than 150 km, releasing a total moment of 6.7-7.0 1022 Nm, equivalent to a magnitude Mw~9.15. The latitudinal distribution of released moment in our model has three distinct peaks around 4°N, 7° and 9°N, which compares well to the latitudinal variations seen in the seismic inversion and of the analysis of radiated T-waves. Our coseismic model is also consistent with interpretation of normal modes and with the amplitude of very long period surface waves. The tsunami predicted from this model fits relatively well the altimetric measurements made by the JASON and TOPEX satellites. Neither slow nor delayed slip is needed to explain the normal modes and the tsunami wave. The near-field geodetic data that encompass both coseismic deformation and up to 40 days of postseismic deformation require that slip must have continued on the plate interface after the 500s long seismic rupture. The postseismic geodetic moment of about 2.5 1022 Nm (Mw~8.8) is equal to about 30±5% of the coseismic moment release. Evolution of postseismic deformation is consistent with rate-strengthening frictional afterslip.

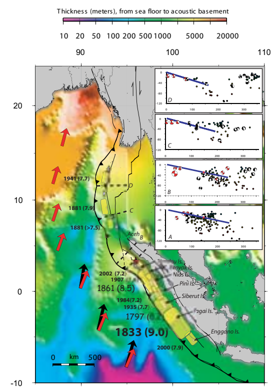

Estimated ruptured area of the major interplate earthquakes along the Sumatra subduction zone between 1833 and 2004 (Newcomb and McCann, 1987; Zachariasen et al, 1999; Natawidjaja et al, 2004). The background shows the sediments thickness from sea floor to accoustic basement. Insets show cross sections with Model's geometries, relocated seismicity and CMT solutions of aftershocks.

Coseismic Slip

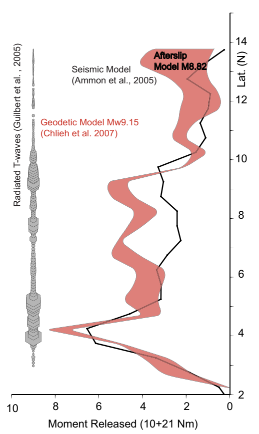

Latitudinal variations of scalar moments as determined from seismic model Ammon-III [Ammon et al. 2005] and from the geodetic coseismic slip model Mw9.15. Both our model and model derived from the latitudinal variation of radiated energy by T-waves [Guilbert et al. 2005] show three distinct regions of energy release. The size of hexagonale symbols corresponds to the relative amplitude released since the earthquake as recorded by hydrophone sensors at Diego Garcia islands.

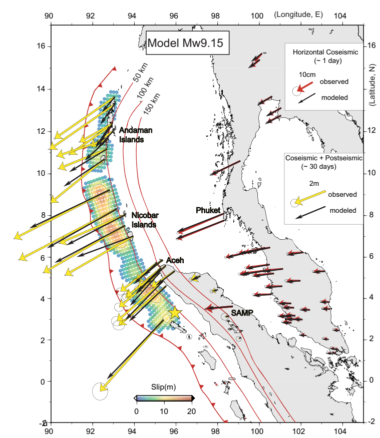

Slip distribution and predicted GPS displacements (black vectors) of the coseismic slip model (Mw9.15). Far-field coseismic displacements are representative to the displacements measured the day after the earthquake [Vigny et al. 2005]. Near-field displacements include coseismic and between 20 to 40 days of post-seismic deformation. Note the change of scale between arrows to the west (Andaman-Nicobar-Aceh) and arrows to the east (Thailand, Malaysia and SAMP).

Afterslip

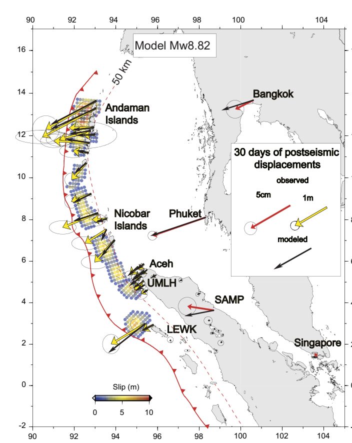

Postseismic slip distribution (slip contours are each 2-m)
Inversion of 1-month cumulative postseismic displacements recorded at permanent GPS stations of SAMP, UMLH, LEWK, Phuket, Bangkok and Singapore and the near-field residuals of the coseismic slip model M9w.15 covering 20 to 40 days of postseismic displacements (Model Mw~8.82).

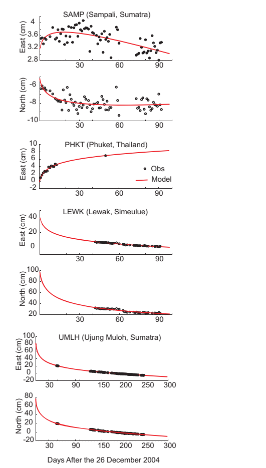

Continuous GPS time series and best-fitting analytical function corresponding to frictional afterslip [Perfettini and Avouac 2004a]. The relaxation time was determined from the best fit to Sampali (SAMP) and Phuket (PHKT) time series and applied to fit the Ujung Muloh (UMLH) and Lewak (LEWK) time series.

Consistencies of the Coseismic Slip model with:

CMT

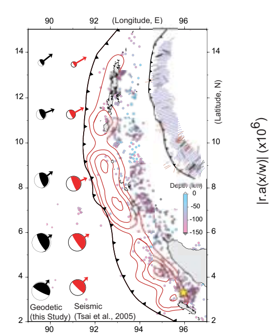

Summary of slip characteristics on the megathrust during the 2004 earthquake for the Coseismic Slip Model M9.15. Slip contours are each 5-m increments. Most of the 2004 coseismic slip occurred trenchward of prior seismicity (circles from [Engdhal et al. 1998]). Black beach balls are best-fitting double-couple mechanism for five regions of the rupture for the model. These are quite similar to the beach balls given by Tsai et al. [2005], based upon centroid-moment-tensor (CMT) analysis of the earthquake. The upper inset show the azimuth of slip on the megathrust (small arrows) which is primarily down dip south of 12N but strike-slip farther north. Bars are the slip vector azimuths of shallow dipping foreshocks and aftershocks from the Harvard CMT catalogue.

Normals Modes

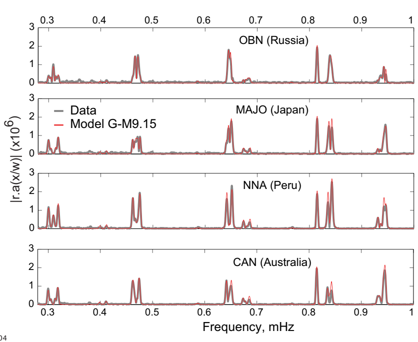

Comparison between normal modes data (thick line) and geodetic model M9.15 synthetics at four stations: OBN (Obninsk, Russia), MAJO (Matsushiro, Japan), NNA (Nana, Peru), CAN (Canberra, Australia).

Very Far-Field

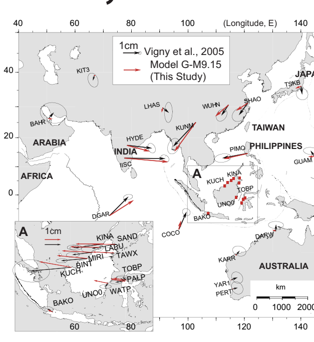

Comparison of the very far-field GPS [Vigny et al. 2005] and predicted displacements of model M9.15 computed by SEM between 2000 and 4000 seconds. This model accounts for 3D structure (model Crust 2.0, [Bassin et al. 2000]), ellipticity, gravity, rotation, topography and ocean load.

Tsunami

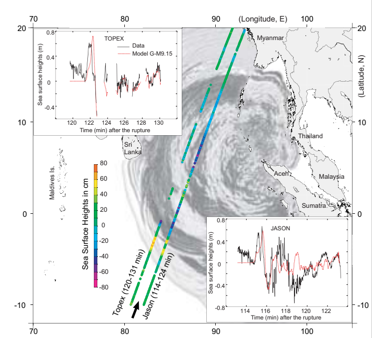

Sea surface heights observed by the JASON and TOPEX-Poseidon satellites compared to numerical simulations of the tsunami based on the coseismic model M9.15 (dotted lines).

The model that fits best the geodetic measurements recorded within the first day of the 2004 earthquake is M9.15 . This model is consistent with seismological, tsunami and T-waves observations. We deduce that the seismic rupture must have propagated as far as 15ºN. The latitudinal distribution of moment in the model has three distinct peaks. This pattern is consistent with latitudinal variations in energy released by T-waves and high-frequency diffracted seismic waves . The general pattern in the model is a gradual northward decrease in slip. The fact that this mimics the northward decrease of the convergence rate across the plate boundary suggests that this pattern might be a characteristic feature of the large ruptures along this stretch of the megathrust.

Although our data place only low constraints on slip near the trench it seems that the coseismic rupture didn't reach to the trench everywhere. This inference is based on the slip distribution obtained from the inversion of the geodetic data and the consistency of that model with the amplitude of the deep-sea tsunami wave. Possibly that would reflect the effect of the poorly lithified sediments at the toe of the accretionary prism on the rheology of the plate interface, which would have inhibited the propagation of the seismic rupture due to a rate-strengthening friction mechanism [Byrne et al. 1988; Scholz 1998]. If this is so, one would expect afterslip on the megathrust proximal to the trench in response to stresses induced by the coseismic rupture [Marone et al. 1991].A model of frictional afterslip explains to first order the evolution of postseismic deformation. Within 60 days of the earthquake, post-seismic moment release equaled about 35% of the coseismic moment, the equivalent of an Mw 8.82 earthquake. The ratio of coseismic to postseismic slip is higher than this average north of 11ºN. In fact, afterslip in this portion of the megathrust in the month following the earthquake was larger than the coseismic slip . Perhaps this is evidence that the rheology of the megathrust there is strongly influenced by subduction of the exceptionally thick sedimentary sequence of the Bengal fan. Although its spatial distribution is poorly resolved, afterslip seems to have occurred over about the same width of the megathrust as coseismic slip.

Geodetic and paleogeodetic resolution of locked patches on the Sunda megathrust, offshore Sumatra

Mohamed Chlieh, Jean-Philippe Avouac, Kerry Sieh, Danny H. Natawidjaja, John Galetzka,
Tectonic Observatory, Caltech, Pasadena, CA
Research Center for Geotechnology, Bandung, Indonesia

Geodetic and paleogeodetic measurements of strain above the Sumatran portion of the Sunda subduction zone reveal a heterogeneous pattern of coupling along the subduction megathrust. Annual banding in coral heads provides vertical rates of deformation spanning the last half of the 20th century and repeated GPS surveys between 1991 and 2004 and continuous measurements at GPS stations operated since 2002 provide horizontal velocities. The area of the plate interface within which the coupling is high is only ~75 km wide near the Equator but increases to ~175 km farther south. Major sections of this Locked Fault Zone (LFZ) coincide with the rupture areas of major Mw>8.5 interplate earthquakes. The section that ruptured during the Mw 8.7 Nias earthquake of 2005 released about 2/3 of the slip deficit that had accumulated since its previous rupture in 1861. Farther south, beneath the Mentawai islands, overlapping ruptures of the LFZ produced giant earthquakes in 1797 and 1833. The accumulated slip deficit since these events is slowly reaching the amount of slip that occurred during the 1833 earthquake but already exceeds the slip that occurred during the 1797 earthquake. Thus, re-rupture of the Mentawai patch in the near future seems quite likely. In contrast, coupling is low in the Batu islands near the Equator and around Enganno island at about 5S, where only moderate earthquakes have occurred in the past two centuries. Temperature might influence the mode of slip along the plate interface, through its effect on the rheology of sediments at the plate interface. Other influences, such as structures on the subducting plate, could also play a role. In particular, subduction of the Investigator Fracture Zone near the Equator coincides with the relatively low coupling there.

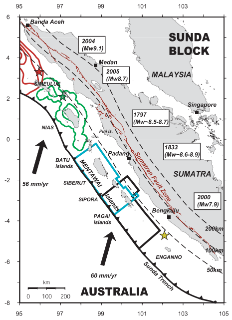

Seismo-tectonic setting of the Mentawai segment along Sumatra subduction zone with location of rupture area of M>8 earthquakes since 1700. The Mw8.7 1861 Nias earthquake that has broke a similar segment than the Nias 2005 earthquake is not reported [Briggs et al. 2006; Newcomb and McCann 1987]. Rupture area of the 2004 Sumatra-Andaman (red) and 2005 Nias earthquake (green) are represented by their 5m coseismic slip contours [Chlieh et al. 2006; Hsu et al. 2006]. Ruptures of the 1797 (blue) and 1833 (black) earthquakes show the elastic dislocation models of coral records of co-seismic uplift [Natawidjaja et al. 2006a]. It is not clear whether the 1833 rupture ends north, or extends south of Enganno island. Iso-depth contours 50km, 100km and 200km (dashed lines) of the megathrust interface are from [Gudmundsson and Sambridge 1998].

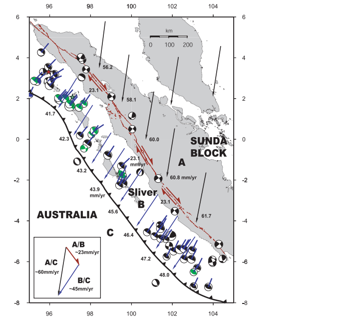

Secular motion of the Sumatra forearc Sliver (B) relative to Australia (C). Plate motion of Sunda, A (black arrows) relative to Australia determined from [Bock et al. 2003] (see parameters in Table 1) and from the Sumatra forearc sliver, B (blue arrows), relative Australia, C. Focal mechanisms of Mw>6 earthquakes between 1976 and June 2005, are from the Harvard centroid moment tensor (CMT) catalogue. CMT after the March 2005 Nias earthquake are in green. Assuming that the Sumatran Fault Zone is purely strike-slip and that the slip vectors of interplate earthquakes is parallel to the long term slip along the plate interface, the Sunda/Australia oblique convergence (black arrow in inset) is partitioned into ~23mm/yr strike-slip motion along the Sumatran Fault Zone (red arrows in inset) and about 42-

FORWARD MODELS AND INVERSION

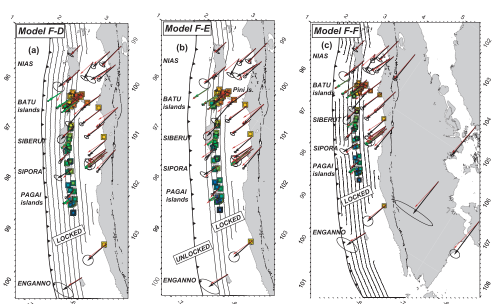

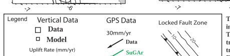

Three-dimensional back-slip model with variable widths of locked fault zone. The interseismic LFZ of the megathrust interface is represented each 5km-depth contour lines. Three tests are done with different hypothesis on the distance of the LFZ updip limit to the trench, (a) the LFZ reaches the trench everywhere (Model F-D), (b) it is at 50km from the trench everywhere (Model F-E) and (c) it is at variable distance from the trench (Model F-F). The predicted GPS velocities are in red and the observed in black (Bock et al. 2003) and green (SuGAr data). The predicted vertical rates are represented by small squares inside the observed vertical rates (big squar), all scaled using the same color bar.

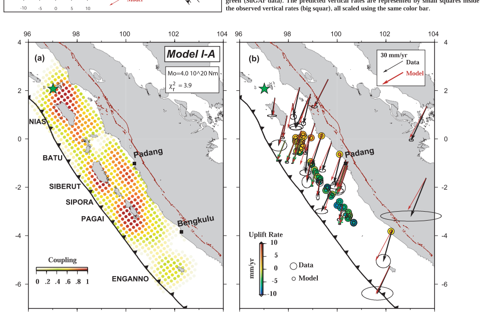

Inversion of the coral and GPS data weighted by their 1-sigma uncertainties. (a) Coupling distribution on the megathrust interface of model I-A (Table 7). Fully coupled areas are in red color and fully creeping area are in white. The gradual decoupling is shown by the color bar. The accumulated moment deficit rate of that inversion is 4.0 x 1020 Nm/yr. (b) Predicted displacements are represented by red vectors for the GPS and by small circles for the data. The reduced Ki^2 of this model is 3.9.

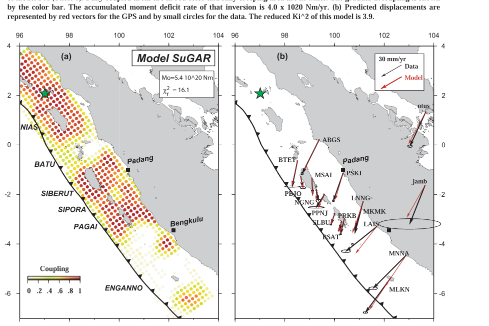

Inversion of the SuGAR Continuous GPS data weighted by their 1-sigma uncertainties. The velocities of all CGPS stations were determined from the time series processed by SOPAC. To reduce deformation related to the postseismic relaxation of the March 2005 Nias earthquake, the velocities were determined for the time-window June 2005 (3 month after the Nias earthquake) to September 2006. (a) Coupling distribution on the megathrust interface. That model suggests that the megathrust portion south of the Pagai islands is creeping at the plate velocity. It confirms also that the 400 km long Siberut-Pagai segment right off-shore Padang city shows a very wide and high coupling. (b) Observed and modelled GPS velocities.

THERMAL MODELS

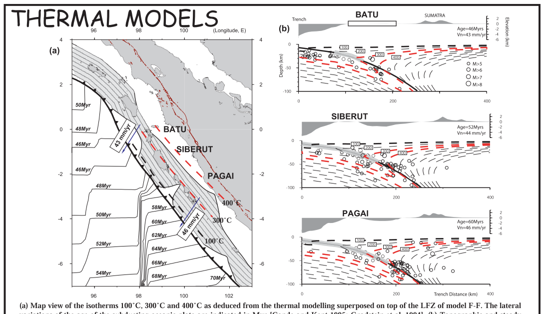

(a) Map view of the isotherms 100˚C, 300˚C and 400˚C as deduced from the thermal modelling superposed on top of the LFZ of model F-F. The lateral variations of the age of the subducting oceanic plate are indicated in Myr [Cande and Kent 1995; Gradstein et al. 1994]. (b) Topographic and steady state thermal structure of the meagthrust interface for three trench-normal sections across the Batu, Siberut and Pagai islands. The slab interface is drawn using the background relocated seismicity catalogue of [Engdhal et al. 1998]. The LFZ of the meagthrust interface deduced from Model F-F are reported in grey. Isotherms are computed from analytical expression of the steady state thermal structure model proposed by {Royden, 1993 #362}. The model accounts for conduction, advection, a shear heating of 40 mW/m2 and upper plate radiogenic heat production of 0.4 mW/m3. The two parameters varying between profiles are the age and the normal convergence velocity of the subducting plate . On each profile, the downdip end of the

PALEOGEODETIC AND GEODETIC DATA

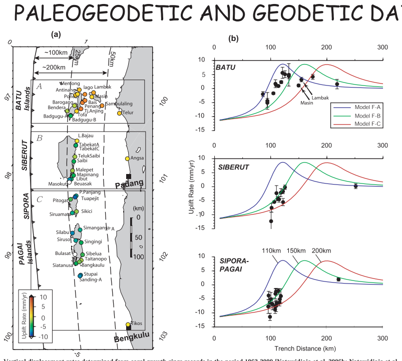

Vertical displacement rates determined from coral growth rings records in the period 1962-2000 [Natawidjaja et al. 2006b; Natawidjaja et al. 2004] in map view and along sections normal to the trench. Boxes indicate the swath corresponding to each section. The origin of horizontal axis on each section is at the trench. The forearc islands are dominantly subsiding as expected if this pattern is consistent with the shallow portion of the plate interface being locked to some degree during this interseismic period. For reference, the continuous lines in the sections show the predicted uplift rates computed assuming that the plate interface is fully locked from the trench to a depth of 30, 40, or 50km, corresponding to a increasing width of the LFZ of ~110km (blue), 150km (green) and 200km (red). Subsidence rates generally increase southward along strike suggesting the LFZ is narrower in the Batu islands area near the Equator.

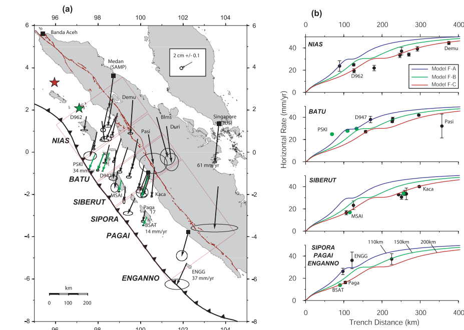

Horizontal velocities relative to Australia, as defined by the plate motion of Australia relative to ITRF200 of Bock et al. (2003), at campaign sites (black arrows) and at the Continuous GPS station of the Sumatra Geodetic Array, SuGAr, (green arrows). Ellipses show uncertainties at the 1-? confidence level (Tables 3 and 4). Plots on the sides show the trench normal horizontal velocities along various sections. The boxes on the map view indicate the swaths corresponding to each section. The origin of horizontal axis on each section is at the trench. Velocities decrease from the Sunda Shelf toward the trench from 60mm/yr to 14mm/yr. Predictions from model F-A, F-B, and F-C corresponding to a Locked fault Zone width of respectively 110, 150 and 200km are shown for comparison (Table 5).

Locked Fault Zone Vs 1797, 1833, 2005 Giant earthquakes

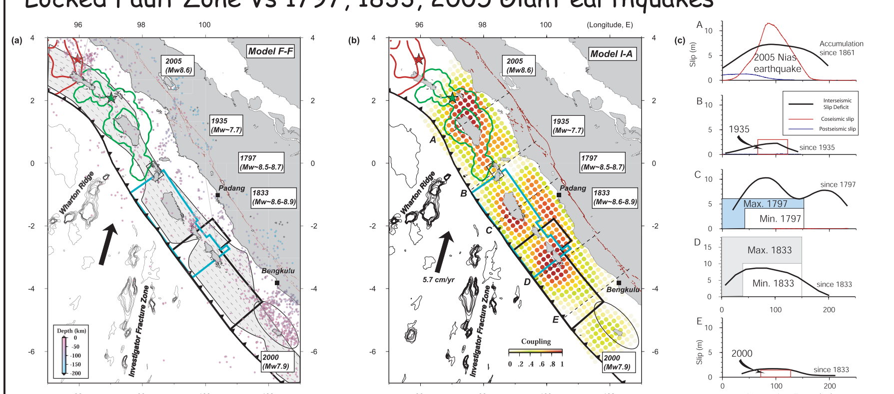

(a) LFZ of model F-F. Below the Batu Islands where the LFZ is narrow, only large earthquake (Mw>7-7.5) happened since below the Siberut and Pagai Islands where the LFZ is wide, giant earthquakes (Mw>8-9) occurred. Background seismicity from [Engdhal et al. 1998] traces relatively well the downdip end of the Locked Fault Zone. The embayment of the LFZ in the Batu could be related to the subducting fossil Investigator Fracture Zone. (b) LFZ of model A-I is shown. Note the remarkable coincidence of the high coupling area (orange-red dots) with the 5m coseismic slip contours of the 2005 Nias earthquake. The 1797 and 1833 ruptures from Natawidjaja et al. 2006 are also well centred on highly coupled asperities. The southernmost rupture

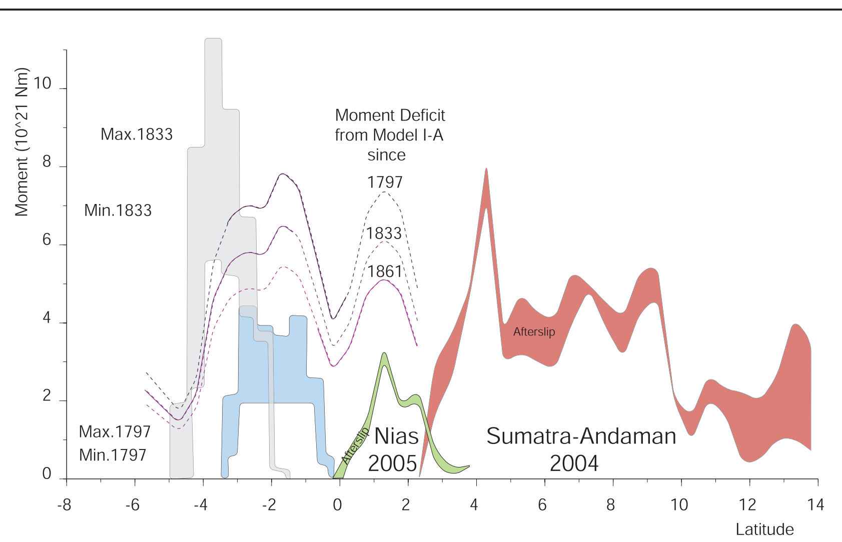

Latitudinal variations of scalar moments as function of latitude for the 2004 Sumatra-Andaman earthquake [Chlieh et al. 2006], the 2005 Nias earthquake [Konca et al. 2006], and 1797 and 1833 Mentawai earthquakes [Natawidjaja et al. 2006a]. For comparison, the cumulated interseismic deduced since 1797, 1833 and 1861 are shown from the prediction of model I-A

Thermomechanics of mid-ocean ridge segmentation

Eun-seo Choi[1], Luc Lavier[2], Michael Gurnis[1]

[1]Seismological Laboratory, California Institute of Technology, Pasadena, CA 91125, U.S.A.

[2]Institute of Geophysics, University of Texas, Austin

ces74@gps.caltech.edu

Abstract

The mechanics responsible for the initiation of the orthogonal pattern characterizing mid-ocean ridges and transform faults are studied using numerical models. The driving forces are thermal stresses arising from the cooling of young oceanic crust and extensional kinematic boundary conditions. Thermal stress can exert ridge-parallel tension comparable to spreading-induced stress when selectively released by ridges and ridge-parallel structure. Two modes of ridge segment growth have been identified in plan view: An overlapping mode where ridge segments overlap and bend toward each other and a connecting mode where two ridge segments are connected by a transform-like fault. As the ratio of thermal stress to spreading-induced stress (γ) increases, the patterns of localized plastic strain on the top surface change from the overlapping to connecting mode. The orthogonal pattern marks the transition from one mode to the other. Besides the amount of stress from each driving force, the rate of stress accumulation is crucial in determining the emergent pattern. This rate-dependence is characterized by the spreading rate normalized by a reference-cooling rate (Pe'). When Pe' is paired with the ratio of thermal stress to spreading-induced stresses (γ'), they define stability fields of the two modes. The obliquely connecting, the orthogonally connecting, and the overlapping mode are similar to the ridge-transform fault intersection observed in ultraslow, slow to intermediate, and fast spreading centers, respectively. The patterns are also sensitive to the strain weakening rate. Fracture zones were created in part as a response to thermal stress.

Introduction

A plausible source for ridge-parallel tension is the cooling of oceanic lithosphere. Thermal cooling stresses make a significant contribution to the stress state of oceanic plates. Thermal stresses are isotropic, but mid-ocean ridges themselves and numerous ridge parallel faults can release thermal stresses in a selective (i.e., ridge-perpendicular) direction when these structures form (Fig. 1). Therefore, the resultant unreleased stress due to cooling would be dominated by the ridge-parallel component.

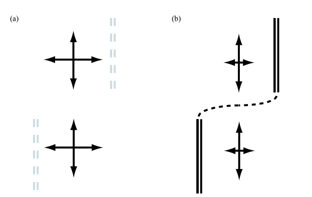

Figure 1: Arrows represent the direction and magnitude of principal components of thermal stresses along ridge-perpendicular and ridge-parallel directions. (a) Before ridge segments are created, thermal stress is isotropic and its horizontal components are equal in magnitude. The future location of ridge segments are marked by the pairs of gray dashed lines. (b) The ridge-parallel component becomes dominant when the ridge-normal principal stress is released by the formation of ridge segments (pairs of solid lines). A possible trace of a structure connecting the ridge segments is denoted by a dased curve.

The role of thermal stress was important in analog experiments. Oldenburg and Brune [JGR, 1972] designed an experiment in which the surface of molten wax was chilled by a fan. They observed the spontaneous growth of an orthogonal system of ridge, transform faults, and fracture zones with characteristics similar to natural systems.

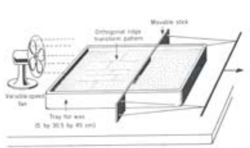

Figure 2: Apparatus setup for the wax experiment by Oldenburg and Brune [1972].

Figure 3: Patterns formed on the frozen surface of wax [Oldenburg and Brune, 1972].

Numerical Method

We turn to a numerical approach although wax models' success in creating the patterns appears to imply that the patterns are made by the very mechanism acting along mid-ocean ridge. Using numerical simulations, known representative values for the Earth's material can be directly used in models. In addition, numerical experiments allow for a better control on testable mechanisms and a wide range of parameter values. Numerical models can also be used to make explicit predictions of geophysical observations such as bathymetry and gravity.

We use SNAC (**S**tGermai**N** **A**nalysis of **C**ontinua), which is an energy-based finite difference code solving equations of momentum balance and heat energy conservation. SNAC can descritize a fully 3-D model domain into a structured tetrahedral mesh. Lagrangian description of motion is adopted. The following features of SNAC are noteworthy:

Mixed Discretization: To deal with incompressibility, volumetric strain in individual tetrahedron is replaced with an average over two overlays (see Fig. 4).

Remeshing: Lagrangian meshes are remeshed to relieve extreme mesh distortion. Nodal values are interpolated from the old mesh to the new one; element values are transferred between the nearest neighbors (Fig. 5).

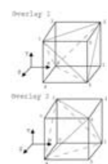

Figure 4: Two different discretizations of a cube with tetrahedra are used for computing average volumetric strain and for symmetric response.

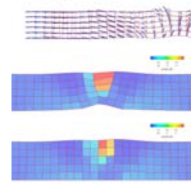

Figure 5: **Top**: Velocity, a node-associated field, is interpolated from the old (blue) to the new (red) mesh. **Middle**: The distribution of plastic strain, an element-associated field, is shown with a deformed mesh. **Bottom**: The plastic strain field has been transferred between the nearest neighbor tetrahedra during remeshing.

Constitutive Model: Total strain is assumed to be the sum of ealstic, viscous, and plastic strain. This consititutive model assumes Maxwell viscoelasticity as a base rheology. When stress increases faster than the relaxation rate, material can yield according to a given criterion: *e.g.*, the Mohr-Coulomb model. Viscosity can be Newtonian or a power-law type.

Model Setup

A hot block of oceanic crust cools while it is stretched at a given spreading rate. Spreading initiates ridge segments, which in turn releases accumulating thermal stress only in the ridge-normal direction. Initial temperature is uniformly 1300 °C except along the top surface, where temperature is 0 °C. The top surface remains isothermal at 0 °C, while the bottom surface has a zero heat flux. These thermal initial and boundary conditions are intended to be those of hypothetically pristine oceanic crust that is about to cool and extend.

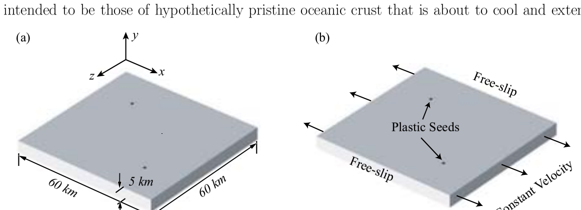

Figure 6: Geometry of the model domain. (a) 60 km × 5 km × 60 km domain with equal 1 km grid spacing in each direction. (b) Two side surfaces normal to the x axis are pulled at a constant velocity. The other two sides, normal to z axis, have free-slip boundary conditions. The bottom is supported by a Winkler foundation. Two plastic seeds, controlling initial localization, are embedded with 30 km separation in the x and z directions.

Results

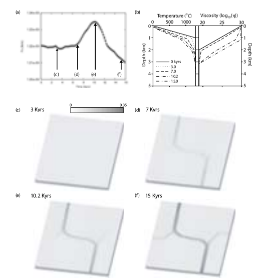

Figure 7: (a) Fx, force required to extend the domain at the applied velocity in the x-direction as a function of time. (b) Depth profiles of temperature and viscosity are compared at different time steps (0, 3, 7, 10.2, and 15 Kyrs). The rise in Fx at approx. 7 Kyrs coincides with the cooling and significant increase in viscosity of the subsurface (1-2 km deep) layer. 3-D rendering of the second invariant of plastic strain at the same set of time steps: (c) 3 Kyrs, (d) 7 Kyrs, (e) 10.2 Kyrs, and (f) 15 Kyrs.

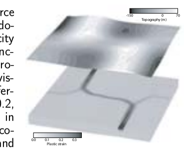

Figure 8: A 3-D representation of the surface topography from the base model at 15 Kyrs on top of the model domain. Plastic strain on the surface of the model domain indicated through grey scale shading.

To assess quantitatively the relative influence of thermal stress to spreading-induced stress on the appearance of localization patterns, we introduce a dimensionless number γ. γ is defined as the ratio of the first invariant of thermal stress to the first invariant of spreading-induced stress. Since the domain geometry (D and L) and the temperature initial condition (ΔT) are common to all the models, we vary the remaining three parameters, v, α_v, and κ to determine their influence on the pattern of localization.

Definitions

$$\gamma = |I_\sigma^{therm}|/|I_\sigma^{spr}|$$
$$I_\sigma^{therm} = -(3\lambda + 2\mu)\alpha_V(T - T_0)$$
$$I_\sigma^{spr} = (3\lambda + 2\mu)\varepsilon_{11}^{spr}$$
$$\therefore \gamma = \frac{(3\lambda + 2\mu)\alpha_V(T - T_0)}{(3\lambda + 2\mu)\varepsilon_{11}^{spr}} = \frac{\alpha_V(\kappa\nabla^2 T)\Delta t}{\dot{\varepsilon}_\sigma^{spr}\Delta t} = \frac{\alpha_V(\kappa\Delta T/D^2)}{v/L} = \frac{\alpha_V(\kappa\Delta T)L}{vD^2}$$
$$\gamma' = \frac{\alpha_V(\kappa\Delta T)L}{v_{ref}D^2}, \text{ and } Pe' = \frac{vD}{\kappa_{ref}}$$

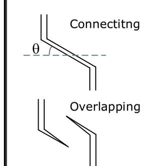

Figure 9: Modes of interaction between two mutually approaching ridge segments. The orthogonal ridge transform fault geometry is a special case of the "connecting mode". The angle, θ, is used as a measure of a connecting pattern's orthogonality spanning the range 0° to 45°.

Those models with the same γ but different parameters can produce considerably different patterns because the growth rates of stresses from cooling and spreading are different even for the proportionally varied parameters. So, we use the Peclet number as another measure of the system which we physically interprete here as the ratio of forced spreading rate (v) to cooling rate (κ/D). To ensure that separate measures of each process are not inherently correlated by sharing common parameters, we compute them with respect to reference values of v and κ/D.

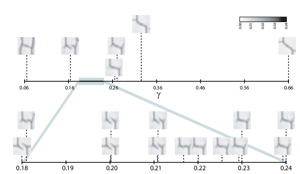

Figure 10: Patterns of localized plastic strain, made on the top surface of models, are arranged in order of increasing γ. The patterns were captured after 10.6 kyrs. As γ increases, the mode of interaction between two mutually-approaching ridge segments changes from overlapping through orthogonal rifting to oblique rifting.

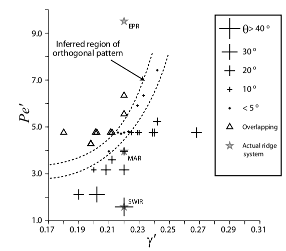

Figure 11: Plot of Pe' versus γ'. The domain of connecting and overlapping mode is well defined and the boundary between them defines the stability field of the orthogonal pattern. Within the connecting-mode domain, the variation in θ is systematic: θ becomes smaller as the values of Pe'-γ' pair gets closer to the inferred region of orthogonal pattern.

MASE: Shallow Subduction in Central Mexico

Robert W. Clayton, Xyoli Pérez-Campos, Paul Davis, Arturo Iglesias, YoungHee Kim, Ting Chen, Alan Husker, Fernando Greene, Lizbeth Espejo, Luca Ferrari, Dante Moran, John Eiler, Mike Gurnis, Vlad Manea, Carlos Valdez, Joann Stock, Vladimir Kostroglodov

ABSTRACT

The objective of the MASE (Middle America Subduction Experiment) is to construct a geodynamical model of the subduction process. The Middle America Trench was chosen as the first example because of the relatively simple plate geometry (a linear margin with near normal subduction) and a significant along-strike slab-dip variation. The initial deployment along the Acapulco to Tampico transect in central Mexico is designed to investigate the case of shallow subduction.

The main results to date are:

- The discovery that the slab underplates the continental crust to a distance of 200 km from the trench. This result is interesting because there is no geologic or geodetic indication of coupling in this zone – the coupling that is measured geodetically is confined to the initial 75 km near the coast where the slab is dipping down. There is also no fluid signature in the magnetotelluric (MT) data of the flat-slab portion of the line.
- The relative attenuation in the mantle under the Mexican Volcanic Belt (presumed location of the mantle wedge) is a factor of 2 higher than the surrounding mantle.
- Modeling studies indicates that a shrinking low-viscosity mantle wedge can lead to flat-slab subduction as observed.
- A slow earthquake appears to be in progress on the southern 200 km of the MASE line. The last slow event occurred in 2002. This one started in March, 2006.

El objetivo del proyecto MASE (*Middle America Subduction Experiment*) es construir un modelo geodinámico que represente un proceso de subducción. Se ha escogido como primer ejemplo la Trinchera de América Central debido a que presenta una geometría relativamente simple (un margen con geometría lineal y con una dirección de convergencia cercana a la normal) y una variación significante del manteo de la placa a lo largo del rumbo. La fase inicial de este proyecto, que consiste en un experimento a lo largo de un transecto localizado en la región central de México entre Acapulco y Tampico, se ha diseñado para investigar este tipo de subducción sub-horizontal. Los principales resultados obtenidos hasta el momento son:

- El descubrimiento de que la placa se encuentra en contacto con la corteza continental hasta una distancia de 200 km de la trinchera. Este resultado es interesante dado que no se ha encontrado indicación geológica o geodésica de que exista acoplamiento en esta zona – el acoplamiento medido en forma geodésica esta confinado a los primeros 75 km cercanos a la costa, donde la placa se encuentra buzando. En la porción del transecto que pasa por la zona de subducción sub-horizontal, los datos magnetotelúricos (MT) no indican la presencia de fluidos.
- Bajo el cinturón volcánico Mexicano (donde se piensa que esta ubicada la cuña del manto) el manto tiene una atenuación relativa con el doble del valor de la del manto circundante.
- Estudios a través de modelos numéricos, indican que la existencia de una cuña de baja viscosidad en el manto puede ser la causa de la presencia de zonas de subducción sub-horizontal como la que se observa en este experimento.
- A partir de Marzo de 2006, se observa que un terremoto lento se esta desarrollando en los 200 km ubicados en la zona sur del transecto de MASE. El último evento de este tipo ocurrió el año 2002.

CURRENT MASE SEISMIC ARRAY

▲ Current Acapulco – Tampico Line

MAGNETOTELLURICS STUDY

Electrical Resistance

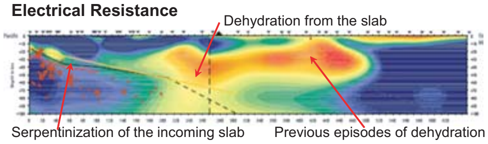

[Jodicke H., Jording A., Ferrari L., Arzate J., Mezger K., Rupke L., 2006. Fluids release from the subducted Cocos plate and partial melting of the crust deduced fro magnetotelluric studies in Soutern Mexico: Implications for the generation of volcanism and subduction dynamics. Journal of Geophysical Research, v. 111, B08102, doi:10.1029/2005JB003739.]

RECEIVER FUNCTION STUDY

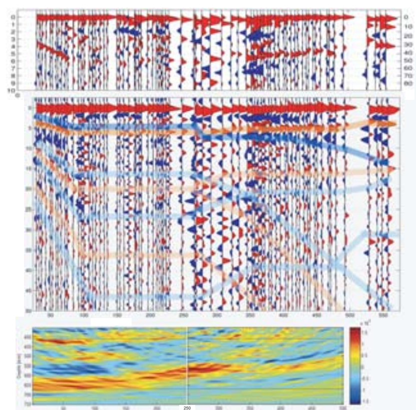

1st panel: Stacked receiver function from 0 to 90 km including Moho and slab
2nd panel: Depth-expanded view with predicted multiples superimposed
3rd panel: Migrated section from 350 to 750 depth including 410, 520, and 660 km discontinuities

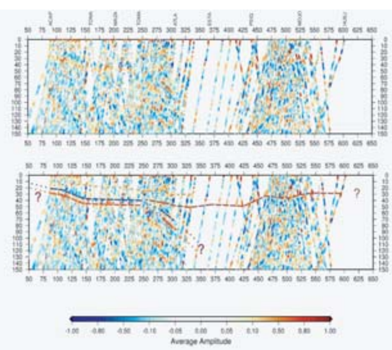

Image by back-projection and migration of receiver function. Top panel is the image and the bottom panel is current interpretation.

ATTENUATION STUDY

Attenuation Model

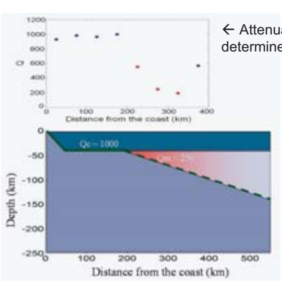

← Attenuation measurements determined from local earthquakes

←Inferred model with a low-Q wedge

SURFACE WAVE STUDY

Velocity Model from Surface Waves

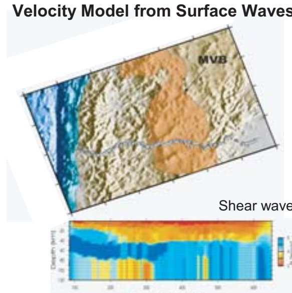

Shear wave velocity model derived ←from Rayleigh waves

GPS STUDY

GPS Transient [From Kostroglodov's group]

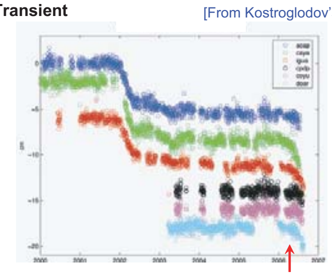

Apparent slow earthquake starting in March of 2006

GEODYNAMICAL MODELING

Simulation of Flat Slab Subduction

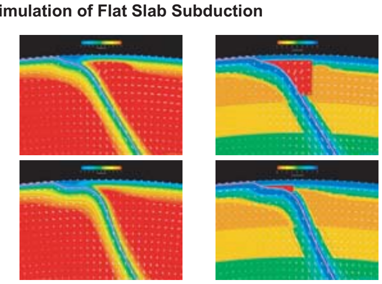

Temperature Viscosity

FUTURE MASE SEISMIC ARRAY

Proposed Oaxaca Line

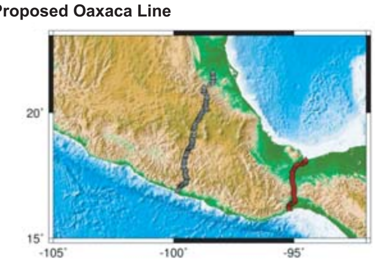

▲ Current Acapulco – Tampico Line
▲ Next Oaxaca – Veracruz Line

OUTREACH

The pictures show engineering students from UNAM making presentations on earth science and earthquake hazard at a school that is hosting a MASE student

Modeling the shortening history of a fault-tip fold using structural and geomorphic records of deformation

M. Daëron*, J.-P. Avouac*, J. Charreau**

(* California Institute of Technology ; ** Institut des Sciences de la Terre d'Orléans)

[Daëron et al., 2006, JGR, in press: http://www.whooshingsounds.net/tecto/public/daeron-jgr-2006.pdf]

Presentation

It is rarely straightforward to interpret uplift rates recorded by geomorphic and structural markers in terms of horizontal shortening, e.g. in the context of piedmont folds, where thrust faults are often blind. Usually, this requires a spatially continuous record of the uplift, such as well-preserved alluvial or fluvial surfaces, as well as assumptions on the underlying pattern of deformation.

Here, using a simple formulation of the displacement field derived from sandbox experiments (Bernard et al., submitted), we parameterize the spatial deformation pattern above the basal detachment of a fault-tip fold. Assuming a stationary spatial pattern of deformation, we simulate the gradual warping and uplift of stratigraphic and geomorphic markers, which provides an estimate of the cumulative amounts of shortening they have recorded. This approach allows modeling of isolated terraces or growth strata.

We apply this method to the study of two fault-tip folds in the Tien Shan, the Yakeng and Anjihai anticlines, documenting their deformation history over the past 6-7Myr. We show that the modern shortening rates can be estimated from the width of the fold topography provided that the sedimentation rate is known, yielding respective rates of 2.15mm/yr and 1.12mm/yr across Yakeng and Anjihai, consistent with the deformation recorded by fluvial and alluvial terraces. This study demonstrates that the shortening rates across both folds accelerated significantly since the onset of folding. It also illustrates the usefulness of a simple geometric folding model, and highlights the importance of considering local interactions between tectonic deformation, sedimentation and erosion.

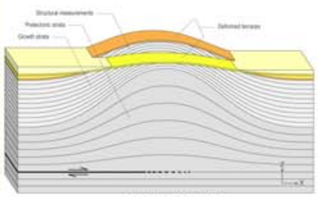

FAULT-TIP FOLD

Fold geometry:
- Seismic data
- Geomorphic surveys

Time constraints:
- Magnetostratigraphy
- OSL dating
- Cosmogenic dating
- Radiocarbon dating

Analyical formulation of fault-tip folding

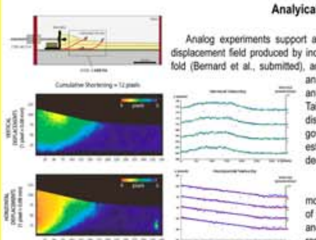

Analog experiments support a simple analytical formulation of the displacement field produced by incremental shortening across a fault-tip fold (Bernard et al., submitted), and this formulation has been used to analyze the growth of Pakuashan anticline along the western foothills of Taiwan (Simoes et al., submitted). The displacement model's parameters, which govern the finite shape of the fold, can be estimated based on seismic imaging of deep pre-growth strata.

We use the same formulation to model the growth of two case examples of young fault-tip folds located in the fold-and-thrust belts that bound the Tien Shan range, in Central Asia.

Regional setting

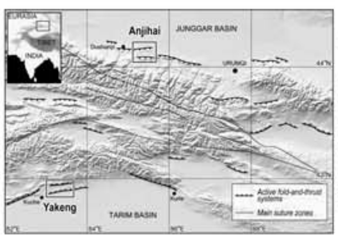

Simplified map of the eastern Tien Shan area. Black boxes mark locations of the folds modeled in this study. Black barbed lines show locations of identified zones of active thrusting and folding. Grey lines show approximate traces of the north Tien Shan and south Tien Shan suture zones.

Sedimentation rates

Our geometric modeling does not directly provide timing information. It does, however, constrain cumulative shortening as a function of stratigraphic depth, which can then be converted to ages using the recent magnetostratigraphic studies of Charreau et al. [2005, 2006] and Charreau [2005]. These studies show evidence for remarkably constant sedimentation rates over the past 10.5 Myr. Between the modern surface and the stratigraphic level of the top of each section, constrained by seismic profiles [Deng fa et al., 2005], average sedimentation rates are very similar to the respective magnetostratigraphic rates since 10-11 Ma. The available local magnetostratigraphic data imply that, at the two sites discussed in this study, old sedimentation rates (10.5 5.2 Ma at Yaha and 10.5 8.5 Ma at Jingou He) may be extrapolated over millions of years, possibly up to Late Pleistocene times, consistent with recent rates of ~0.43 mm/yr near Yakeng and ~0.27 mm/yr near Anjihai.

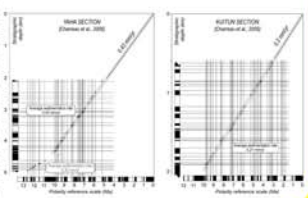

Yakeng fold

At the surface, the Yakeng anticline manifests as a gentle ridge resulting from the folding of a large-scale, south-dipping alluvial terrace (Ta). This structural surface is generally well preserved, although south-flowing rivers dissect it in a number of locations, forming steep, narrow gorges. One of these rivers, (East Quilitag river) formed and abandoned a partially preserved fluvial terrace (Tf). Since then, ongoing deformation has folded and uplifted Tf, bringing it about 25 m above the modern river (Poisson, 2002).

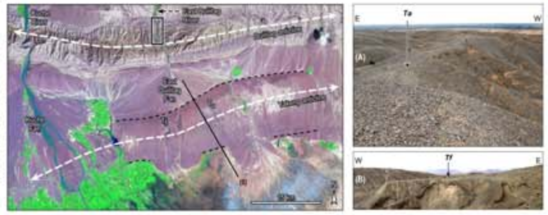

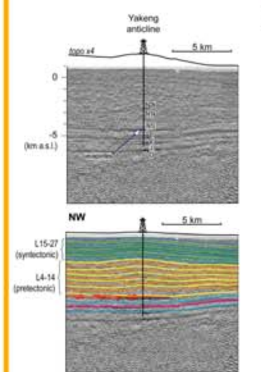

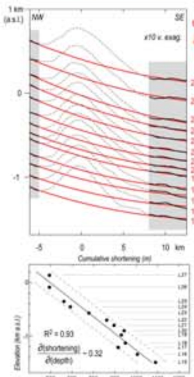

Seismic imaging (Hubert-Ferrari et al., 2005) reveals that the width of the structural fold is more than twice that of the emergent Ta, because the latter is buried under sediments on the outer flanks of the anticline. At depth the amplitude of folding generally decreases downwards, consistent with the geometry of a fault-tip fold growing above a 6-km-deep basal detachment coinciding with reflector L4, in the evaporites of the Oligo-Miocene Jidikeh formation. Gonzalez-Mieres and Suppe (2006), using measurements of thickness relief area, estimated the mean finite shortening to be 1.2km, and showed that folded reflectors L5 to L14 are pretectonic.

Based on the assumed original geometries of the syntectonic seismic reflectors, we estimate their respective amounts of cumulative shortening, and use these values to estimate deformation model parameters consistent with the observed finite geometry. The resulting folding model is used to estimate the cumulative shortening experienced by the geomorphic markers Ta and Tf.

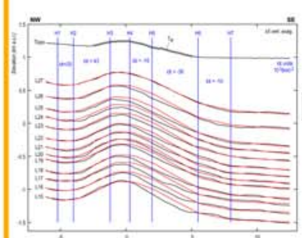

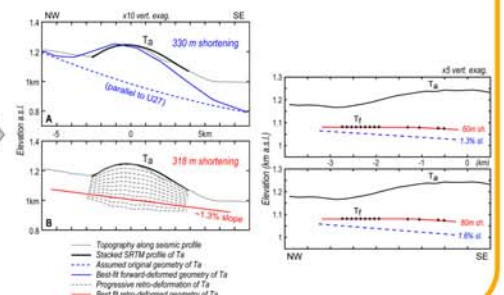

Anjihai fold

The surface fold is about 7 km wide, and exposes conglomerates of the Xiyu (highly diachroneous, Neogene to Quaternary) and Dushanzi (Neogene) formations, unconformably overlain by Quaternary conglomerates and loess. On the flanks of the anticline, such Quaternary structural surfaces are well-preserved, forming triangular cuestas with slopes of 7–10%. We interpret these surfaces (noted Tn and Ts) as folded strath terraces which passively record deformation since their abandonment. Along the steep walls of the river-gap, the shallow structure of the fold is beautifully exposed, with dip angles up to 25°.

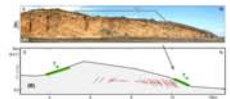

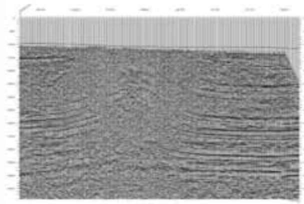

The seismic profile reveals a smooth, rather symmetric subsurface structure strongly suggestive of detachment-driven folding, although the lower part of the section might be suggestive of small-scale ramping near the fold's core. Our line-drawing interpretation of the seismic data allows mapping 7 distinct markers across the fold (L1 to L7). For all seven markers, the structural relief areas are well-correlated with depth, consistent with ~1.5 km of finite shortening over a basal detachment located ~5 km below the surface. We conclude that the sediments below L7 are pretectonic strata.

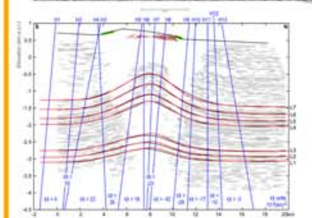

Imposing a finite shortening of 1.55km and a basal detachment depth of 4.5 km b.s.l., we can model the observed finite geometry of the pretectonic markers using a 13-hinge deformation model. The agreement between the predicted and observed dip angles is evidenced when all present-day seismic reflectors are"un-shortened" by 1.55km. Below L7, the retro-deformed reflectors are uniformly flat, whereas above L7 they adopt a syncline-like geometry, implying that these reflectors therefore correspond to growth strata.

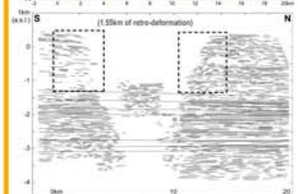

Simple scenarios of shortening (constant shortening & sedimentation rates) provide a good fit to the seismic data alone. However, all of these models predict that the fold should have no or negligible topographic relief, because the sedimentation rate generally exceeds the uplift rate. This is clear indication that the ratio of shortening to sedimentation rates has recently increased.

Two-stage scenarios involving a recent acceleration of shortening yield a better fit to the combined subsurface + surface data set. Additional data is still needed to quantify this acceleration.

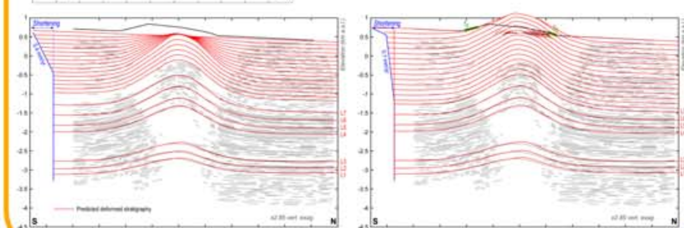

Discussion

The study of these case examples highlights some simple interactions between folding, sedimentation and erosion. Topographic relief can only accrue where and when tectonic uplift is faster than sedimentation (see also discussion in Simoes et al. [2006]). Thus, in the early phases of the histories of both folds, syntectonic sedimentary units extend continuously across the fold, and no topographic relief builds up (A). As shortening rate increases, maximum uplift rates overcome the sedimentation rate, in a zone whose width is a function of the spatial distribution of uplift. As long as the hydrographic system has enough erosion power to sweep laterally back and forth and abrade rocks as they are uplifted, relief remains negligible, and an abrasion surface is emplaced, unconformably overlying older units (B), as observed on the northern flank of Anjihai. If the river is forced to entrench in a narrow gorge because it does not have enough stream power to abrade laterally all the uplifted rocks, relief starts building up above the core of the anticline (C), producing something similar to the current situation of Yakeng. Eventually, the fold ridge is expected to undergo secondary erosion driven by its own relief, as observed in the exposed core of Anjihai.

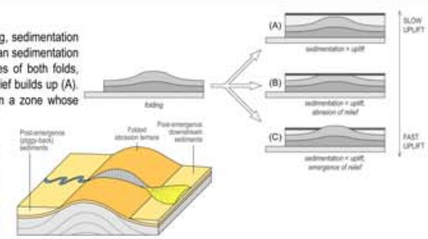

Topographic relief width is thus a function of the spatial distribution of uplift and the sedimentation rates. Shortly after the initiation of relief, the fold width should equate to the width of the area where the uplift rate is greater than the sedimentation rate. Using our parameterized deformation models for the Yakeng and Anjihai folds, we can plot the predicted emergence width as a function of the ratio between the shortening and sedimentation rates. The ratios consistent with the observed fold widths are 5.0 for Yakeng, and 4.15 for Anjihai. Combining the predicted ratios with relevant magnetostratigraphic sedimentation rates yields first-order estimates of the mean shortening rates since relief emergence, 2.15 mm/yr at Yakeng and 1.12 mm/yr at Anjihai, both much faster than the long-term averages. While the precision and reliability of this fold-width method will depend on our ability to understand the complexities of the post-emergence sedimentation regime, surface fold width stands out as a remarkably sensitive measurement, governed as it is by competition between two important geomorphic processes.

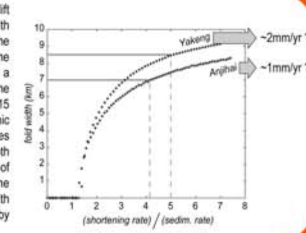

Seismicity in the Mentawai Region of Sumatra Using the Caltech Tectonic Observatory's Local Short-Period Seismic Network

Natalia I Deligne, Robert W Clayton, Erik Hauksson
Seismological Laboratory, California Institute of Technology

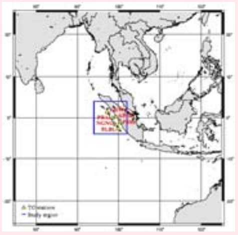

OVERVIEW

A small 6-station seismic array was installed in Sumatra by Caltech's Tectonic Observatory (TO) in May 2005. Each site, co-located with a GPS station, has an L4 1-Hz verticle seismometer recorded by a Nanometrics Taurus 24-bit logger. The data are continuously recorded on site and are retrieved every 3 to 5 months. Events are located using SEISAN. To date, 1094 earthquakes have been located for the period from May 19th - August 4th 2005. In general, for the entire study region (4N - 4S, 94E - 102E) only about 20% of the located earthquakes have also been located by the National Earthquake Information Center (NEIC), suggesting that background seismicity is far greater than previously estimated. In the region near Nyang Nyang island, the NEIC reports almost no events, but the TO stations pick up considerable activity. Most of the located earthquakes appear to be M4 - M5.

SEISMICITY LOCATION

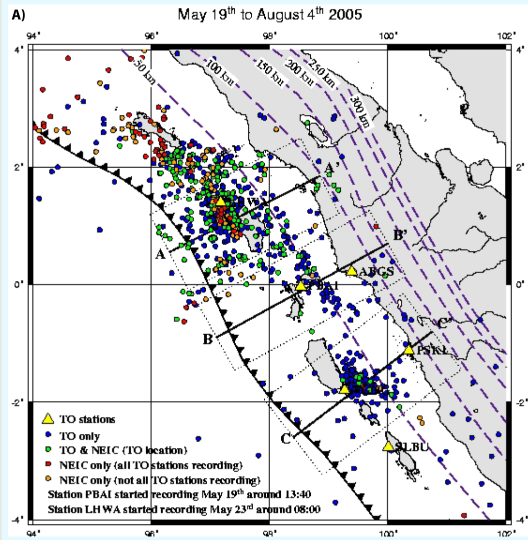

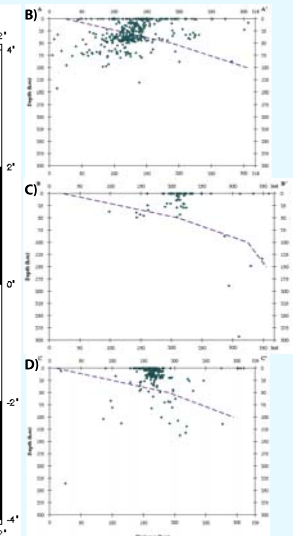

A) All located earthquakes in the study region (4N - 4S, 94E - 102E) for the period from May 19th - August 4th 2005, with the locations for crosssections for figure parts B, C, and D indicated. TO stations are shown as yellow triangles. Events were located from TO waveforms using SEISAN, and a minimum of four stations had a signal for an event to be located. Events in blue are only located by the TO, green events are located by both the TO and the NEIC, while red and orange events have only been located by the NEIC. For most such events, however, at least one or two TO stations picked up the signal. Slab contours are based on global seismicity (Gudmundsson and Sambridge, 1998).
B) Cross-section across the northern portion of the study region. For this and the other cross-sections, only TO-located earthquakes are shown (i.e. blue and green events on location map).
C) Cross-section across the central region. Note the linear feature occuring about 200 km from the trench, going to a depth of 50 km. Although focal mechanism have not yet be done, such a linear feature suggests strike slip motion. Earthquakes not along this feature seem to match the suggested slab location pretty well.
D) Cross-section across the southern portion of the study region. There is a lot of activity at shallow depth above the presumed slab location. This region was selected fo the double difference relocation study (see below)

SAMPLE WAVEFORM DATA

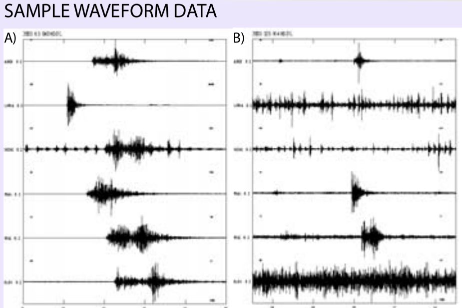

A) Example of event with high-quality signal. The NEIC reports this earthquake as having a magnitude of 5.8; the epicenter we obtained for this event is 1.579 N, 96.845 E with a depth of 19.3 km (the NEIC reports location / depth of 1.46 N, 97.15 E, 24 km). Note the regular spikes at station NGNG corresponding to the surf.
B) Example of typical data. This event was not located as less than 4 stations recorded a signal. Note the noise at station LHWA, the extreme noise at station SLBU (this is what most of the data from station SLBU looks like), and the regular spikes at station NGNG corresponding to the surf.

DATA QUALITY

The two land-based stations (ABGS and PSKI) have the clearest signal. Proximity of an earthquake also strongly influences clarity of signal at a given station. Station PBAI has the clearest island-based signal. Station LHWA has a relatively good signal, and records numerous events, presumably to the north of the array, that are not recored by any other staions. Station NGNG records the surf at a nearby beach, while station SLBU is exceedingly noisy.

AVAILABLE DATA FOR 2005

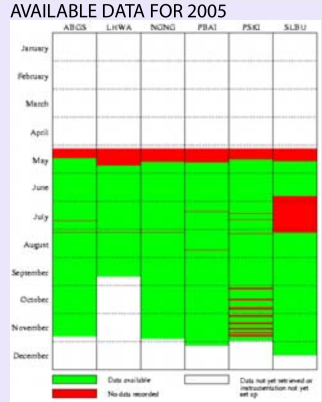

White indicates there is no data available either because instrumentation was not yet set up or because data has yet to be retrieved, green indicates that there is data, and red indicates that the instrument was not recording.

DOUBLE DIFFERENCE RELOCATION

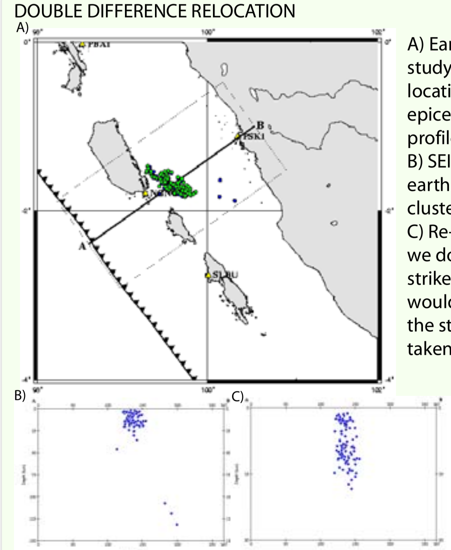

A) Earthquakes selected for the double difference relocation study. Blue circles correspond to the original SEISAN-based TO location, and the green circles correspond to the re-located epicenter. TO stations are yellow triangles, and the cross-section profile is indicated.
B) SEISAN-based location cross-section. The three deeper earthquakes are the three earthquakes outside of the main cluster on the location map.
C) Re-located events. Note the strong linear feature; although we do not yet have focal mechanism, this feature suggests strike-slip motion. If this activity is indeed strike slip motion, this would imply that the Great Sumatran Fault does not take up all the strike-slip motion along the Sunda arc; there is a component taken off shore closer to the trench.

FUTURE WORK

In the future, we plan to :
1) Update the current 1D velocity model, with the aim of eventually developing a 3D velocity model
2) Calibrate the amplitude from the stations to be able to determine earthquake magnitude.

Unroofing of the southwestern Colorado Plateau from (U-Th)/He apatite thermochronometry

Rebecca M. Flowers (rflowers@gps.caltech.edu), Brian P. Wernicke, and Ken A. Farley
California Institute of Technology, Division of Geological and Planetary Sciences

ABSTRACT

The timing and mechanism of uplift of the Colorado Plateau by ~1.9 km since the Cretaceous is a major question in Cordilleran tectonics. Resolving when the Colorado Plateau was unroofed can provide some insight into this problem, because erosional denudation commonly is linked with uplift. New (U-Th)/He apatite data constrain post-Cretaceous denudational patterns in the Grand Canyon region of the southwestern Colorado Plateau.

(U-Th)/He dates for individual detrital apatites from fourteen Moenkopi sandstone samples across this area 1) are significantly younger than the depositional age of the unit, indicating partial to complete He loss following deposition, and 2) display dates that are younger with increasing distance from the plateau margin, reflecting an overall pattern of southwest to northeast stripping of the overlying sedimentary package. Individual apatites from five Tertiary rim gravel samples did not undergo significant He loss following deposition, such that the distributions of dates reflect the denudation of source regions and impose a maximum timing constraint on gravel deposition following unroofing to the modern plateau surface. Our results suggest that the current plateau margin was buried by > 1.5 km of Cretaceous sediments prior to pulses of denudation in the Laramide and mid-Tertiary (40-35 Ma) that may be linked with uplift episodes at these times. Each denudational pulse was followed by rim gravel aggradation. A component of unroofing ca. 30-20 Ma is likely associated with drainage reversal across the Mogollon rim. Significant late-Tertiary unroofing and scarp retreat is most simply explained by integration of the Colorado River at 6 Ma that provided a mechanism to efficiently remove large sediment volumes from the plateau. A mid-Tertiary ancestral Colorado River in the eastern Grand Canyon is permissible by the current dataset, and $^4He/^3He$ thermochronometry on basement samples is underway to better resolve the timing of canyon incision.

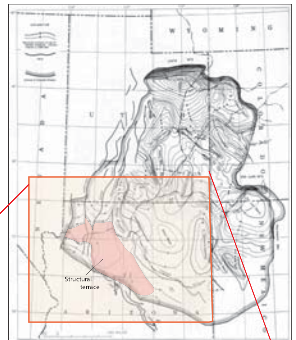

Stratigraphic Section

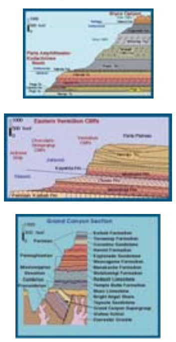

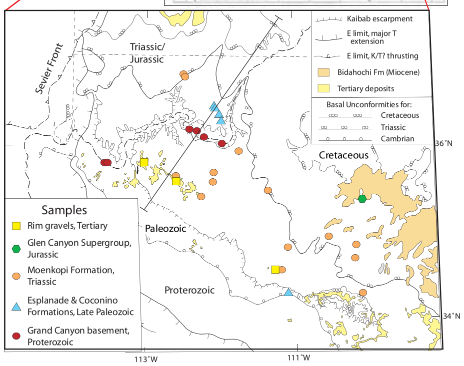

GRAND CANYON REGION OF THE COLORADO PLATEAU

The southwestern portion, or Grand Canyon region, of the Colorado Plateau is characterized by a broad (~15,000 km2) gently NE-dipping structural terrace that is interrupted by the N-trending Kaibab uplift. The plateau surface resides at an elevation of 1500 to 2000 m, is underlain by the resistant Permian Kaibab limestone, and preserves discontinous exposures of fluvial sandstone of the Triassic Moenkopi Formation. To the northeast, progressively younger Mesozoic and Cenozoic formations are exposed in a series of cuestas known as the "Great Rock Staircase". To the west, the plateau edge is structurally delineated by major normal faults of the Basin and Range Province. The Colorado River currently drains the Colorado Plateau to the southwest, forming the Grand Canyon where it cuts across the topographically high southwestern plateau and incises to depths as great as 1600m.

The Mogollon rim, extending 500 km in a northwest trend across Arizona, is primarily an erosional feature that separates the Colorado Plateau from Precambrian basement of the Transition Zone (e.g. Peirce, 1979). Tertiary Rim gravels are preserved immediately north of the Mogollon Rim, and record northeastward transport and unroofing of the Laramide Mogollon highlands to the southwest (Young, 1979; Potochnik, 1989). Locally, in the extreme western Grand Canyon, deeply incised channels containing preserved Rim gravels have >1200 m of relief (Young, 1989, 2001; Elston and Young, 1991; Billingsley et al., 1999). Drainage reversal across the Mogollon rim is inferred to have occurred ca. 30-20 Ma. The thin (~100 m) areally extensive Bidahochi Formation records fluvial and lacustrine aggradation from ~16 to 6 Ma (Dallege et al., 2001).

RADIATION DAMAGE CONTROL ON APATITE (U-TH)/HE DATES

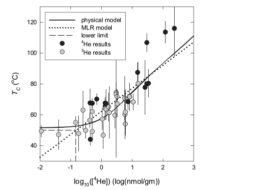

Apatite helium closure temperature (Tc) versus the log of the ^{4}He concentration., for stepwise degassing experiments on 39 different apatite samples. Tc is positively correlated with [He] and is interpreted to be a proxy for accumulated radiation damage. Values of Tc were calculated for a cooling rate of 10 C/m.y. Figure 1, Shuster et al., 2006.

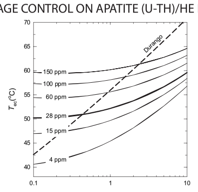

Effective closure temperature (Tec) as a function of cooling rate and [eU] computed from the radiation-damage trapping model. Results for conventional Durango diffusion kinetics are also shown. Figure 5, Shuster et al., 2006.

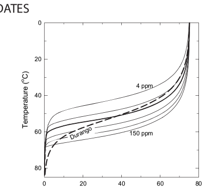

The He partial retention zone calculated for apatites of differing [eU] that are held at the indicated temperatures for 75 m.y. for the radiation-damage trapping model and conventional Durango diffusion kinetics. Figure 6, Shuster et al., 2006.

Generic Burial and Unroofing Models

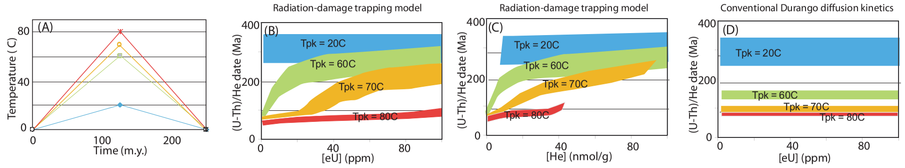

The radiation-damage trapping model incorporates He diffusion kinetics that evolve with temperature and [He]. We simulated distributions of dates expected for detrital grains of uniform diameter (100 um) characterized by an arbitrary but reasonable range of [eU] (2-100 ppm) and (U-Th)/He provenance dates (AHe date of the apatite when deposited, AHedep) from 5 to 100 Ma. We first consider monotonic heating and cooling (A), and display the results in (B) and (C). For comparison we show the results for a model that assumes conventional Durango apatite He diffusion kinetics (D).

A Tpk of 20 °C is insufficient to cause He loss from any of the apatites, such that the final distribution of dates mimics the provenance distribution, and is independent of [eU]. For Tpk of 60 °C, apatites with the lowest [eU] (least radiation damaged and lowest Tec) undergo complete He loss and thus yield the youngest dates, while apatites with higher [eU] (more radiation damaged and higher Tec) are incompletely reset under the same conditions and so yield older dates. Increasing Tpk to 70 °C induces greater resetting of apatites with higher [eU]. A Tpk of 80 °C causes nearly complete He loss in all apatites, thereby generating a fairly uniform population of dates. Thus, burial and unroofing simulations characterized by no resetting show no correlation between date and [eU], and those affected by complete resetting yield dates that cluster fairly tightly. Only those simulations that include an episode of partial He loss can generate broad distributions of AHe dates that correlate with [eU] and [He], due to divergence of He retentivities in the apatite suite prior to partial resetting.

(U-Th)/He RESULTS

Triassic Moenkopi Formation, 14 samples (N = 114)
Permian Esplanade & Coconino Formations, 5 samples (N = 34)

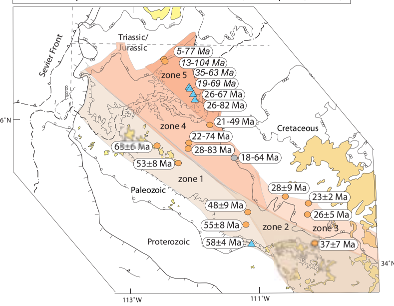

Proterozoic Grand Canyon basement, 6 samples (N = 25)
Tertiary Rim gravels, 4 samples (N = 22)

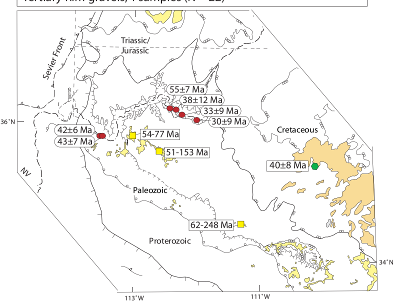

Three clear patterns emerge from the AHe dataset. First, the apatite dates are younger to the northeast with increasing distance from the Mogollon rim and in closer proximity to the modern scarp formed by the Mesozoic and Cenozoic units. Second, dates along the southeastern Mogollon rim (zone 2) are younger than those along its northwestern segment (zone 1). Third, apatites along the Mogollon rim (zones 1, 2, 3) yielded more consistent dates than apatites to the northeast (zones 4, 5). For this reason, results for the former are reported as weighted mean dates, while the span of dates is reported for the latter samples. Zone 5 samples are characterized by large ranges of dates correlated with [eU] and [He], and can be explained by the effect of radiation damage on He retentivity (see below).

Grand Canyon basement - We targeted crystalline basement from the Upper and Lower Granite Gorges because these rocks typically are characterized by more abundant apatite than the sedimentary units that are exposed elsewhere in the canyon. With the exception of one sample characterized by high [eU], apatites from the other samples yield younger dates in the eastern than in the western Grand Canyon.

Tertiary rim gravels - The heterogeneous dates, including results significantly older than the Tertiary depositional age of the unit, indicate that the apatites did not undergo significant He loss following deposition. The youngest AHe dates of ca. 50 Ma provide a maximum constraint on gravel aggradation.

Zone 1 - Detrital Apatite Data

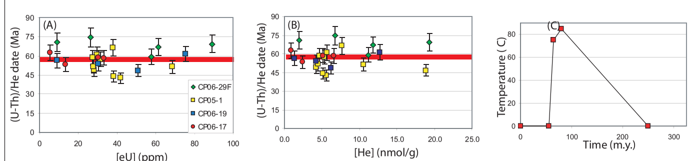

(A) (B) Individual detrital AHe dates (symbols) as a function of [eU] and [He]. (C) Simulated thermal history, with simulated distributions of dates using the radiation damage trapping model depicted as shaded fields in (A) and (B). Samples from zones 1 can be explained by a single pulse of Laramide cooling/unroofing. These samples show fairly uniform dates, despite broad [eU] and [He] variation. This is most simply explained by peak temperatures in zone 1 that were higher and/or were maintained longer than those in zone 5, and induced complete He loss from all the apatites. We attribute these higher temperatures to the proximity of zone 1 samples to magmatic and orogenic activity in the Sevier and Mogollon orogenic systems.

Zone 5 - Detrital Apatite Data

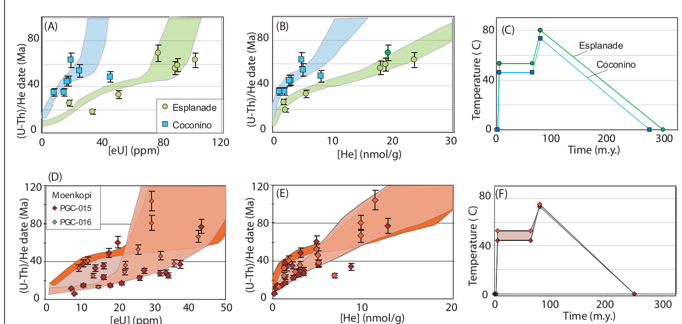

Individual detrital AHe dates (symbols) as a function of [eU] and [He]., for the Esplanade and Coconino samples (A) and (B), and Moenkopi samples (D) and (E). (C) Simulated thermal histories used to reproduce the Esplanade and Coconino data distributions using the radiation damage trapping model, with simulated distributions depicted as shaded fields in (A) and (B). (F) Simulated thermal histories used to reproduce the Moenkopi data using the radiation damage trapping model. with simulated distributions of dates depicted as shaded fields in (D) and (E). A single thermal history does not generate the entire spread of data, so we depict endmember thermal histories that together encompass the fan of data. Two endmember simulated distributions are depicted as separate, but overlapping, shaded fields in (D) and (E). The distributions of dates in all six samples analyzed from zone 5 can be explained by a two-pulse exhumation model involving episodes of cooling in the Laramide and Miocene (Flowers et al., in review). In contrast to the samples in zone 1, we infer that these apatites underwent incomplete He loss during burial.

RADIATION DAMAGE CONTROL ON (U-Th)/He APATITE DATES FROM THE SOUTHWESTERN COLORADO PLATEAU

Our results from zone 5 of the Grand Canyon region of the Colorado Plateau suggest that the increase in apatite He retentivity due to radiation damage, implied by laboratory diffusion data, is important for the interpretation of data in certain geological settings. Forward models predict that the effect of radiation damage on He retentivity will be manifested in suites of apatites with a range of [eU] that underwent a history in which the apatite He diffusion kinetics had sufficient time to diverge prior to an episode of partial resetting. A common geological history that satisfies these requirements is one like that in the Grand Canyon region involving 1) deposition of compositionally diverse apatites with variable provenance dates in sedimentary units, and 2) burial, partial He loss, and subsequent exhumation. The data suggest that in some situations, a span of AHe dates positively correlated with [eU] is geologically meaningful. Our simulations predict that the correlations between AHe date, [He] and [eU] can be very sensitive to the thermal history. Thus, it may be possible to extract additional information regarding the details of the temperature-time path from these relationships than would be possible in a sample characterized by a uniform distribution of apatite dates.

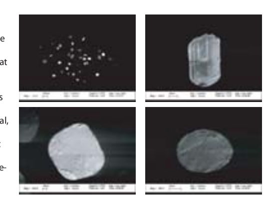

CL images of apatites from Moenkopi sample PGC-015 that display variable brightness and zoning characteristics.

UNROOFING THE COLORADO PLATEAU

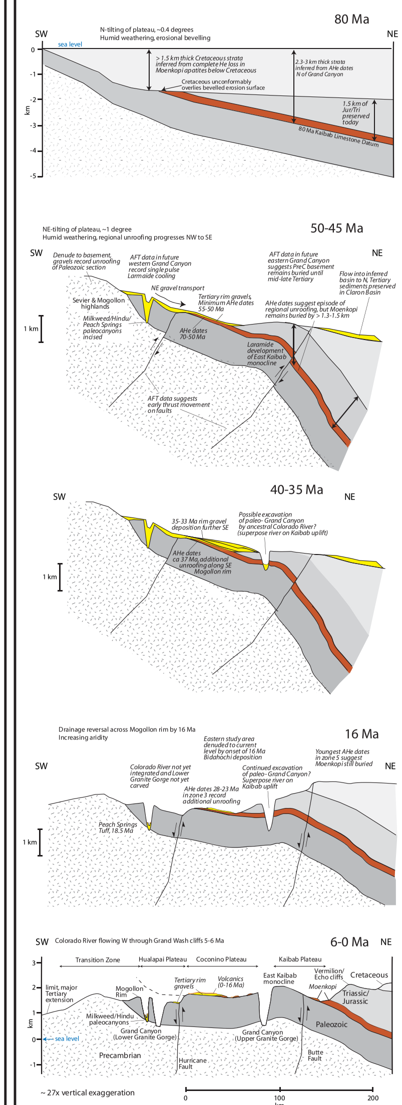

REFERENCES

Billingsley, G. H., Wenrich, K.J., Huntoon, P.W., and Young, R.A., 1999, Breccia-Pipe and geologic map of the southwestern part of the Hualapai Indian Reservation and vicinity, Arizona: U.S. Geological Survey, Geologic Investigations Series, scale 1:48,000.

Dallegge, T. A., Ort, M.HY., McIntosh, W.C., and Perkins, M.E., 2001, Age and depositional basin morphology of the Bidahochi Formation and implications for the ancestral Upper Colorado River, in Young, R. A. a. S., E.E., ed., Colorado River Origin and Evolution, Grand Canyon Association, p. 47-52.

Elston, D. P., and Young, R. A., 1991, Cretaceous-Eocene (Laramide) Landscape development and Oligocene-Pliocene drainage reorganization of Transition Zone and Colorado Plateau, Arizona: Journal of Geophysical Research-Solid Earth and Planets, v. 96, no. B7, p. 12389-12406.

Farley, K.A., 2000, Helium diffusion from apatite: General behavior as illustrated by Durango fluorapatite: Journal of Geophysical Research, v. 105, p. 2903-2914.

Flowers, R.M., Shuster, D.L., Wernicke, B.P., and Farley, K.A., in review, Radiation damage control on apatite (U-Th)/He dates from the Grand Canyon region, Colorado Plateau: Geology.

Pierce, H. W., Damon, P.E., and Shafiqullah, 1979, An Oligocene (?) Colorado Plateau edge in Arizona: Tectonophysics, v. 61, p. 1-24.

Potochnik, A.R., 1989, Depositional style and tectonic implications of the Mogollon Rim Formation (Eocene), East-Central Arizona: new Mexico Geological Society Guidebook, 40th Field Conference, Southeastern Colorado Plateau, p. 107-118.

Shuster, D.L., Flowers, R.M., and Farley, K.A., 2006, The influence of natural radiation damage on helium diffusion kinetics in apatite: Earth and Planetary Science Letters, v.249, p. 148-161.

Young, R. A., 1979, Laramide deformation, erosion and plutonism along the southwestern margin of the Colorado Plateau: Tectonophysics, v. 61, p. 25-47.

Young, R. A., and Spamer, E. E., 2001, The Laramide-Paleogene history of the western Grand Canyon region: Setting the stage, in Young, R. A. a. S., E.E., ed., Colorado River Origin and Evolution, Grand Canyon Association, p. 47-52.

GPS at CTO: Geodetic Arrays and Data Processing

Jeff Genrich, John Galetzka, Jean-Philippe Avouac, Kerry Sieh, Mark Simons, and Brian Wernicke

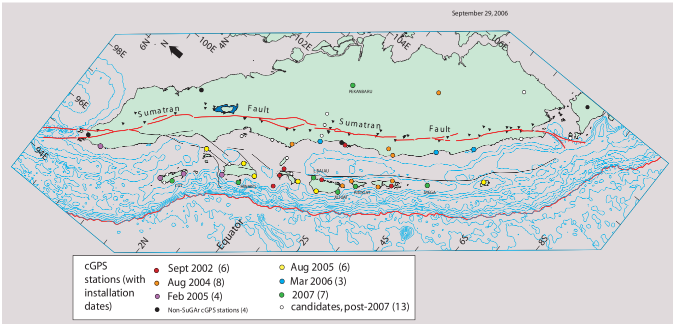

Figure 1. Map location of existing and future SuGAr sites in Sumatra.

Introduction and Current Status

CTO operates 4 medium size GPS geodetic arrays at or near plate boundaries. Two arrays are located near prominent subduction zones, a third monitors deformation in a continent-continent collision setting, and a forth measures displacement in an extentional environment. Established in 2002, the 27-station Sumatra GPS Array (SuGAr) occupies the Sumatran forearc from Enggano in the South to small islands north of Simeulue (Figure 1). With measurements starting in 2005, 11 stations of the Central Andean GPS Array (CAGA) span northern Chile from the Peruvian border to Antofagasta (Figure 2). Since 2004, data from 9 CTO stations in Nepal (Figure 3) add substantially increased spatial resolution to measurements from 3 pre-existing permanent sites in the area. The 71-site Basin and Range Geodetic Network (BARGEN) has been a collaborative project between Caltech and Harvard since 1996. Recent CTO efforts focus on a 31-station subset of BARGEN (Figure 4). CTO also contributed 3 stations in tectonically important, hard-to-access locations of the Central Range to the Taiwan GPS Network.

Station Design

Basic station design is similar for all networks (Figures 5 and 6). A tripod, formed by welded stainless steel tubing resting in drill holes, is anchored to the subsurface by epoxy and supports the radome equipped GPS choke-ring antenna. A 30 m coaxial cable carries the L-band satellite signals from the preamplifier (located at the base of the antenna) to the GPS receiver. The receiver is housed in a steel equipment box together with ancillary electronic and electrical equipment (Figure 7). The station is powered by 2 50-80 W-rated solar panels that charge 2 deep cycle, 70-100 Ah-rated gel cells. Where feasible, communications with the receiver is facilitated by radio links.

Data Retrieval

Data from SuGAr sites are downloaded in daily batches to a central internet hub in Batam, Indonesia, through low bandwidth serial port modems of a regional communications satellite. Several CAGA sites have internet links by long range Ethernet radio bridges terminating at internet hubs of local universities (Arica and Antofagasta) or of municipal administrations (Putre). The Nepal network, located in a challenging environment, currently relies exclusively on periodic on-site manual downloads.

Future Development

Site Augmentation

A major addition of sites is scheduled for all CTO-run networks. For SuGAr, a densification in certain key areas (Figure 1) will help to account for research activities related to the different stages of the seismic cycle for different parts of the network. For CAGA, targeted new sites near the coast and the Andean foothills will narrow the wide spacing of the existing array, while expansion into southern Peru and western Bolivia and Argentina will capture a much larger area of the plate margin. Near-future developments of the Nepal array call for a major deployment of new sites in the western half of the country. A trans-Himalayan expansion is currently underway with several sites in Tibet.

Real time Data Streaming

If site measurements can be transmitted in near real time to central processing facilities, GPS geodetic networks located near plate boundaries will potentially yield important contributions to natural hazards early warning systems, Three CAGA sites (ATJN, PCCL, PTRE) currently have internet links. Links to two additional sites (JRGN, MCLA) have been tested successfully. Near real time data links for SuGAr have been explored earlier this year at the central facility of the satellite communications provider (ACeS) in Batam. Using existing (low bandwidth) modems, data stream with a sampling interval of about 5 sec. were forwarded to CTO with a latency of several seconds. Employing a higher bandwidth satellite Ethernet radio bridge yielded subsecond latencies for data streams of 1 or 2 Hz. Efforts to expand real-time connectivity are underway for all CTO networks.

Data Processing

The displayed time series of station positions (Figures 8 and 9) show a long term, approximately linear trend that reflects crustal motion. This tectonic signal is superimposed by noise from a variety of sources. Depending on their origin, there are temporally correlated aperiodic and periodic components with annual, semi-annual, or diurnal contributions. Local- (multipathing), regional-, and reference frame-induced errors produce additional, spatially correlated noise. Eliminating or reducing these contributions with the help of suitable models and filters will be a significant part of future work.
With an increasing number of on-line data streams, it will also become necessary to develop proper tools for near real time data processing and analysis.

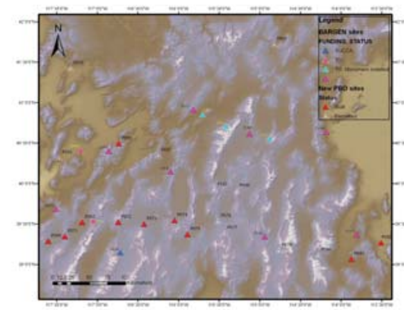

Figure 4. Map location of CTO subnetwork of BARGEN.

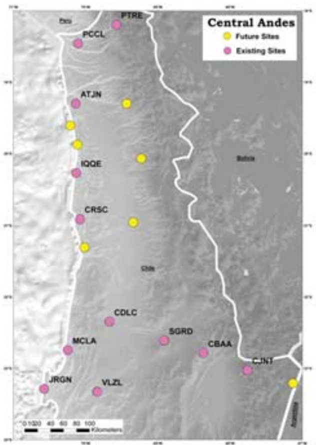

Figure 2. Map location of existing and future CAGA sites in northern Chile

Figure 5. CAGA station ATJN in northern Chile. Equipment box, solar panels, and ethernet link radio antenna in the foreground, GPS tripod and antenna in the background.

Figure 6. CAGA station PTRE.

Figure 7. Interior of equipment box for station PCCL. Solar panel control unit and ethernet radio located above batteries, GPS receiver below.

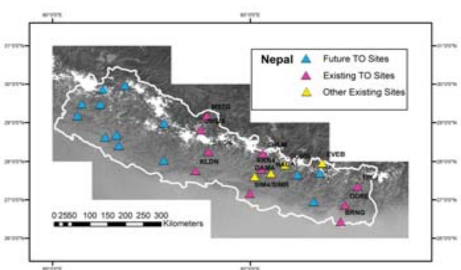

Figure 3. Nepal GPS network. Map location of existing and future sites.

Data Processing

For each 24 hour time period, all available raw receiver image files are converted to Ascii Rinex format. Using the GAMIT software package, local Rinex files are processed with corresponding phase observations from nearby global reference stations to yield daily station positions with respect to a loosely constrained global reference system. Refined ITRF 2000 daily positions are then computed by a Kalman Filter (GLOBK) with the help of solutions from several global (IGS) networks. North-, east- and up-components of the daily station positions are displayed on network specific web pages (Figures 8 and 9).

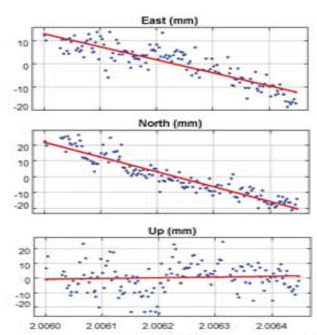

Figure 8. East-, north-, and up components of daily positions for SuGAr site LEWK in ITRF2000.

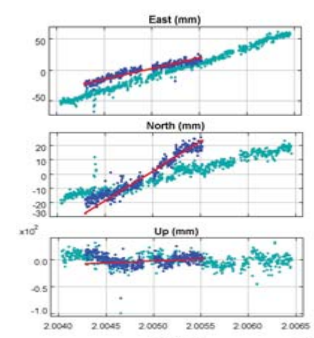

Figure 9. East-, north-, and up- components of daily positions for Nepal site KLDN (blue) and global reference site LHAS (green) in ITRF2000.

Geodynamic models for the "uplift" and erosion of the Colorado Plateau

Frederic Herman and Mike Gurnis

Tectonics Observatory, Geological and Planetary Science
California Institute of Technology

Our aim is to test a range of geodynamic models that can explain the uplift of the Colorado Plateau, if uplift there was. Many mechanisms have been proposed and summarized in the literature [e.g. McGetchin 1980]. The main mechanisms fall in three different categories: (a) Late Cretaceous to early tertiary uplift related to Sevier-Laramide orogeny (80 to 40 Ma) [e.g. McQuarrie and Chase 2000]; (b) mid-Tertiary uplift related to removal of flat subduction (either through mechanical thinning of continental mantle lithosphere and subsequent removal of flat slab [Spencer 1996], release of negative dynamic topography [Mitrovica et al 1989, Gurnis 1992] or hydration of the lithosphere from volatiles derived from the Farralon slab [Humphries et al 2003]) and (c) Late-Tertiary uplift associated with regional extensional tectonism, either by large removal of instable lithosphere [Bird 1979] or heating from below. We propose to test these geodynamic models using the codes available through the Computational Infrastructure for Geodynamics framework.

We use a mantle convection model, so-called CitcomT [e.g. Billen et al 2003] CitcomT is a solving the equations of momentum, continuity and transport equations :

$$u_{i,i} = 0,$$

$$-P_{,i} + (\eta u_{i,j} + \eta u_{j,i})_{,j} + Ra\delta\rho\delta_{ir} = 0,$$

$$(\delta\rho)_{,t} + u_i(\delta\rho)_{,i} = (\delta\rho)_{,ii},$$

in 3D and in spherical coordinates.

It computes dynamic topographies using the boundary flux method [Zhong et al 1993].

The viscosity varies laterally and is temperature-pressure dependant. Lateral and radial viscosity variations can be included in the model, by setting the effective viscosity to the desire value in a given region.

The code to account for regions that are chemically different [Moresi 1998] to simulate continental lithosphere/tectosphere. It is important to note that this implementation includes the computation of the advection of the chemically different layer.

We present three models which test the hypothesis of uplift of the Colorado Plateau due to removal of the the flat subduction. In each model, we include a buoyant continental tectosphere that is shaved by the flat subduction. In each model, decoupling between the subducting plate and the overiding lithosphere is ensured by including a region of low viscosity between the two. Model 1 simulates an abnormally thick oceanic lithosphere below the plateau, Model 2 assumes a thinner oceanic plate and Model3 is equivalent to model 2 except that the zone of decoupling is made larger.

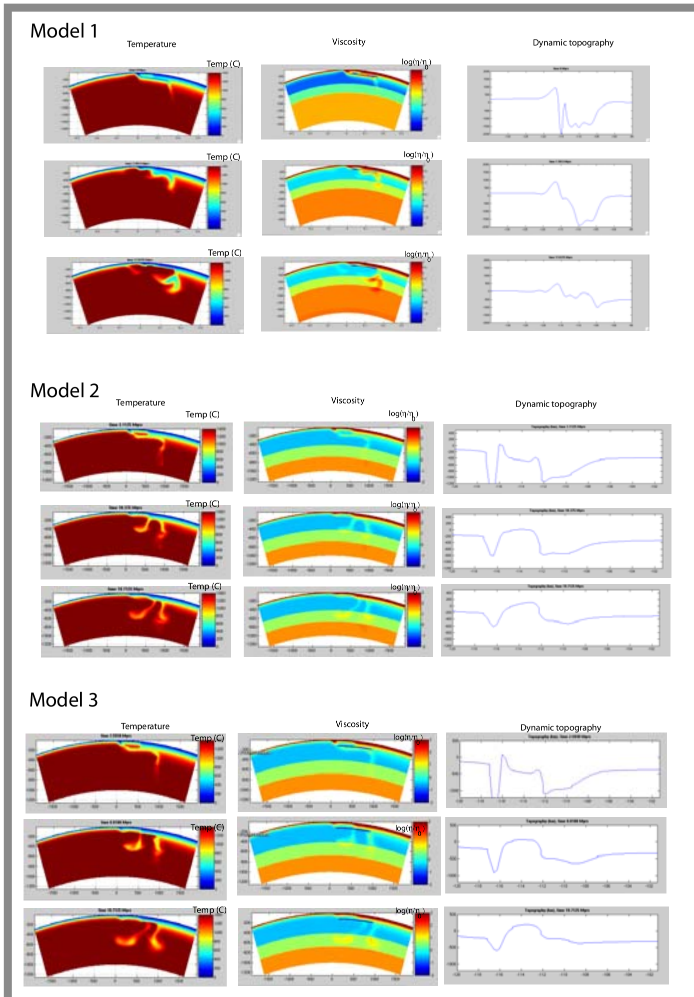

(a) begining of simulation

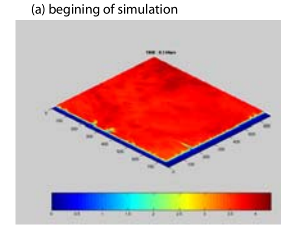

(b) erosion along the edges of the plateau

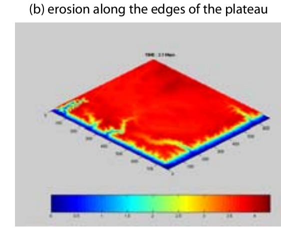

(c) begining of incision of the Grand Canyon

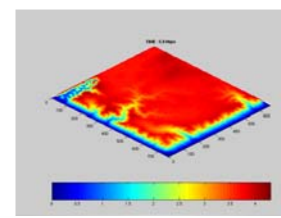

We here use a Surface Process Model, which simulates the evolution of hillslope and river incision. We present an example of a simulation.
The model starts with a base level drop. Consequently, erosion is induced at the edges of the plateau. This, in turn, causes isostatic uplift on the edges of the plateau, slowing down erosion along these scarps and forming an internally drained basin. Ultimately, the basin will overfill and lead to rapid erosion along the Grand Canyon.

Computations were perfomed on the Pangu facilities at the Geological and Planetary Sciences Division, California Institute of Technology

Thermal modelling of metamorphism and exhumation in Western Nepal and India

Frederic Herman*, Jean-Philippe Avouac*, Amos Aikman+, Julien Celerier+, Mark Harrison @
* Tectonics Observatory, California Institute of Technology
+ Research School of Earth Sciences, Australian National University
@ Department of Earth and Space Sciences, University of California Los Angles

The geological association of the Himalayan range is a juxtaposition of inverted metamorphic sequences in the footwall of the Main Central Trust (MCT) with a belt of Miocene leucogranites emplaced above the fault (Figure 1). The MCT extends across the 2500 km length of the Himalayan orogen and is the dominant structural feature of that mountain belt.

The inverted metamorphic sequences beneath the MCT ramp has been interpreted as a reactivation of the thrust following ~10 m.y. of inactivity [e.g. Harrison et al 1997]. Measured monazite ages from the lower Lesser have been used to interpret reactivation of the MCT at ca. 8 Ma and activation of the MCT Zone at ~6 Ma. More recently, Bollinger et al 2004 and 2006 showed that shortening across the Himalaya can be explained by accommodation by a single fault, the Main Himalayan Thrust (MHT), and that the growth of Himalayan wedge has resulted from underplating and development of a duplex. In this latter scenario, the MCT zone corresponds to the MHT exhumed at the surface.

In both instances, an increase of exhumation from about 8 Ma is required. We test here these models in Far West Nepal and India, where new thermochronological data have been collected (Ar39/Ar40 in muscovite, Raman Spectrometry and (U-Th)/He in zircon). We use a thermal-kinematic model which solves the heat transfer equation coupled with an inversion algorithm, the Neighbourhood Algorithm (Sambridge 1999).

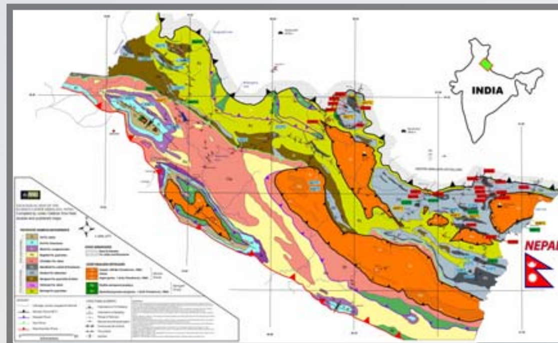

Figure 1: Geological map (courtesy of Julien Celerier)

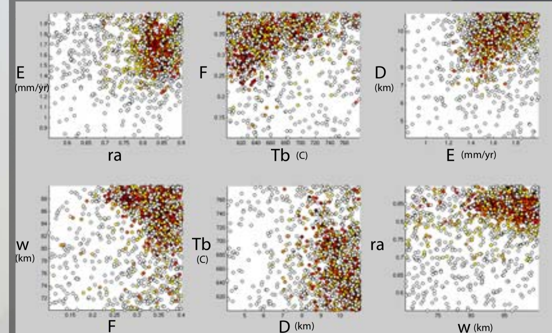

Figure 3: Inversion of thermal model. Each dot represents a forward model in the parameter space (white dots=low fit, red dots=goof fit)

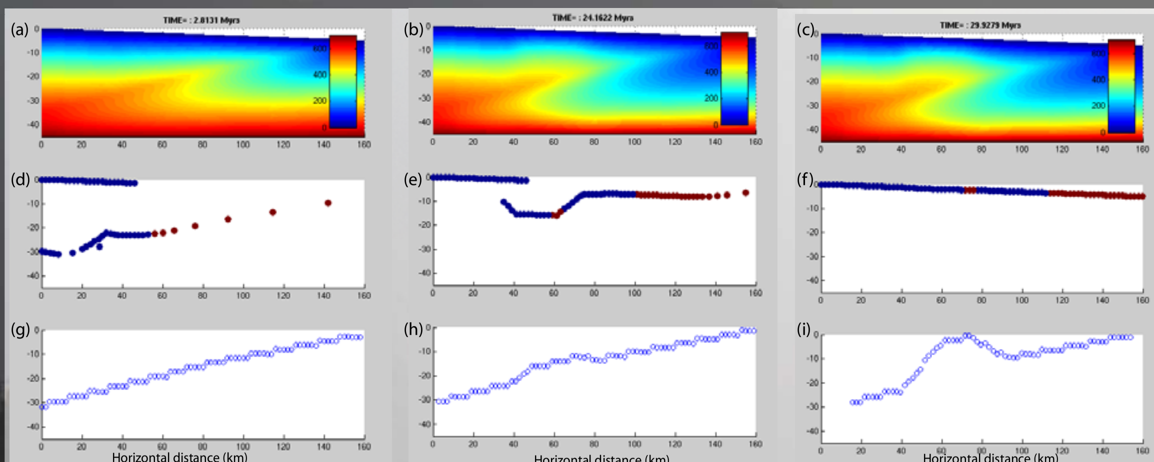

Figure 2: Evolution of thermal model (a)-(c) Thermal structure, (d)-(f) particles paths for rocks that end up at the surface at the end of the run, (g)-(i) evolution of MHT during model run.

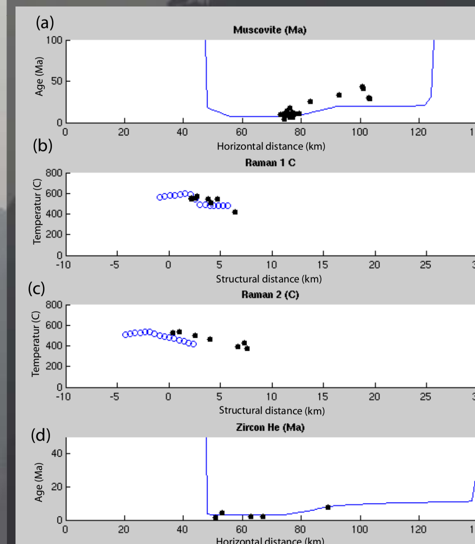

Figure 4: Fit to the data for a forward which minimizes the misfit. Black color scheme depicts data and blue model output.
(a) Ar39/Ar40 in muscovite vs. horizontal distance
(b) Raman peak temperature vs. structural distance near the MCT
(c) Raman peak temperature vs. structural distance 30 km south of MCT
(d) (U-Th)/He in zircon ages vs. structural distance

References
Harrison, T.M., et al 1997, A late Miocene-Pliocene origin for Central Himalayan inverted metamorphism, Earth and Planetary Science Letters, 146, p. E1-E8.
Bollinger, L., et al 2004. Thermal structure and exhumation history of the lesser Himalaya., Tectonics
Sambridge 1999, Geophysical Inversion with a Neighbourhood Algorithm -I. Searching a parameter space Geophys. J. Int., 138, 479-494

Computations were performed on the Pangu facilties at the Geological and Planetary Sciences, California Institute of Technology.

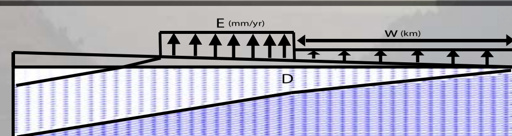

Figure 5: Kinematics used in thermal model. There is a window of accretion, the upper plate overthrust the lower plate at (1-ra)*v, with v being the total shortening rate.

Spectral element modeling of earthquake nucleation and spontaneous rupture on rate and state faults

Yoshiro Kaneko[1], Nadia Lapusta[1,2], Jean Paul Ampuero[3]

1. Division of Geological & Planetary Sciences, Caltech, Pasadena, CA
2. Division of Engineering & Applied Science, Caltech, Pasadena, CA
3. Institute of Geophysics, Seismology & Geodynamics, ETH, Zürich
E-mail: ykaneko@gps.caltech.edu

1 Introduction

Nucleation and spontaneous dynamic propagation of earthquakes on rate and state faults have been successfully modeled in the framework of boundary integral methods (BIM) (*Rice and Ben-Zion*, 1996; *Lapusta et al.*, 2000). However, these studies have been mostly restricted to planar faults embedded into a uniform elastic space or half-space, due to the nature of BIM. At the same time, observations show complicated crustal structures (such as layering and fault damage zones) and non-planar fault geometries. It is important to include those factors into earthquake models, combining them with laboratory-derived constitutive fault relations such as rate and state friction. In this work, we use 3-D spectral element method (SEM) to model earthquake nucleation and propagation of spontaneous rupture on a vertical strike-slip fault governed by rate and state friction. Our ultimate goal is to develop a SEM framework for simulating long-term deformation histories, in terms of sequences of earthquakes and combination of seismic and aseismic sliding.

2 Spectral element method (SEM)

- Flexibility of a finite element method and accuracy of a pseudo-spectral method
- Successfully applied in computational fluid dynamics and seismic wave propagation
- Diagonal mass matrix and explicit time scheme

3 Boundary integral method (BIM)

- Only the boundary (on the fault) is discretized
- Wave propagation is accounted for analytically through theoretically derived kernels
- Accurate and efficient but relatively limited in terms of geometry and bulk properties

4 Rate and state dependent friction

In the standard formulation with constant effective normal stress $\bar{\sigma}$, the shear strength τ can be expressed as:

$$\tau = \bar{\sigma}\mu = \bar{\sigma}\left[\mu_0 + a\ln(V/V_0) + b\ln(V_0\theta/L)\right]$$

$$d\theta/dt = 1 - V\theta/L \quad \text{(aging law)}$$

$$d\theta/dt = (V\theta/L)\ln(V\theta/L) \quad \text{(slip law)}$$

- Formulated based on lab experiments
- Direct effect can be derived from a model of viscoelastic creep
- Capable of representing stable and unstable sliding
  - Potentially, unstable sliding when $a < b$
  - Stable sliding when $a > b$

5 Anti-plane test problem to compare SEM and BIM

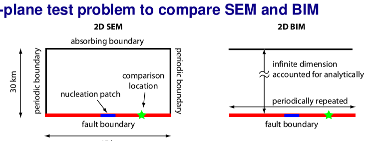

Our comparisons are similar to the SCEC code validation (*Harris et al.*, 2004), and we consider the following questions:

- the accuracy of SEM solutions with respect to BIM
- appropriate measures of errors
- abrupt vs. smooth initial conditions
- the state-variable updates, integration or direct use of evolution law
- simulations with aging law vs. slip law

6 SCEC 3D code comparison

A study of Day et al., 2005, similar to our comparison, is based on:

- linear slip-weakening friction
- non-smooth initial conditions (both in time and space)
- the errors are represented as rupture arrival time (slip rates at 1 mm/sec)

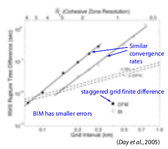

7 Initial conditions for our test cases

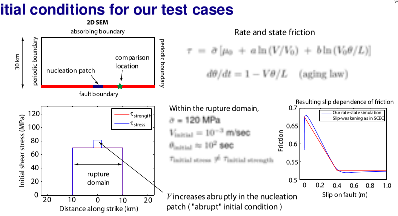

To have similar effective slip weakening of friction at the comparison location, we choose $a = 0.013$, $b = 0.018$, and $L = 0.038$ m. Hence, our initial conditions are similar to the initial conditions of the SCEC comparison problem.

8 2D SEM simulations using rate-state (aging law) friction

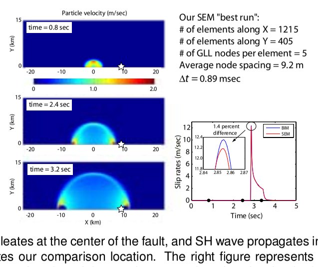

The rupture nucleates at the center of the fault, and SH wave propagates in the medium. The star indicates our comparison location. The right figure represents the SEM and BIM slip rates as a function of time at the comparison location for the best-resolution runs.

9 Measures of errors: rupture arrival time vs. cross-correlation

Two different measures of errors

1. Rupture arrival time difference
   Rupture arrival time ≡ time at a peak of slip rates (our current definition)
2. Cross-correlation time difference

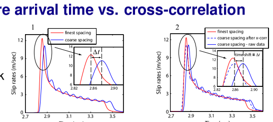

10 Convergence rates: rupture arrival time vs. cross-correlation

On the vertical axis, the rupture arrival time difference or the cross-correlation time difference between the highest-resolution run and lower-resolution runs is shown. In general, BIM and SEM give similar convergence rates in terms of the rupture arrival time difference. When the cross-correlation time difference is used, SEM shows smaller errors than those of BIM. For one of such cases, the slip rates for both BIM and SEM are shown on the bottom panels.

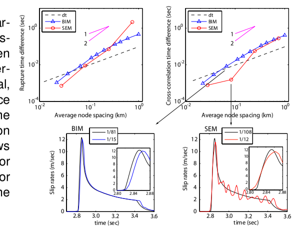

11 Geometry of 3D simulation

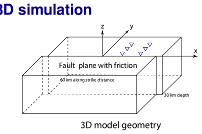

12 Nucleation and super-shear transition of spontaneous rupture

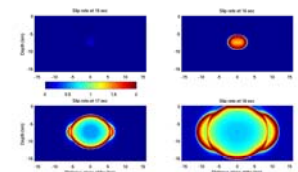

We have incorporated rate and state friction into 3D SEM dynamic rupture code (*Ampuero*, 2004). The snapshots of the slip rates on the fault are shown above. The initial conditions used for this simulation are similar to the smooth case in 2D, where the nucleation proceeds gradually. The rupture speed transitions from sub-shear to super-shear in the in-plane direction, consistently with daughter crack mechanism of Burridge-Andrews for slip weakening friction (Andrews, 1976). Note that the transition is observed here for rate and state friction laws.

13 Dynamic rupture simulation in homogeneous media

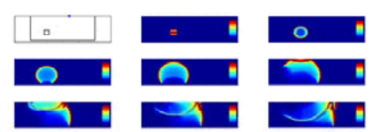

14 Dynamic rupture simulation in homogeneous media (continued)

Snapshots of horizontal slip rate (m/s) on the fault in the interval of one second. Homogeneous property (Vs = 3464 m/s, Vp = 6000 m/s) is imposed. The quantity $(a-b) = -0.005$ in the vel-weakening region, 0.005 in the vel-strengthening region. Effective normal stress is 120 MPa, and initial shear stress is 70 MPa except at "nucleation region" (81.6 MPa). The rupture speed becomes super-shear near the free surface.

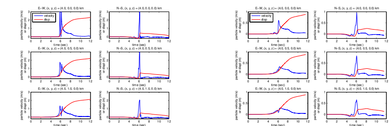

Displacement and velocity seismograms at 4-km horizontal distance (14 km away from the center of nucleation). Right and left insets correspond to the simulations above and below respectively. The top, middle, and bottom panels correspond to different off-fault locations (on the fault, 0.5 km away, and 1.0 km away from the fault).

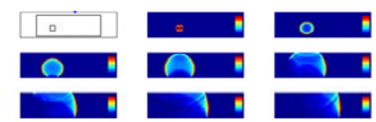

Same as above except that the effective normal stress gradually increases with depth and constant (120 MPa) below 6-km depth. The transition from velocity-weakening to velocity-strengthening is smooth and occurred at 2-km depth.

15 Dynamic rupture simulation in a layered structure

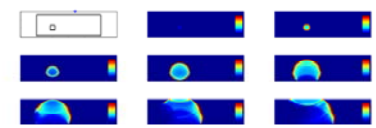

Snapshots of horizontal slip rate (m/sec) on the fault are shown in the interval of one second. Layered velocity model is used (Vs = 2136 m/s and Vp = 3700 m/s for 0 - 4 km depth, Vs = 2887 m/s and Vp = 5000 m/s for 4 km - 10 km depth, Vs = 3464 m/s Vp = 6000 m/s for 10-30 km depth).

16 Conclusions

- We have incorporated rate and state friction into 2D and 3D SEM dynamic rupture code for simulating a single earthquake.
- SEM and BIM give virtually indistinguishable solutions to the test problem with the nucleation and spontaneous rupture propagation when the node spacing is small enough.

17 Future work

- Understand how much can be learned from the near-field seismic records in terms of the history of slip or slip rate on the fault with different weakening mechanisms.
- Develop SEM to include variable time steps to simulate long-term deformation history of a fault.

Sense of shear and thermal evolution of the schist of Sierra de Salinas, California

Steven Kidder[1], Jason Saleeby[1], Frédéric Herman[1], Mihai Ducea[2]
[1] California Institute of Technology [2]University of Arizona

Abstract

Improved knowledge of kinematic and geochronologic relationships is important for understanding the late Cretaceous demise of the Salinia-Mojave continental arc, its effect on crustal composition, and the processes of sediment subduction, tectonic erosion, ridge collision and exhumation. The demise of the arc coincided with structural juxtaposition of forearc-type assemblages (the POR schists) and Eastern-zone plutonic rocks along the Salinas shear zone. We investigate this late Cretaceous episode using microstructural techniques, 2D modeling and Ar-Ar dating. Preliminary microstructural work indicates top-to-northeast ductile shear, similar to the sense of shear in lower-grade early Tertiary schists to the SE. Preliminary 2D modeling suggests that flat subduction may not be a feasible mechanism for schist emplacement as has previously been suggested.

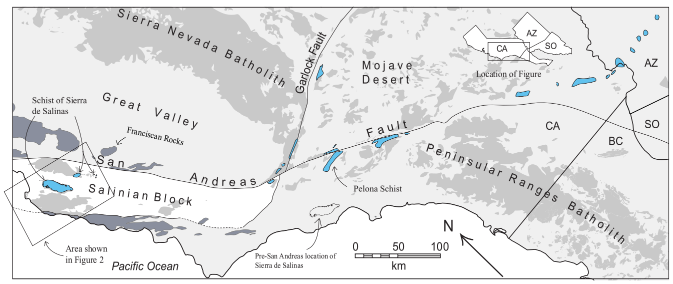

Figure 1. Map of parts of California, Arizona, Sonora, and Baja California showing some geologic features. The POR schists are shown in blue. Mesozoic granitic and related metamorphic rocks are shaded lightly. Fine-gridded areas are mainly Franciscan formation. Pre-San Andreas location of Sierra de Salinas from Powell (1993).

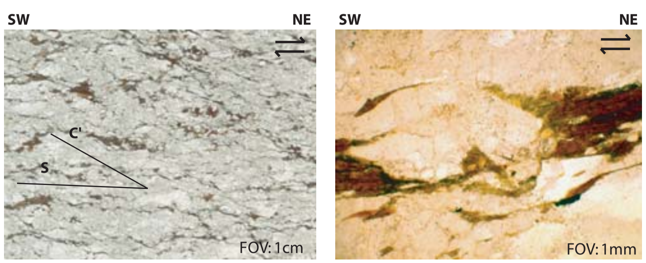

Figure 2. Micrographs of schist of Sierra de Salinas showing criteria used to determine sense of shear. The image at left shows typical C' fabric. The image at right shows two biotite "fish."

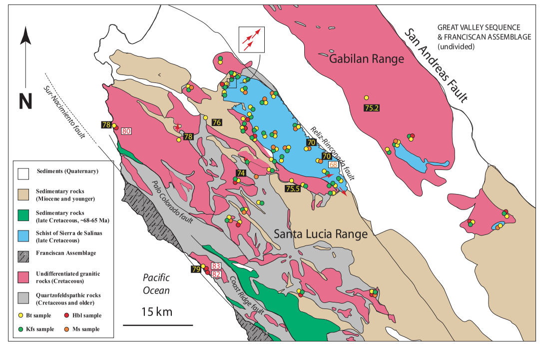

Figure 3. Geologic map of the Salinian central block (after Barbeau et al, 2005) showing sample locations for 40Ar/39Ar dating and sense-of-shear determinations. Boxed ages mark locations of samples previously dated by Barth et al. (2003) and Kistler and Champion (2001). Ar-work is in progress. See figure 1 for location. Red arrows indicate locations where a preliminary sense of shear is determined. Arrows indicate motion direction of upper plate.

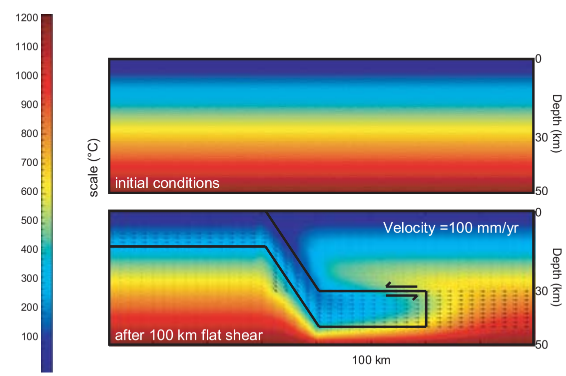

Figure 4. Thermal mechanical modeling can test the flat slab hypothesis (from East or West; e.g. Kidder et al, 2005; Grove et al, 2005). The key field observation is a convergence in upper and lower plate temperatures at initial upper plate conditions. Preliminary results shown above suggest insufficient heat is available with a flat slab scenario to reach observed temperatures in the schist.

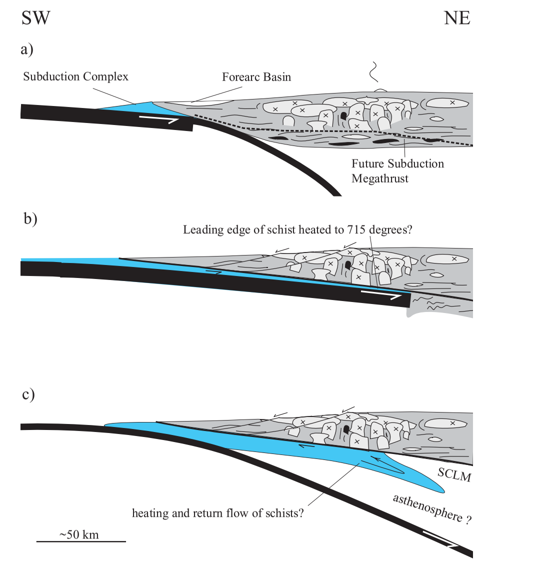

Figure 5. Cartoons depicting initial conditions and two possible scenarios for schist emplacement during the Late Cretaceous demise of the Salinia-Mojave continental arc. Schist shown in blue. No vertical exaggeration. (a) Initial conditions of arc just prior to collision with overthickened oceanic crust (e.g. Saleeby, 2003). The dashed line in panel a depicts the future location of the megathrust. (b) Flat slab hypothesis for heating the schist (after Kidder & Ducea, 2006). As lower portions of the arc were sheared off, the leading edge of the schist was carried beneath the now-extinct volcanic arc heating the schist to over 700º. This hypothesis predicts top-to-southwest shear. (c) Alternative hypothesis for heating the schist (after Saleeby, 2003). Schist is heated at depth and returned to shallower levels by some exhumation process, possibly return flow. This process overprints structures that may have developed in an earlier deformation phase of top-to-southwest shear (e.g. panel b). This hypothesis is more consistent with results of 2D modeling and preliminary evidence of top-to-northeast sense of shear observed in the schist of Sierra de Salinas.

Receiver Function Analysis of the Middle American Subduction Zone in Central Mexico

YoungHee Kim, Robert W. Clayton

Seismological Laboratory, California Institute of Technology, Pasadena, CA 91125

ABSTRACT

We have produced an image of the subducted Cocos plate beneath central Mexico with receiver functions utilizing data from the Meso America Subduction Experiment (MASE). The receiver function image shows that the subducting oceanic crust is shallowly dipping to the north at 15 degrees for 80 km from Acapulco and then horizontally underplates the continental crust for 200 km, all the way to the beginning of the Trans Mexico Volcanic Belt (TMVB). Both the continental and oceanic Moho are also clearly seen in the image. The cross section from Acapulco to a point 150 km to the north shows the erosion of the continental material by the slab. There is no apparent evidence of crustal compressional features due to the underplating. Beneath the TMVB, the slab is dipping at about 20 degrees toward the end of the MASE array (near the Atlantic Coast). The continental Moho is about 40 km deep beneath the TMVB and shallows towards the north. An image is also produced by migration of the individual receiver functions. Multiples are also included in the image because in many instances they are stronger than the primary conversions. The image is tested by modeling the derived structure with a finite-difference wave propagation program.

DATA

Station Map

Event Map

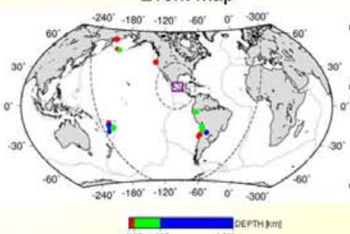

- 100 broadband stations
  - Interstation distance of 6±2 km
- 19 teleseismic earthquakes
  - 6 events from SE direction
  - 7 events from SW direction
  - 6 events from NW direction
- Magnitude range from 6.2 to 7.9

METHOD

I. Receiver Function Method

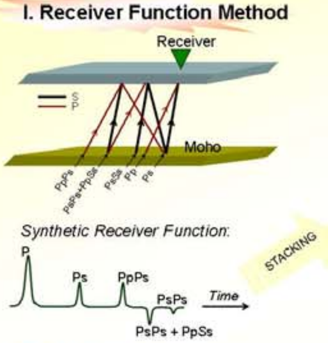

H (moho depth) and κ (v_p/v_s) are estimated by maximizing the weighted summation function: $S(H, \kappa)=w_1 r(t_{Ps})+w_2 r(t_{PpPs})-w_3 r(t_{PsPs})$.

The arrival times for Ps, PpPs, and PsPs are calculated for given (H, κ), and their amplitudes are phase-weighted summed.

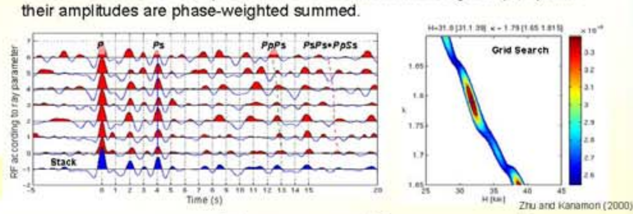

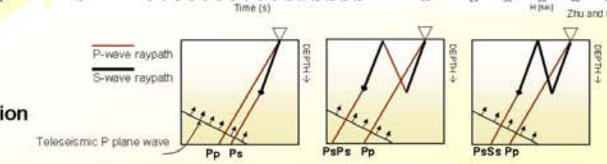

II. Receiver Function Migration

RESULTS

I. Receiver Function Method

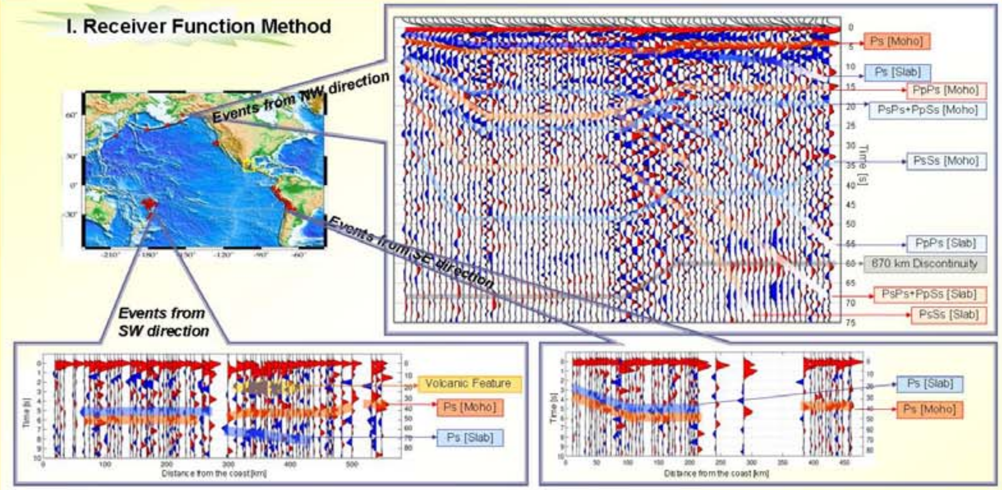

II. Receiver Function Migration

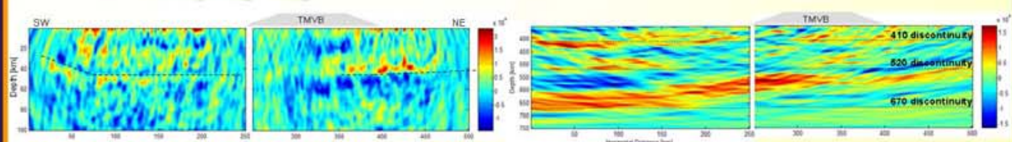

CONCLUSIONS & FUTURE WORK

Conclusions

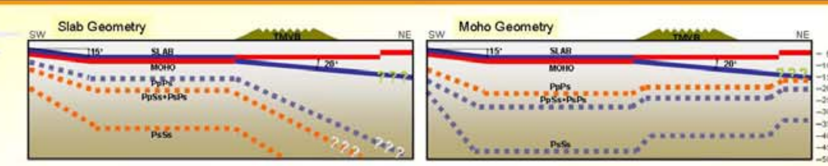

Future Work

- Focus on obtaining the slab geometry at the northern end of the MASE line using more data from future events
- To provide reference velocity from inversion
- To develop migration algorithm to deliver an inversion of scattered wavefield for variations in the Earth's elastic properties
- 2D & 3D elastic-wave finite-difference modeling
- To image upper mantle discontinuities by RF migration

The Rupture Characteristics of the 1999 Izmit Earthquake Sequence Using Geodetic and Seismic Data

A. Ozgun Konca[1], Don Helmberger[1], Sebastien Leprince[1], Jean-Philippe Avouac[1]
[1]Tectonic Observatory, California Institute of Technology e-mail: ozgun@gps.caltech.edu

Introduction

[The 1999 M_W7.5 Izmit and M_W7.1 Duzce earthquakes provide unique opportunities to study source caharacteristics using multiple datasets including teleseismic and strong-motion, SPOT GPS and field measurements. This study focuses on using various combinations of datasets to understand the kinematics of these earthquakes. The proximity of these events are also very useful since they can be used for path calibrations of teleseismic body waves.

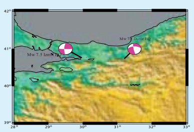

Figure 1: Local network (Kandilli) locations and Harvard CMT solutions of the events used in this study

1. Path Calibration for teleseismic inversions

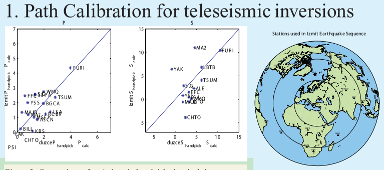

Figure 2: Comparison of variations in handpicked arrival times from the arrival times calculated with IASP 90 model.

The conventional method of doing source inversion involves "handpicking" of the arrival times of P and SH waves. The variations of handpicked arrival times from a reference one dimensional model are interpreted as a consequence of velocity variations. If that is the case, then two close events are predicted to have the same path corrections.

The Duzce and Izmit earthquakes are close enough, that their teleseismic arrival times would be similar relative to a 1-D reference model. However, as can be seen in Figure 2, the variations of handpicked arrival times from IASP 90 model, differ significantly despite the proximity of the two events. Especially, the incompatibility of the SH wave arrival picks is significant. In most stations, Izmit SH handpicks are earlier compared to Duzce picks.

Especially for S waves, the process of picking arrival times turns out to be harder for large events because of the presence of PS-coda arriving on top of the initial S onset. Since S waves have a slower apparent velocity, they are more sensitive to the rupture details. Hence picking their right arrival times is of critical importance.

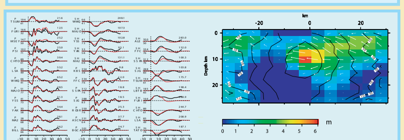

Figure 3, 4: Waveform fits and spatial distribution of slip for Nov 12, 1999, Mw7.2 Duzce Event using the inversion method by Ji, *et al*, 2002. Note that the slip is concentrated around the hypocenter.

We used the KOERI (Turkey) location for inversion. A single plane dipping 54º, from InSAR and GPS studies of Burgmann, et al, 2002 was used for the source inversion.

Inversion was done in two steps. First we perform an inversion with only handpicked P waves to get a preliminary distributed slip. We use this preliminary model to forward calculate synthetic seismograms and cross-correlate them with all the records that will be used in inversion. The time shifts obtained in this process are used to perform a second inversion with both P and SH waveforms.

Our inversion fits the teleseismic body waves very well. This inversion is also consistent with the result of joint InSAR and GPS inversion of Burgmann, et al, 2002.

Results for 17 Aug, 1999, Izmit Earthquake

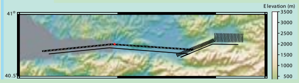

Figure 6: Izmit Earthquake is modelled with four segments based on the surface rupture observations (Delouis *et al*, 2002).
The dip of each segment is modified from a model by Wright *et al*;,2001, based on inversion of InSAR data for six segments.
A one dimensional velocity model for Western Turkey is used from Sekiguchi *et al*, 2002.

Figure 7: Waveform fits, Rupture Pattern , Static Field and GPS predictions for the inversion with the Calibrated Arrival Times

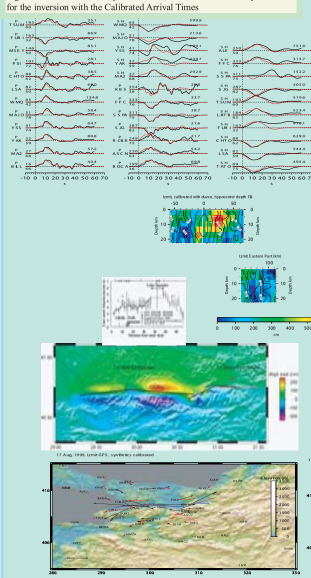

Figure 8: Waveform fits, Rupture Pattern, Static Field and GPS predictions for the inversion with the Handpicked Arrival Times.

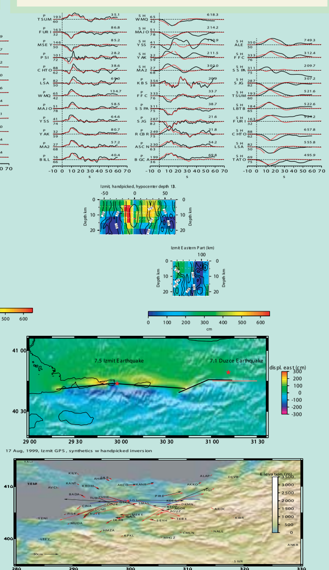

Results

Using calibrated arrival times reduces the overall waveform mismatch of the teleseismic data (~0.20 vs. 0.25).

The slip distribution for the two inversions differ considerably. For the calibrated inversion, the maximum displacement is to the east of the hypocenter, while it is west in the handpicked inversion. The asperity to the west is deeper in calibrated inversion. This effect is clearly revcealed in the estimated static field plots.

The SPOT data is more consistent with the calibrated arrival time inversion. The maximum slip in east-west direction is on the eastern end of Lake Sapanca as it is revealed in spot data.

The GPS predicted from handpicked inversion fits the data better than calibrated inversion. Relatively poor fit of the calibrated inversion is due to north south component of the slip. The reason for this could be the complexities of the fault geometry as well as the slip distribution. However, understanding the actual reason for this inconsistency (fitting SPOT data better, but fitting GPS poorer) remains as a future work for us.

2. Joint Inversion of Duzce Earthquake

Similar to Izmit Earthquake, supershear rupture velocity (~4.5 km/s) to the east is estimated from strong-motion data for Duzce earthquake while rupture to the west is about 3 km/s. Here we test two scenarios **(a)** fast rupture speed (3.8-4.8 km/s) to the east and slow (2.5-3.5km/s) to the west (b) slow rupture speed (2.5-3.5km/s) to the east to the east and slow (3.8-4.8 km/s) to the west. The goal of this comparison is to test whether teleseismic data together with near-field geodesy has any significant sensitivity to rupture velocity or not.

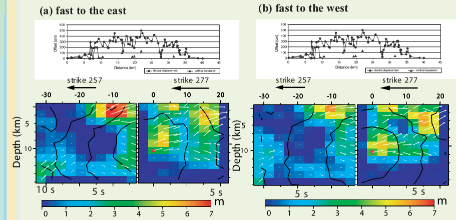

Figure 9: Slip model for joint (teleseismic, GPS and InSAR inversion of Duzce earthquake. Rise time is between 1-5 s.

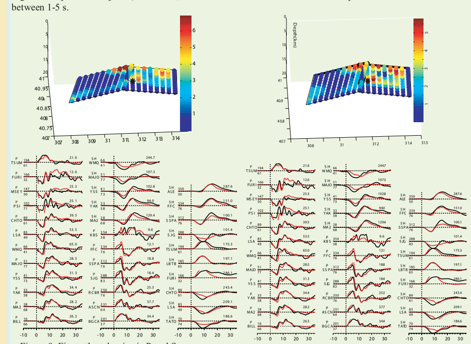

Figure 9: Fits to the teleseismic P and S waves

M_W7.1 Duzce earthquake is a significant earthquake to study.
There is a wealth of teleseismic, strong-motion, geodetic and geological data available. There has not been a study yet that used all available data. The goal here is to use all data available. The results shown here are shown here do not include the strong-motion data yet. The model shown in Figure 9 is quite consistent with geodetic inversion (Burgmann et al, 2002), and GPS and strong-motion inverson (Bouin et al., 2004).
Another target of this study is to understand whether supershear rupture speed proposed to explain strong-motion data is consistent with other datasets. The geodetic data and surface offset measurements constrain the slip distribution significantly. Therefore, the rise time and rupture velocity are the two parameters to play with, in order to fit both teleseismic and strong-motion data.

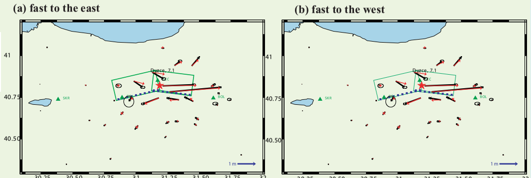

Figure 11:Fits to GPS data. Data is in black and synthetics are in red. Strong-motion stations that are going to be used are shown with green triangles.

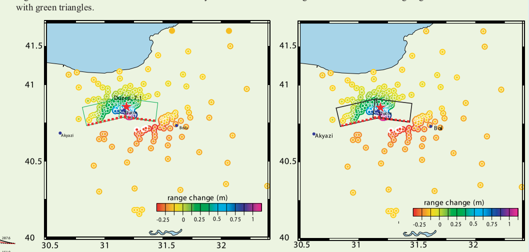

Figure 12:Fits to InSAR data. Each circle is a datapoint, where the smaller circle inside is the synthetic and outer circle is the data. Two fault planes are also shown.

These results show that the combination of far field seismic data and near-field geodetic data is not sufficient to resolve the details of the rupture velocity. The misfits to the datasets for the two scenarios are similar.

Summary and Future Work

This study aims to study Izmit and Duzce earthquakes using consistent travel times for both events and all available datasets to resolve the details of rupture velocity and slip distribution. As a start, we have used the calibration of travel times to see what difference it makes in teleseismic inversions. We have also modeled Duzce earthquake using geodetic ad teleseismic data. We will also implement strong-motion and surface offsets using SPOT images in future. It is of great interest to model strong-motion data together with geodetic data to test whether the observed waveforms are due to a supershear rupture or not.

Once good slip distributions are achieved for these two events, we can learn about the interactions and how stress change of Izmit earthquake has effected the Duzce earthquake.

Moreover, we can use these calibration events to reexamine historical events of the 20th century using existing teleseismic recordings by methods similar to previous studies of the 1906 San Francisco earthquake

Time Dependent Slip:

A Mathematical Study of Historic Displacement Near the Sunda Megathrust Subduction Zone

A. P. Kositsky, M. Chlieh, J-P. Avouac, K. Sieh - California Institute of Technology, GPS division D. H. Natawidjaja,- LIPI, Indonesia
apk@caltech.edu

ABSTRACT
We invert displacement data using principal component analysis (PCA) and the Okada formulation for slip at depth on the fault in the Sumatra subduction zone. Though this work only deals with one dimensional displacement data, the method can be generalized to three dimensional displacements using GPS data. (Work in progress)

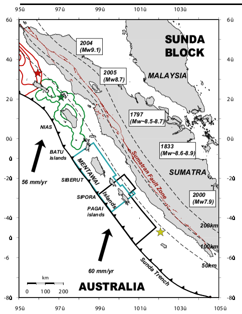

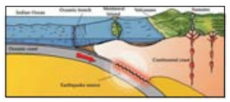

Located in Southeast Asia, the Sunda subduction zone lies at the interface between the Sunda block and the Australian plate.

Over the last 200 years, there have been at least five giant earthquakes, including the December 26, 2004 earthquake which caused a tsunami that killed approximately 100,000 people. As such, a detailed understanding how the two plates are slipping past each other can help us understand where and when the next giant earthquake near the Sunda subduction zone is likely to occur.

The earthquake cycle for two plates on the seductions on consists primarily of three phases:

1. Inter-seismic Loading
   - As the subducting plate and the overriding plate converge, a section of the interface between the two plates locks and stress builds over time.
2. Co-seismic Events
   - The stress eventually becomes too much for the plates to bear a sudden and violent slipping between the two plates (i.e. an earthquake) occurs, releasing the stress that has built up.
3. Post-seismic Relaxation
   - After the earthquake the plates gradually return to a temporary state of equilibrium, often accompanied by gradually decreasing time-dependent slip.

A cartoon representation of this process and the resulting surface deformation are located in the figure on the right. This information implies that if we are able to figure out what the displacement at the surface has been we may be able to solve for what is happening at depth.

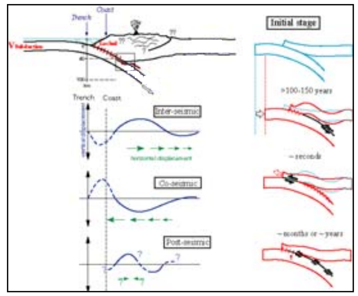

Photos courtesy of the Tectonics Observatory.

(Left)
The two primary methods used to measure surface displacement at this particular site are GPS, which directly measures displacement in every direction, and coral growth records, which is a proxy for vertical displacement. While GPS both is more precise and provides data in three directions rather than just one, we can only find data for time periods during which a GPS station was functioning and in place. Coral dies when it is exposed to air. Thus any changes in the lowest low tide of the year, for example due to tectonic uplift, may be reflected in how the coral grows from year-to-year. Because coral occurs naturally, coral growth records can provide over a hundred years of displacement data [5].

(Right)
After taking into account factors such as changes in sea level over time and idiosyncrasies related to working with a biological proxy, the position of the yearly growth rings formed by coral can be counted to determine the sea level relative to some part of the coral that can be dated using radioactive isotopes. What results are time series that provide a reasonably detailed record of vertical deformation over the last 40 to 150 years.

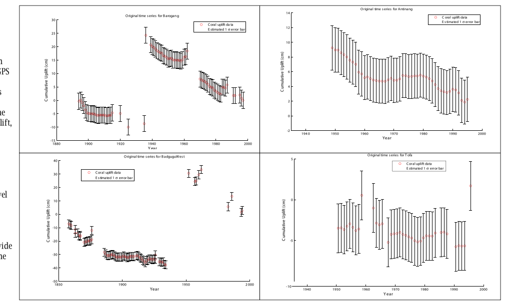

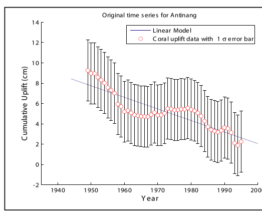

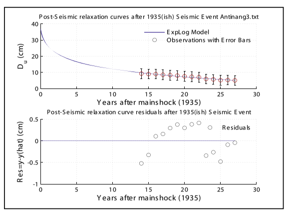

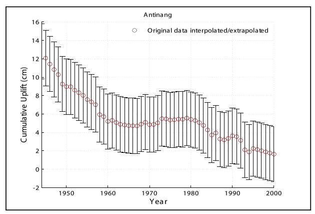

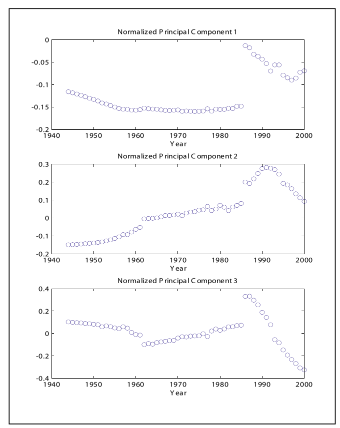

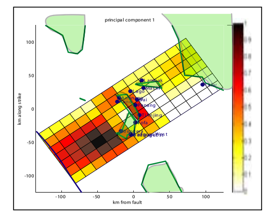

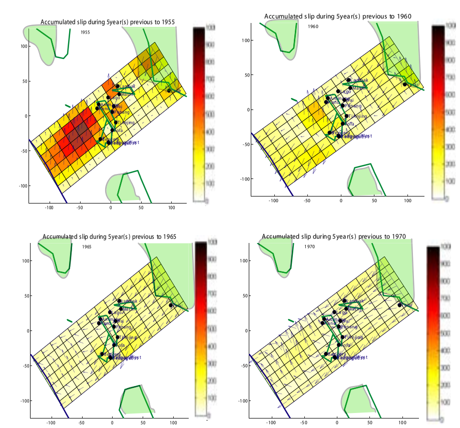

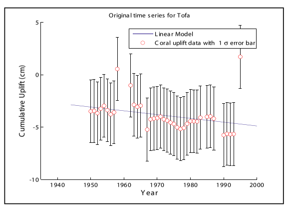

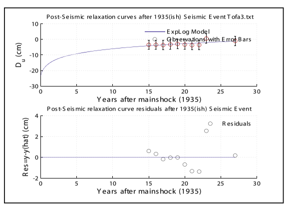

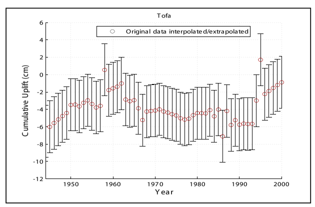

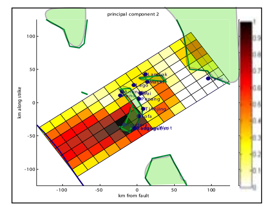

The most straightforward model is one that is linear with time. That is, the rate of displacement (vertical displacement in this case) at the surface is constant. This allows us to explain most of the first-order features of the data (no pun intended.) However, it is clear that there is some unexplained variability in the data.

The first step in investigating this variability is to fit the data using an assumed physical model, in this case the spring slider model from [8].

The physical model allows us to interpolate and extrapolated data so each of our datasets has the same distribution of "measurements" in time. In the case of the coral data, we make this an even distribution with one data point per year.

We then decompose all of our time series using a statistical technique called principal component analysis (PCA). The so-called principal component vectors are chosen and ordered such that the first principal component vector explains as much variability of the data as possible, the second principal component vector explains as much variability of the data as possible given that the variability associated with the first component has been removed, and so on. This allows us to find the common patterns amongst the data (in other words, components not consisting of uncorrelated noise or signal,) and thus faithfully represent each time series as the sum of the first several pence will components. In this particular case, there are 14 principal component vectors total and the even the most troublesome stations (e.g. Antinang) are well-represented with the first six principal components. Some stations (e.g. Barogang) are well-represented with only one component.

Each of the principal components has a weight corresponding to each station. These weights represent how strongly each principal component is represented in the time series of that particular station. The vertical displacement resulting from the contribution of each component is proportional to each component's weight for that station. Using this information or a given component we are able to invert the set of weights for each station using the Okada formulation and solve for a slip map that xplains the surface deformation we observe that the surface due to this component. In part the quality of the smoothing parameter used. If the smoothing parameter is set too low, the slip distribution will not be able to vary much with position. However if the smoothing parameter is set too high, the solution becomes very non-unique.

The figures above are examples of cumulative slip distributions over five-year periods, from 1950-1955, 1956-1960, 1961-1965, and 1966-1970. Notice how the direction and magnitude of slip over these time periods varies greatly. From examining all of the time series, it is clear that something out of the ordinary happened near 1960. Figures such as these will help unravel the mystery. Units are relative.

References:

[1] Aoki, Y., and C. H. Scholz, Vertical deformation of the Japanese islands, 1996 - 1999, J. Geophys. Res., 108(B5), 2257, doi:10.1029/2002JB002129, 2003.
[2] Hsu, Ya-Ju, et. al., 2006. Frictional afterslip following the Mw 8.7, 2005 Nias earthquake, Sumatra, prepared.
[3] Marone, C. (1998), Laboratory-derived friction laws and their application to seismic faulting, Annu. Rev. Eath Planet. Sci., 26, 643-696.
[4] McGuire, Jerey J. and Segall, Paul, 2003. Imaging of aseismic fault slip transients recorded by dense geodetic networks, Geophys. J. Int. 155:3 778.
[5] Natawidjaja, D. H., K. Sieh, S. N. Ward, H. Cheng, R. L. Edwards, J. Galetzka, and B. W. Suwargadi, 2004. Paleogeodetic records of seismic and aseismic subduction from central Sumatran microatolls, Indonesia, J. Geophys. Res., 109, B04306, doi:10.1029/2003JB002398.
[6] Okada, Ya, 1992, Internal deformation due to shear and tensile faults in a half-space: Bulletin Of the Seismological Society Of America, v. 82, no. 2, p. 1018-1040.
[7] Perfettini, H., and J.-P. Avouac, 2004, Postseismic relaxation driven by brittle creep: A possible mechanism to reconcile geodetic measurements and the decay rate of aftershocks, application to the Chi-Chi earthquake, Taiwan, J. Geophys. Res., 109, B02304, doi:10.1029/2003JB002488.
[8] Perfettini, H., J.-P. Avouac, and J.-C. Ruegg, 2005, Geodetic displacements and aftershocks following the 2001 Mw = 8.4 Peru earthquake: Implications for the mechanics of the earthquake cycle along subduction zones, J. Geophys. Res., 110, B09404, doi:10.1029/2004JB003522.
[9] Savage, J.C., and J.L. Svarc, 1997. Postseismic deformation associated with the 1992 Mw=7.3 Landers earthquake, Southern California, J. Geophys. Res., 102, 7565-7577.
[10] Segall, Paul and Matthews, Mark, 1997. Time dependent inversion of geodetic data, J. geophys. Res., 102, 22 391-22 400.
bibitem Crustal Deformation Associated with Two-Dimensional Thrust Faulting Sarva Jit Singh* and Sunita Rani Department of Mathematics, Maharshi Dayanand University, Rohtak- 124001, India.

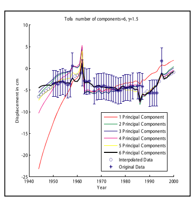

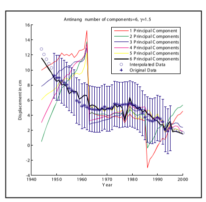

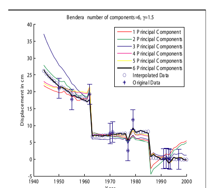

Special thanks to the SURF program, the Tectonics Observatory, and the George W. Housner Student Discovery Fund for supporting this project.

An example of the how well the slip model agrees with the field data.

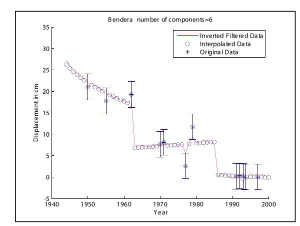

COSI-Corr v1.0 : Co-registration of Optically Sensed Images and Correlation

Toward an operational use of optical remotely sensed images for ground deformation measurements

S. Leprince, F. Ayoub, J-P. Avouac - California Institute of Technology, GPS departement
leprincs@caltech.edu

Y. Klinger - IPGP, France

In complement to seismological records, the knowledge of the ruptured fault geometry and of the co-seismic ground deformation are key data to investigate the mechanics of seismic rupture. This information can be retrieved from sub-pixel correlation of pre- and post-earthquake remotely sensed optical images. However, this technique suffers from a number of limitations, mostly due to uncertainties on the imaging systems and on the platform attitudes, leading to strong distortions and stereoscopic effects. Here, we propose an automated procedure that overcomes most of these limitations. In particular, we take advantage of the availability of accurate digital elevation models with global coverage (SRTM). This methodology will improve our ability to collect measurements of ground deformation, in particular in the case of large earthquakes occurring in areas with little or no local geophysical infrastructure.

Measuring co-seismic deformations from remotely sensed optical images is attractive thanks to the operational status of a number of imaging programs (SPOT, ASTER, USGS-NAPP aerial programs, etc...) and to the broad availability of archived data.

The general procedure consists of generating accurate ground control points (GCP) for each image. An accurate ortho-rectification model is then built, which allows accurate ortho-rectification and co-registration of the images. Correlation on the ortho-rectified images then delivers the horizontal ground displacements to analyse.

As of November 2006, we are releasing a complete software package, COSI-Corr, developped in IDL and integrated under ENVI, that allows for such processing. In the following, we demonstrate its main capabilities, namely the processing of SPOT, ASTER and aerial images, the possibility of constraining aerial images with satellite derived measurements, and the convenient use of batch processing for intensive computations.

The 2005, Mw 7.6 Kashmir earthquake: Sub-pixel correlation of ASTER images

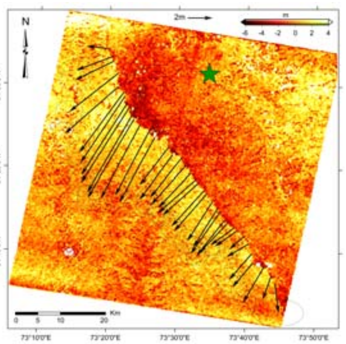

The color image represents the Northward ground displacements (positive to the north), determined from the correlation of ASTER images, 15-m ground resolution, taken on November 14, 2000 (AST_L1A.003:2003527667) and on October 27, 2005 (AST_L1A.003:2031572195). The incidence angle is 8.6° for both images. This correlation image was obtained with a sliding 32×32 pixels correlation window and 8-pixel step, leading to a ground resolution of 120 m. No measurement is assigned to white points, where the correlation is lost or where outliers (where the measured ground displacement was found to exceed 10 m) have been filtered out. Correlation is lost mainly due to landslides or variation of the snow cover.
Oscillations with an amplitude of 3-4m and with a period of 5km have been removed from stacking. They were characteristic of attitude oscillations from ASTER.

Arrows represent the horizontal surface fault slip. They are determined from linear least sqaure adjustment, on each side of the fault and on each NS and EW images, of stacked profiles running perpendicularly to the rupture. Profiles are stacked over a width of 6 km and a length of 18 km. Ellipses show the 95% confidence intervals.

The 1999, Mw 7.1 Hector Mine earthquake: Using a priori information from Satellite images to better constrain Aerial images measurements

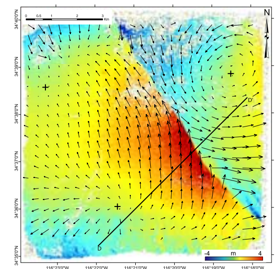

NS component of the correlation map. Three GCPs, located by the black crosses, are optimized to co-register the images without accounting for seismic ground displacement at their ground location. Arrows represent the ground displacement field accounting for both NS and EW components. Long wavelength distortions are introduced to satisfy the images co-registration.

Aerial Pre-earthquake image
USGS-NAPP, 7/25/89, 1m

Aerial Post-earthquake image
USGS-NAPP, 06/01/02, 1m

Aerial Processing
- 128m x 128m correlation windows
- 16m between measurments

Satellite Pre-earthquake image
SPOT 4, 10m, 08-17-1998

Satellite Post-earthquake image
SPOT 2, 10m, 08-18-2000

Satellite Processing
- 320m x 320m correlation windows
- 80m between measurements

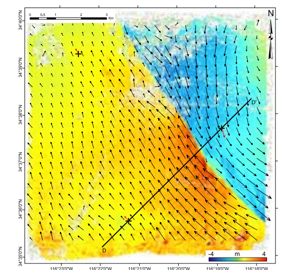

NS component of the correlation map. The GCPs are optimized to co-register the images while accounting for ground displacement at their ground location (red arrow) from SPOT derived measures. Major long wavelength distortions are removed. Only may remain the long wavelength distortions caused by the SPOT correlation error, along with those introduced by film distortions.

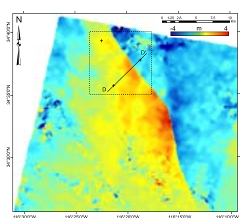

North/South component of the denoised SPOT correlation map. The GCPs are located away from the fault to assume a null ground displacement. Images are orthorectified on a 10 m resolution grid and correlated using a 32 × 32 pixels window with a 8 pixels step. The dotted square represents the air photo footprint, and black cross indicates the location of the air photo GCPs.

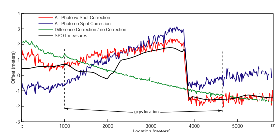

Profile DD'. GCPs correction brings a 2nd order polynomial correction in each NS and EW directions. High frequency signal (displacement at the fault) is not affected however.

The 1999, Mw 7.1 Hector Mine earthquake: Cross-correlating SPOT and ASTER images

COSI-Corr allows the co-registration and correlation of several kinds of data. Here is an example where the co-seismic displacement of the Hector Mine earthquake is accurately retrieved from the cross-correlation of SPOT and ASTER images. Here, only the NS compenent of the displacement is shown. The correlation map has been denoised.

Satellite Pre-earthquake image
SPOT 4, 10m, 08-17-1998

Satellite Post-earthquake image
ASTER, 15m, 04-24-2000

Processing
- Each image is ortho-rectified at 15m
- 480m x 480m correlation windows
- 120m between measurements
- Waves artifacts due to the pitch oscillations of ASTER have been removed by stacking

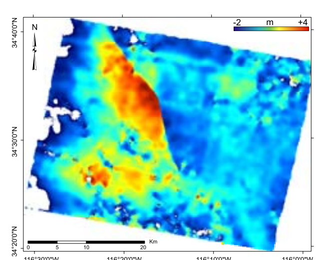

The 1992, Mw 7.3 Landers earthquake from Aerial images, batch processing. SPOT images taken as reference.

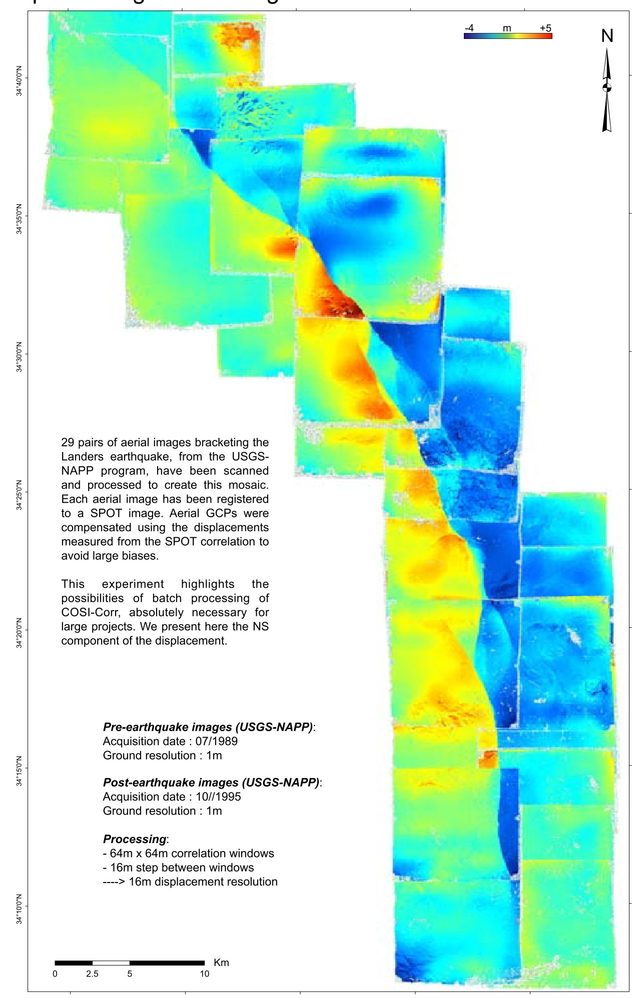

29 pairs of aerial images bracketing the Landers earthquake, from the USGS-NAPP program, have been scanned and processed to create this mosaic. Each aerial image has been registered to a SPOT image. Aerial GCPs were compensated using the displacements measured from the SPOT correlation to avoid large biases.

This experiment highlights the possibilities of batch processing of COSI-Corr, absolutely necessary for large projects. We present here the NS component of the displacement.

Pre-earthquake images (USGS-NAPP):
Acquisition date : 07/1989
Ground resolution : 1m

Post-earthquake images (USGS-NAPP):
Acquisition date : 10//1995
Ground resolution : 1m

Processing:
- 64m x 64m correlation windows
- 16m step between windows
----> 16m displacement resolution

Work in progress, collaboration with Yann Klinger, IPGP, France

References:

S. Leprince, S. Barbot, F. Ayoub and J. P. Avouac, "Automatic, Precise, Ortho-rectification and Coregistration for satellite Image Correlation, Application to Ground Deformation Measurements", IEEE Transactions on Geoscience and Remote Sensing, In Press 2006.

J. P. Avouac, F. Ayoub, S. Leprince, O. Konca and D. Helmberger, "The 2005, Mw 7.6 Kashmir earthquake, rupture kinematics from sub-pixel correlation of ASTER images and seismic waveforms analysis", Earth and Planetary Science Letters, vol. 249, no. 3-4, 2006, pp. 514-528.

F. Ayoub, S. Leprince and J.P. Avouac, "Aerial Photography for Seismic Ground Deformation Measurement",Submitted to ISPRS, 2006.

S. Leprince, A. Samanta and J.P. Avouac, "Edge Preserving Denoising of Optical Correlation Images, Applications to Ground Deformation Measurement", in preparation.

Three-Dimensional Elastodynamic Simulations of Seismic and Aseismic Slip History of a Planar Strike-Slip Fault

Yi Liu (yil@caltech.edu) and Nadia Lapusta (lapusta@caltech.edu), California Institute of Technology

Abstract

Simulations of spontaneous slip accumulation in three-dimensional (3D) models enjoy a lot of interest because of their ability to clarify earthquake physics. We have been developing a 3D methodology for simulating the entire seismic and aseismic slip history of a fault subjected to slow tectonic loading. The algorithm, extended from the 2D study by Lapusta et al. (2000), allows us to resolve all stages of spontaneous slip accumulation in a single computational procedure, including quasi-static nucleation process, dynamic rupture propagation, post-seismic deformation, and aseismic processes throughout the loading period. Simulating long-term deformation histories while accounting for dynamic effects of occasional earthquakes is quite challenging due to a variety of temporal and spatial scales.

We consider a vertical strike-slip fault embedded in an elastic half-space and governed by rate and state friction. On the fault, there is a seismogenic region, 30 km long and 15 km deep, with steady-state rate-weakening properties. It is surrounded by steady-state rate-strengthening regions that stably slip (creep) under loading. We observe the following interesting phenomena:

(1) The simulations produce realistic earthquakes and complicated patterns of interseismic slip. The earthquakes propagate with rupture speeds comparable to the shear wave speed of the surrounding bulk and have average slip rates of order of 1 m/s. After each large earthquake, there is an accelerated post-seismic creep in the surrounding rate-strengthening regions. During interseismic periods, we observe very interesting patterns of aseismic slip, with accelerating and decelerating patches and slow propagation of faster creep along the interface. These patterns result in occasional small events.

(2) The quasi-dynamic model, which ignores wave-mediated stress changes and hence significantly simplifies the computation of dynamic response, qualitatively captures most features of the fully dynamic computation, but produces more sluggish earthquake behavior and seems unable to reproduce some dynamic features such as the supershear burst.

(3) An asperity (a small circular region 20% stronger than the surrounding fault) causes a supershear burst for the first earthquake in the simulation but not for subsequent events. This indicates that single-earthquake simulations, due to their strong dependence on initial conditions, may in some cases reach conclusions that would not be sustained over a longer history of the fault.

(4) All simulated large events have similar initial stages of their moment-rate function.

In future studies, we plan to (i) adopt more realistic friction laws, by combining rate and state friction with pore pressure evolution and flash heating effects during the dynamic rupture; (ii) incorporate the bimaterial configuration into our earthquake sequence simulations, to investigate its statistical influence on rupture propagation direction over many earthquake cycles; (iii) determine the model response for a wider range of frictional parameters, such as more realistic characteristic slip distance of rate and state friction; (iv) investigate the possibility of determining frictional parameters by comparing our simulations with observations; (v) study whether complicated patterns of aseismic slip that we observe can explain recent observations of slow earthquakes and other interseismic phenomena.

Model of a vertical strike-slip fault

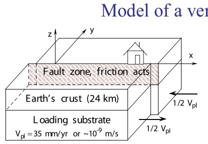

3D earthquake simulations help us to:

1. Study effects of earthquake physics and fault geometry, independently of initial conditions.
2. Understand how earthquakes nucleate, propagate and arrest, and how these stages interact.
3. Understand how heterogeneitites influence fault behavior in earthquake sequences vs. single earthquakes.

In simulations, we use rate-and-state friction law:

$$\tau = \sigma f = \sigma\left[f_o + a\ln\frac{V}{V_o} + b\ln\frac{V\theta}{L}\right] \qquad \frac{\partial\theta}{\partial t} = 1 - \frac{V\theta}{L}$$

a, b are friction parameters, of the order of 0.01.

If $a < b$, the fault exhibits steady-state velocity weakening;

if $a > b$, the fault exhibits steady-state velocity strengthening.

Basic friction f_o = 0.6 at the sliding velocity V_o = 10^{-6} m/s.

Main challenge in simulations of earthquake sequences: multiscale nature

Multiple scales in time (dynamic cracks + slowing loading)

Loading time	100 to 1000 years
Duration of dynamic event	10 to 100 seconds
Time for rapid change of variables at the crack tip	fraction of a second

Multiscale in space

Fault dimensions	100 km
Nucleation size on faults	1 to100 meters (if L ~ 10 to 100 μm)
Distance of rapid changes at the rupture tip	fraction of a meter

Case I: Fault with homogeneous seismogenic region

Model Geometry

We simulate earthquake sequences on a fault embedded in an infinite elastic half space, subjected to slow tectonic loading V_{pl} = 35 mm/yr. The fault properties are extended from 2D studies (i.e. Lapusta et al. 2000), where a steady state velocity-weakening region of a = 0.015 and b = 0.019 is surrounded by seatdy state velocity-strengthening regions of a = 0.019 and b = 0.015. Nucleation starts in the strip -15 km < x < -10 km as the initial shear stress there is set to be 10% higher than $\tau_{ss|V=V_{o}}$. L is 8 mm, and the estimated critical nucleation sizes for an in-plane problems are (Rice Ruina, 1983; Rubin and Ampuero, 2005):

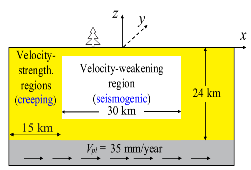

$$h^*_{RR} = \frac{\pi}{4}\frac{\mu}{1-\nu}\frac{L}{\sigma(b-a)} \approx 1.1 \text{ km} \qquad h^*_{RA} = \frac{1}{\pi}\frac{\mu}{1-\nu}\frac{Lb}{\sigma(b-a)^2} \approx 2.5 \text{ km}$$

The calculation is implemented using spectral boundary integral method. Since the analytical integral kernels are available only for the whole infinite space, we make a mirror image of the simulated fault to approximately represent the effect of the free surface.

We use variable time stepping. Throughout the computation, time steps change by more than 10 orders of magnitude, allowing us to do relatively few steps through the quasi-static slow-loading periods, and to consider carefully earthquake nucleation and dynamic rupture propagation periods.

Snapshots of slip rate distribution during 1st and 2nd events

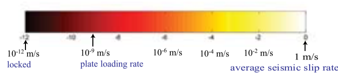

The color scheme depicts the slip rate in m/s on a logarithmic scale. Each snapshot has two time markers. The first one is simulated time t in years. The second one is the current time step Δt multiplied by 50.

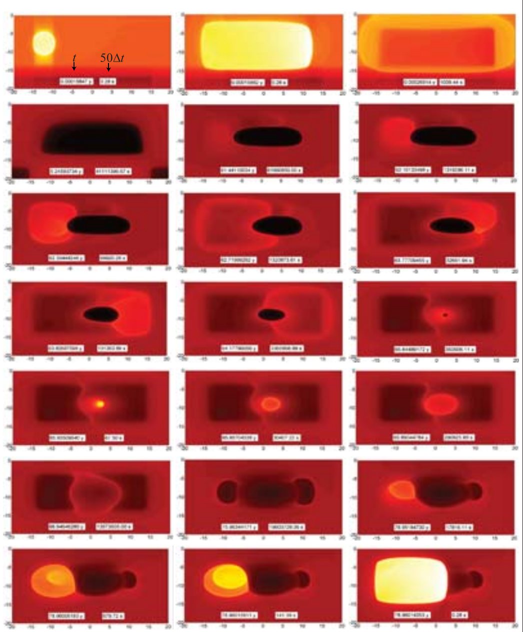

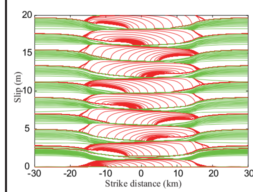

Fig 1: Accumulation of slip vs. strike, along the line z = -8 km. The red lines are plotted every 1 second when the maximum slip rate exceeds 1 mm/s. The green lines are plotted every 5 years.

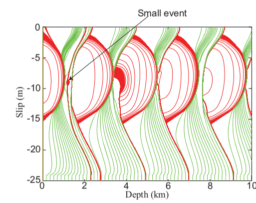

Fig 2: Accumulation of slip vs. depth, along the line x = 3 km. The red lines are plotted every 1 second when the maximum slip rate exceeds 1 mm/s. The green lines are plotted every 5 years.

Case II: Fault with a compact heterogeneity

We add a circular patch of 1 km radius, centered at the point (3 km, -8 km). The effective normal stress σ in the patch is 20% larger than on the rest of the fault. The other parameters are the same as in Case I. We find that the heterogeneity causes a supershear burst for the first earthquake but not for subsequent events.

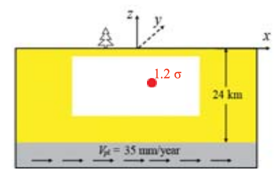

Supershear Burst in the First Event

Snapshots of velocity distribution in the 1st event:

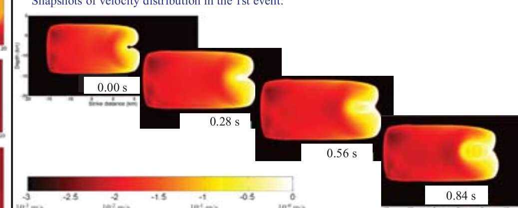

Average rupture speed during the time shown is c = 4.6 km/s which is larger than c_s = 3 km/s. Dunham et al. (2003) studied this kind of supershear bursts in single-event simulations; rupture surrounds the heterogeneity and creates a supershear burst after breaking it.

No Supershear Burst in the Following Events

Snapshots of velocity distribution in the 2nd event:

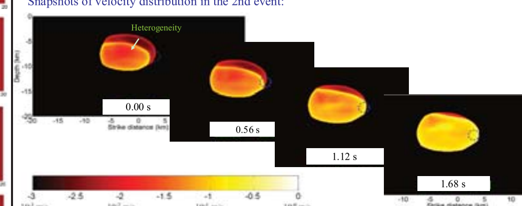

Supershear burst due to this heterogeneity is not repeatable in subsequent events due to redistribution of stress.

Comparison between fully-dynamic and quasi-dynamic models for Case II

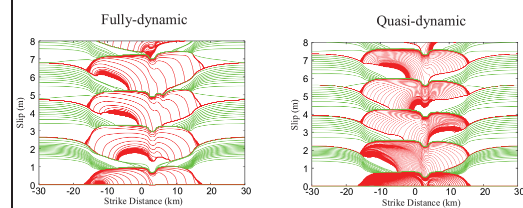

Fig 3: Accumulation of slip vs. strike, along the line z = -8 km that passes through the center of the heterogeneity. The red lines are plotted every 1 second when the maximum slip rate exceeds 1 mm/s. The green lines are plotted every 5 years.

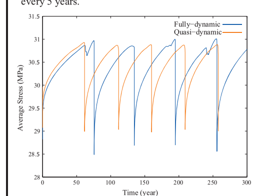

Fig 4: Comparison of average stress drop between fully-dynamic and quasi-dynamic models.

Quasi-dynamic simulation has some qualitatively similar features:
- slow nucleation process
- fast rupture propagation
- postseismic slip
- interseismic slip

Quasi-dynamic simulation has important differences with the fully-dynamic simulation:
- slower rupture propagation speed
- smaller slip rate and slip in events
- smaller earthquake period
- smaller stress drop in events

Similar moment rate function for large events

Moment rate $\dot{M}_o = \mu\iint V(x,z)\,dxdz$

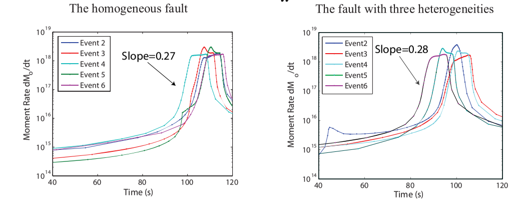

Different events have almost the same slope of growth S.
What is the physical meaning of the slope? Some discussion in Ampuero (2003).
Can it be inferred from seismic observation?

Influence of L on earthquake period T

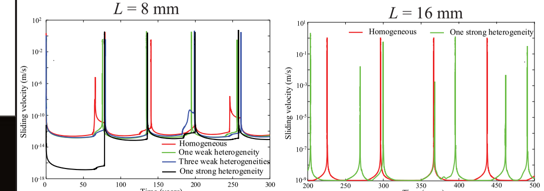

Fig 5: Sliding velocity evolution for several simulated cases with different heterogeneities on the fault. Every vertical line represents an event, and the time itervals between vertical lines are earthquake periods T. For L =16 mm, T is different for different cases. For L =8 mm, T is almost the same.

What happens for even smaller L?
Will T become insensitive to the existence of heterogeneities for small enough L?

An Instantaneous Sub-Rayleigh-to-Supershear Transition Mechanism

Yi Liu[1] and Nadia Lapusta[1,2]

1. Division of Engineering & Applied Science, Caltech, Pasadena, CA
2. Division of Geological & Planetary Sciences, Caltech, Pasadena, CA
E-mail: yil@caltech.edu, lapusta@caltech.edu

1 Abstract

Observations suggest that supershear bursts and sustained supershear propagation may have occurred in a number of earthquakes (such as 1992 Landers, 1999 Izmit, and 2001 Kunlun). Two mechanisms have been proposed to explain the sub-Rayleigh-to-supershear rupture transition. In the Burridge-Andrews mechanism (e.g., Andrews, 1976), the shear-wave stress peak traveling in front of the main Mode II rupture nucleates a daughter crack, if the prestress on the fault is large enough, and the daughter crack is born supershear. Alternatively, supershear burst can result from breaking a strong heterogeneity on a 3D fault as shown by Dunham et al. (2003).

Taking a broader look at the Burridge-Andrews mechanism, we hypothesize that, for the model to produce rupture transition from sub-Rayleigh to supershear speeds, it needs to accomplish two goals: (i) nucleate a crack and (ii) drive the crack fast enough. These processes are inseparable in the Burridge-Andrews mechanism, as they both occur at the shear stress peak of the main crack propagating in a uniform prestress field. Our simulations show that goals (i) and (ii) can be achieved in other ways. For example, one can advance Mode II rupture towards a location susceptible to crack nucleation, such as a preexisting subcritical crack, a patch of lower static friction strength, or a patch of higher prestress. In these cases and under the right conditions, the secondary crack nucleates before the shear stress peak arrives, and yet the stress field of the advancing main rupture is still able to drive the secondary crack to supershear speeds. Hence nucleating the daughter crack at the shear stress peak, as it is done in the Burridge-Andrews mechanism, is not essential for the subsequent supershear propagation. One can also use different means of driving the crack supershear, such as overstressing statically a part of the rupture or imposing an outside dynamic stress field.

We observe the following interesting features in our simulations, which we will present along with our preliminary analysis:

(1) Crack fronts can abruptly jump from the Rayleigh-wave speed to a supershear speed. We call this "direct" supershear transition. For example, consider a secondary crack nucleated by one of the ways described above under the advancing stress field of the main rupture. The secondary crack is sub-Rayleigh and it accelerates towards the Rayleigh wave speed. Once the Rayleigh wave speed is reached, the secondary crack jumps to a supershear speed instantaneously.

(2) The supershear transition mechanisms we have described work not only in 2D in-plane models, but also in 3D models under certain conditions.

(3) Once the transition takes place in our models, the supershear rupture propagation can be maintained under prestress levels that are much lower than the ones predicted by the Burridge-Andrews mechanism. This shows that the level of prestress implied by the Burridge-Andrews mechanism is only needed to nucleate a crack at the site of the shear-wave peak, and not to drive the rupture to supershear speeds or to maintain that supershear propagation.

2 Simulated Model (2D)

A planar interface is embedded in an infinite, elastic and homogeneous space. The main rupture initiates from a length of $2L^c$ given in (2). In some cases, a heterogeneity exists in front of the main rupture. Depending on simulated problems, the heterogeneity may be a preexisting subcritical crack, a patch with lower static friction strength, or a patch with higher prestress.

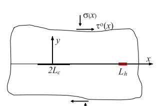

The fault strength Γ is assumed to be governed by a linear slip-weakening law:

$$\Gamma(\delta) = \begin{cases} \tau^d + (\tau^s - \tau^d)(1 - \delta/d_o) & \delta \le d_o \\ \tau^d & \delta > d_o \end{cases} \quad (1)$$

A singular shear crack with uniform prestress τ^o will propagate spontaneously if its half length exceeds a critical value L^c (*Andrews 1976*):

$$L^c = \frac{2}{\pi}\frac{\mu(\lambda+\mu)}{(\lambda+2\mu)}\frac{(\tau^s - \tau^d)d_o}{(\tau^o - \tau^d)^2} \quad (2)$$

The seismic ratio S (*Andrews 1976*) quantifies the level of prestress and is defined as $S = (\tau^s - \tau^o)/(\tau^o - \tau^d)$. Without loss of generality, we assume $\tau_d = 0$ in simulations. Rupture propagation is calculated with grid size Δx and time step Δt:

$$\Delta x = \frac{L^c}{N^c} \qquad \Delta t = \frac{\Delta x}{\beta c_s} \quad (3)$$

3 Burridge-Andrews Supershear Transition Mechanism

Based on a self-similar shear crack model, Burridge (1973) found that there is a shear stress peak $\tau^l = \tau^o + S_{crit}\left(\tau^o - \tau^d\right)$, which propagates with the shear wave speed in front of the crack. In numerical simulations of a 2D in-plane shear crack governed by linear slip-weakening law, Andrews (1976) observed that the stress τ^m at the shear wave peak gradually increases as the rupture propagates, and approaches the limiting value τ^l. If $\tau^l > \tau^s$ (or equivalently, the seismic ratio $S < S_{crit} \approx 1.63$), τ^m overcomes the fault strength τ^s in the process of rupture propagation, and a daughter crack nucleates at the shear wave front, propagating with a supershear speed.

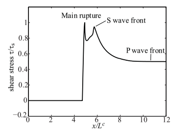

Figure: Shear stress distribution on the fault in Burridge-Andrews model.

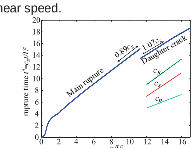

Figure: Rupture time along the fault in Burridge-Andrews model.

4 Supershear transition in our model

In the following, we will show that various other approaches, described in the abstract, are also able to trigger the rupture to go supershear.

4.1 Advancing main rupture toward a preexisting subcritical crack

To smoothly initiate main rupture and a subcritical secondary crack, we impose the following loading stress $\tau^o(x,t')$:

$$\tau^o(x,t') = \tau^o + (\tau^s - \tau^o)[1 + (1 - e^{-1})t'][e^{-\frac{x^2}{L_o^2}} + e^{-\frac{4(x-D)^2}{L_o^2}}] \quad t' < t_{crit} \quad (4)$$

where $L_o = 0.6\mu d_o/(1-\nu)\tau^s$ is half of the critical nucleation length for in-plane crack obtained by *Uenishi and Rice (2003)*, $D = 12L^c$, and $\tau^o = \tau^s/3$. This form of loading stress initiates two separate cracks at $x = 0$ and $x = D$ at $t' = 0$. At $t' = t_{crit}$, the length of the crack around $x = 0$ reaches the critical length $2L_o$, and it starts to propagate spontaneously; and the length of the crack around $x = D$ is only $1.2L_o$, therefore it remains a subcritical crack. We stop increasing the loading stress at $t' = t_{crit}$, and set $t = t' - t_{crit}$.

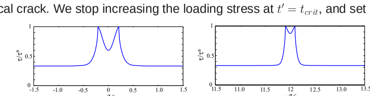

Figure: Stress distribution around the main and preexisting crack at time $t = 0$.

The right figure shows the rupture time on the fault for the case $N^c = L^c/\Delta x = 200, \beta = \Delta x/c_s\Delta t = 4$, where rupture time of a point is defined as the time when its sliding velocity becomes larger than 10^{-6} m/s for the first time. We observe that the secondary crack eventually accelerates to the speed larger than c_s, and the supershear is maintained despite the prestress lower than that of the Burridge-Andrews mechanism ($S = 2 > S_{crit}$).

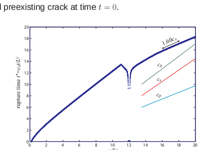

We rerun the simulations with finer resolution (larger N^c and/or β), and observe that the supershear transition always occurs within one cell length and one time step. This implies that the rupture front abruptly jumps from Rayleigh-wave speed to a supershear speed.

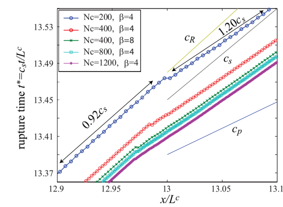

The figures on the right illustrate the transition of the secondary crack front to supershear. Snapshots of slip velocity and stress distribution on the interface are shown for $N^c = 200, \beta = 4$. (For plotting convenience, the slip velocity shown in the figures is the actual velocity plus 10^{-6}.) At time $t^* = c_st/L^c \approx 13.47$, the crack front propagates with the speed close to the Rayleigh wave speed. At $t^* = 13.49$, a daughter-like crack initiates just ONE cell ahead of the preexisting crack front, and propagates with supershear speeds immediately. This process is the same in simulations with smaller and smaller cell size Δx. Hence, in the limit of $\Delta x \to 0$, the daughter-like crack should be inseparable from the crack front, and initiate exactly at the front. This feature is fundamentally different from the Burridge-Andrews mechanism.

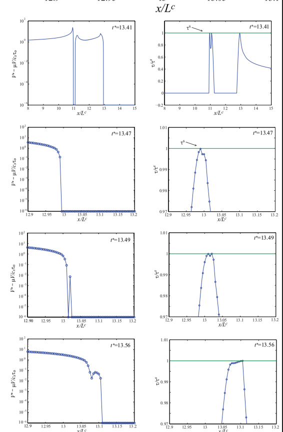

4.2 Advancing main rupture toward a patch of higher prestress

Instead of having a preexisting crack, we introduce a patch of higher prestress. The fault outside the patch has stress low compared to the Burridge-Andrews mechanism, with $S = 2 > S_{crit}$.

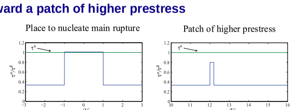

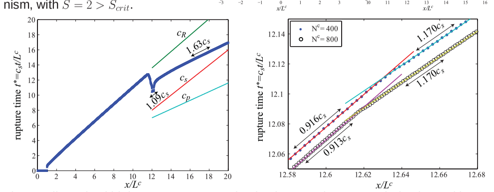

The small patch of higher prestress completely changes the rupture behavior. Without the patch, the main rupture propagates with sub-Rayleigh speeds. However, the patch (with the length $0.2L^c$ in the simulation) induces the rupture to transition to supershear, and the rupture remains supershear afterward. This shows that the level of prestress implied by the Burridge-Andrews mechanism is not needed to maintain the supershear propagation. Hence, supershear propagation on real faults can occur under prestress that are much lower than the values implied by the Burridge-Andrews mechanism.

4.3 A crack under over-stressing condition

Supershear transition can induced by overstressing a crack. Consider the case with prestress τ^o over the region $x \in [-L^c, L^c]$ set to be 0.8 times larger than the static friction strength τ^s. At the beginning of the simulation, the stress inside the patch drops from $1.8\tau^s$ to τ^s instantaneously, and spontaneous rupture propagation starts. The rupture is initially sub-Rayleigh.

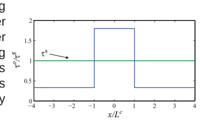

An interesting phenomenon is that both our abrupt supershear transition and the Burridge-Andrews daughter crack transition appear in the simulation. First, we observe our abrupt supershear transition without initiating a daughter crack (I in the figure below). Later we observe a daughter crack that nucleates in front of the main rupture and propagates with supershear speeds (II in the figure below).

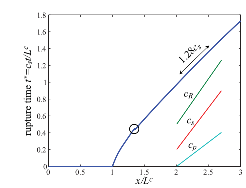

Figure: Rupture time for the case $N^c = 600, \beta = 4$.

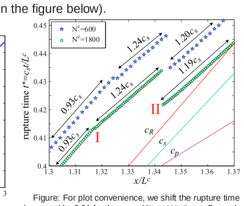

Figure: For plot convenience, we shift the rupture time downward by 0.01 for the case $N^c = 1800, \beta = 4$. Supershear transition happens twice. I denotes our abrupt transition. II denotes the Burridge-Andrews' transition.

5 Discussion

The described abrupt supershear transition mechanisms work in 3D fault models as well. We simulate the rupture propagation on a strike-slip fault interface, where a rectangular fault is surrounded by unbreakable barriers. If the model includes a patch of higher prestress or lower static friction strength, the rupture may transition to supershear speeds and the supershear can be maintained in spite of the prestress much lower than that predicted by the Burridge-Andrews mechanism. However, we notice that to trigger supershear transitions, the required patch size in the 3D strike-slip model should be much larger than that in the 2D in-plane model.

From simulations, it seems that a special loading stress τ^o is needed to cause cracks to transition to supershear. We hypothesize that the loading stress should move fast enough in the direction of the crack propagation. The most natural loading stress environment of this kind is the stress field in front of main rupture propagating with sub-Rayleigh speed advancing on a secondary crack or heterogeneity. However, there are other ways to create suitable loading stress environments. For example, we have tried to artificially impose a dynamic loading stress field $\tau^o(x,t)$ of the form $\tau^o(x,t) = f(x - c_pt)$ on a crack propagating with sub-Rayleigh speeds. We find that this also triggers supershear transition with features very similar to the preexisting crack case (4.1). Our current work is directed towards developing theoretical explanations for these phenomena.

POLYGENETIC POST-LARAMIDE MANTLE LITHOSPHERE BENEATH THE MOJAVE DESERT: THE XENOLITH RECORD

Peter I. LUFFI[1]*, Jason B. SALEEBY[1], Mihai N. DUCEA[2]

[1]Division of Geological & Planetary Sciences, California Institute of Technology, [2]Department of Geosciences, University of Arizona

*e-mail: pluffi@gps.caltech.edu

1. Introduction

Sr, Nd and Pb isotope composition of mantle-derived lavas from the Mojave Desert reveal regional scale heterogeneities of the deep lithosphere in the Miocene [Miller et al., 2000, GSA Bull]: enriched Precambrian sub-continental lithospheric mantle (SCLM) of North America has underlain the eastern part of the Desert, whereas depleted, young Farallon oceanic mantle has dominated its western part. The boundary between these domains coincides with the Sr_i = 0.706 line of Kistler and Peterman [1973, GSA Bull]. In the eastern part of the Mojave Desert this model is sustained by trace element and radiogenic isotope enriched peridotite xenoliths erupted in the Cima volcanic field in Plio-Pleistocene times [Mukasa & Wilshire, 1997, JGR]. Late Pleistocene-Holocene basanites from Dish Hill, Central Mojave Desert, erupted close to the hypothesized boundary between these mantle domains, and contain xenoliths which can help 1) refine the boundary conditions between the inferred mantle domains, and 2) evaluate whether the lithospheric mantle structure of the Mojave Desert has changed significantly after Miocene.

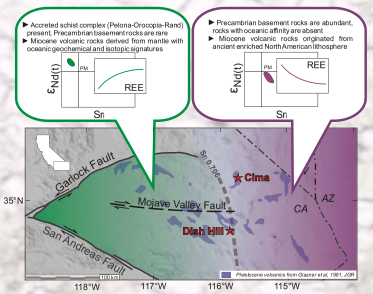

3. Inferred mantle structure beneath the Mojave Desert

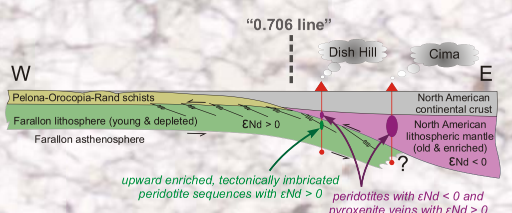

Nd isotope data combined with geothermometry results indicate that the E-W horizontal heterogeneity of the Mojave mantle inferred from lava geochemistry may be identified as vertical heterogeneity beneath Dish Hill.

Here, the uppermost mantle is relatively cold, enriched and old (T= 850-900°C, εNd = 6.4 to 13, T_{DM} > 2Ga), and corresponds to the ancient SCLM represented by xenoliths from the Plio-Pleistocene Cima Volcanic Field, whereas the deeper and hotter mantle is depleted and relatively young (T= 970-1100°C, εNd = +5.7 to +16, T_{DM} < 1Ga), and similarly to the Western Mojave basalt sources, is likely to be of Pacific (Farallon) origin.

The recurrence of compositional trends may be best explained by flat subduction-related tectonic imbrication.

Our results 1) suggest that much of the Miocene lithospheric architecture of the Mojave Desert had been preserved without noticeable changes until Holocene, 2) corroborate the idea that no significant post-Miocene extension has shaped the Mojave Desert, and 3) may place important constraints on thermal evolution and dynamics of the Farallon plate.

(Cartoon cross section adapted from Miller et al 2000, GSA)

2. Dish Hill xenoliths

Geothermometry

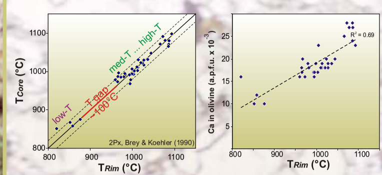

Two-pyroxene geothermometry [Brey & Koehler, 1990, JP] based on core-core and rim-rim composition pairs suggest that neither systematic cooling nor heating events are recorded by the Dish Hill xenolith suite (dashed lines correspond to the thermometer's ±20ºC uncertainty). Ca contents in olivine loosely correlate with two-pyroxene temperatures, but derivation of a meaningful geotherm is impossible due to the large uncertainties associated to the Ca-in-olivine geobarometer [±4 Kbar, Koehler & Brey, 1990, GCA, Brey & Koehler, 1990, JP]. This correlation nevertheless suggests that if a qualitative pressure correction to the 15 kbar reference pressure used for geothermometry would be applied, the temperature range covered by these xenoliths would increase with 20-30ºC. Assuming a local geotherm in the 16-25 °C/km range, the xenoliths are representative for a 10-15 km mantle column located somewhere in the 33-68 km depth range.

Compositions

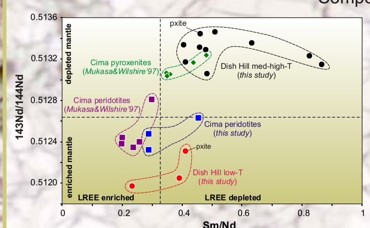

Sm/Nd vs. $^{143}Nd/^{144}Nd$ in clinopyroxenes from Dish Hill and Cima xenoliths. The four quadrants of the diagram distinguish coupled Sm/Nd ratios and Nd isotopic compositions (lower left and upper right fields) from decoupled ones (upper left and lower right fields). Xenoliths with $^{143}Nd/^{144}Nd$ plotted in the upper right quadrant are derived from a mantle source depleted in LREE, those with $^{143}Nd/^{144}Nd$ plotted in the lower left quadrant have they source in a mantle enriched in LREE for a considerable period of time. Xenoliths plotted in the other two quadrants likely have been disturbed by relatively recent metasomatic processes. Low-T xenoliths from Dish Hill and Cima Cr-diopside peridotites appear to derive from the same enriched continental mantle, whereas medium- and high-T xenoliths from Dish Hill are similar to the mantle source of Cima pyroxenites, and may be of Farallon origin.

Temperature - composition relationships

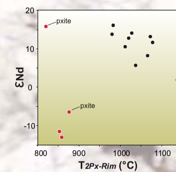

T_{2Px} vs. εNd for Dish Hill xenoliths. Medium- and high-T samples display a loose negative correlation between T_{2Px} and εNd, suggesting poor correlation between depth and depletion. Low-T xenoliths do not share this trend; therefore the gap in the lithospheric mantle beneath Dish Hill is likely both thermal and isotopic.

T_{2px} vs. bulk rock major and trace elements in medium- and high-T xenoliths from Dish Hill. Remarkably, medium- and high-T samples share the same, but thermally divided trends. This suggests that the deeper, high-εNd mantle section beneath Dish Hill is characterized by a double layered architecture, in which each layer display a top-to-bottom depletion zoning.

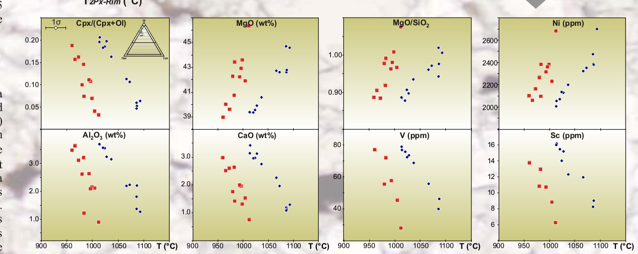

4. Implications for understanding the compositional layering of oceanic mantle lithosphere

The downwards depleted trends observed in the medium- and high-T xenolith suites from Dish Hill cannot be easily reconciled with the general view that mantle lithosphere formed at mid-ocean ridges (MOR) are largely upwards depleted due to progressive melt extraction from the uprising asthenosphere. Employing the *adiabat_1ph* software [Smith & Asimow, G[3]] and the MELTS thermodynamic database [Ghiorso & Sack, 1995, CMP] we tested the possibility to develop limited-scale upwards reenrichment trends in MOR residual peridotites. Assuming that abyssal peridotites form by combined batch and fractional melting processes [e.g. Asimow, 1999, EPSL], we calculated the compositions of solid residua resulted by adiabatic batch melting until Cpx exhaustion (*F ~ 20%*), followed by limited fractional melting along polybaric cooling paths. Our results indicate that low dP/dT polybaric cooling paths may explain the composition-depth trends of the Dish Hill medium- and high-T peridotites in terms of most major elements, except Si and Na. Whereas SiO_2 discrepancies rather may be related to the employed thermodynamic database, Na_2O differences are more likely of natural origin, and need further considerations.

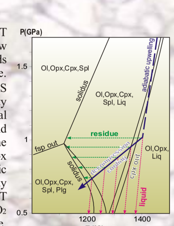

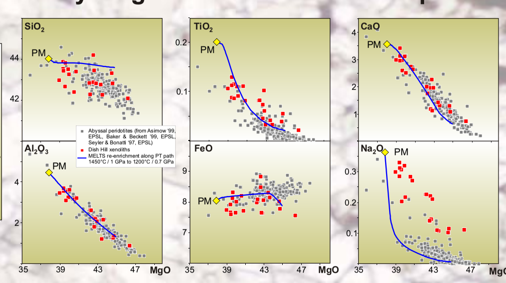

5. Summary

- Mantle xenolith suite from Dish Hill reveal juxtaposition of old, isotopically enriched North American lithosphere and younger, isotopically depleted Farallon slab beneath the central Mojave Desert during the Late Pleistocene-Holocene. This conclusion constrains geodynamic models of the Southwestern United States .
- Compositional trends in medium- and high-T xenoliths suggest subduction induced tectonic imbrication in the Farallon slab.
- Adiabatic batch melting combined with limited fractional melting along polybaric cooling paths in MOR environment may explain the top-to-bottom depletion trend observed in the Dish Hill peridotites.

ACKNOWLEDGEMENTS
P.L. gratefully acknowledges discussions and constructive suggestions by Paul Asimow. This research was supported by the Caltech Tectonics Observatory.

WESTERN NORTH AMERICA NEVADA GPS PROJECT, 2006

Faculty Participants: Brian Wernicke, Mark Simons, Kerry Sieh
Postdocs: Richard Briggs, Kevin Mahan
Staff: Jeff Genrich

Abstract

The Nevada GPS project was funded as a strategic augmentation of planned Earthscope continuous GPS sites in the Basin and Range, with the objective of producing dense enough coverage to observe and model apparent migratory strain in north-central and eastern Nevada. As extensively discussed in TO western US working group meetings, and published this summer (Davis JL, Wernicke BP, Bisnath S, et al., 2006, Nature - see below), this region of the Basin and Range forms a boundary zone between accelerating sites in the western Basin and Range and non-accelerating sites to the east. These large-aperture observations over the last decade are the first to suggest relatively efficient anelastic energy transfer across a deforming plate boundary zone at human timescale, which in turn could be a major control on the seismic cycle and rheology of the lithosphere. Full characterization of strain waves down to ~100 km wavelength will be possible with the ~30 km site spacing of the densified network.

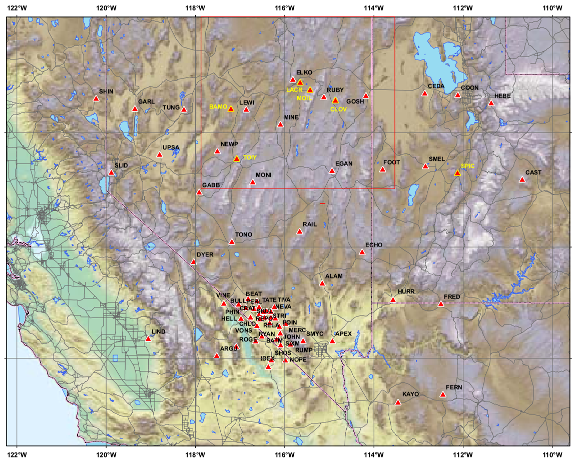

Map of western North America showing the locations of continuous GPS stations operated by the California Institute of Technology under the auspices of the National Science Foundation, the Department of Energy's Yucca Mountain Project and the Tectonics Observatory. As of Novemeber 2006, there are 74 stations operating in California, Nevada, Utah, and Arizona. Six GPS sites funded by the Tectonics Observatory are highlighted in yellow. New sites built this year as part of the Yucca Mountain in southern Nevada project are identified with roman textface.

Tectonic Implications

We speculate that an episodically creeping detachment horizon ~500 km wide at or near the base of the crust may provide a general explanation for the velocity changes. In one scenario, the mantle would either translate or stretch smoothly below the horizon, imparting a westward component of shear traction on the base of the crust (<1997–~2000). Top-to-the-east plastic yielding along the horizon translates the crust eastward en bloc, as internal stretching and shear of the crust continues. Yielding thus relaxes stress on the eastern margin of the accelerating domain (where baselines ELKO-GOSH and EGAN-FOOT were contracting at ~0.5 and 1 mm/yr, respectively), and focuses strain accumulation (2000–3), and subsequently strain release (2003-4) along the western margin of the domain. An active decoupling zone at the base of the crust under the Nevada Basin and Range, accompanied by magmatic injection, has long been suspected on the basis of nearly continuous, bright seismic relections along the Moho. Like the GPS velocity change, these reflections also die out near the Nevada-Utah border, suggesting the reflection Moho is a coherent structure that episodically yields, thereby transferring strain energy hundreds of kilometers across the province.

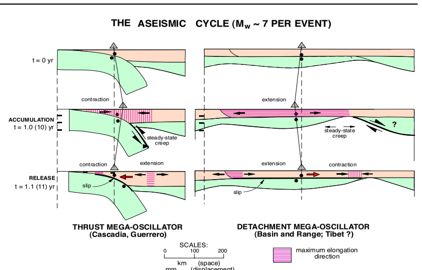

Subcontinental-scale Transient Deformation along Pacific-N. America Boundary

Davis, J.L., Wernicke, B.P., Bisnath, S., Niemi, N.A., Elosequi, P., 2006, Nature 441: 1131-1134

Transient tectonic deformation has long been noted within ~100 km or so of major plate boundary faults zones and within active volcanic regions, but do transient motions also occur at larger scales within plates? We report the first geodetic evidence for a coherent, subcontinental-scale change in tectonic velocity along a diffuse, ~1000-km wide deformation zonebased on continuous GPS observations over the last decade across the Basin and Range province Basin and Range deformation absorbs approximately 25% of Pacific-North America right-lateral transform motion, expressed by east-west extension in Utah and north-northwest right-lateral shear in western Nevada and eastern California. Changes in site velocity define a sharp boundary near the centre of the province oriented roughly parallel to the north-northwest relative plate motion vector. From 1999.5 to 2001.0, sites to the west of this boundary slowed relative to sites east of it by ~1 mm/yr.

Relatively localized transients are known to occur as both seismic and episodic aseismic events1, and are generally ascribed to motions of magma bodies, aseismic creep on faults, or elastic or viscoelastic effects associated with earthquakes. However triggering phenomena and systematic patterns of seismic strain release at subcontinental (~1000 km) scale along diffuse plate boundaries, have long suggested that energy transfer occurs at larger scale. Such transfer appears to occur by the interaction of stresses induced by surface wave propagation and magmas or groundwater in the crust, but do mechanisms not directly associated with earthquakes also exist?

We have addressed this issue by constructing the Basin and Range Geodetic Network (BARGEN), the first 1000 km-aperture continuous GPS network to be deployed across an actively deforming plate boundary zone. Eighteen sites, comprising an east-west transect between latitudes 39°N and 41°N (map above), began recording in 1996–7; time series are now long enough for us to obtain statistically reliable estimates of any changes in velocity that might occur on a regional scale. Dual-frequency GPS phase data were first analyzed in the usual way using GAMIT/GLOBK, resulting in estimated average velocities and time series in a North American reference frame. The average horizontal velocities of the sites rise from near zero in the east to ~3 mm/yr due west across western Utah, remain relatively constant across eastern Nevada, and then rotate northwestward and progressively increase up to ~12 mm/yr in the Sierra Nevada.

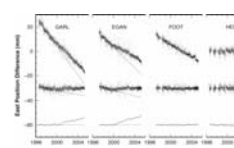

Illustration of the post-analysis procedure, using time series of east position for four BARGEN sites. Top: "Raw" time series, in a North-America-fixed geodetic reference frame. Error bars are omitted for clarity, but are generally ~1 mm. The straight line is the best-fit straight line using points from the first 2.5 years. Middle: Residuals of the raw time series from a best-fit model consisting of a straight line and seasonal (annual and semi-annual sinusoids) terms. A spatial filter5 with mean, rate, and acceleration constrained to zero has been applied. Bottom: Residuals smoothed with a Gaussian filter of width 0.04 yr (~15 days), and sampled every 0.04 yr. A model based on a linear fit to the first 2.5 yr of data has been removed. The evolution of these final time series thus indicates deviation from temporally linear motion.

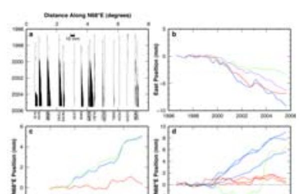

Analysis of spatial variation of nonlinear deviations. **a**, Smoothed time series of smoothed position deviations from linear motion in the direction N68°E, projected along a great circle with azimuth N68°E near the centre of the network. Where these deviations are positive, the space between the trace and zero has been shaded black. The significant deviations occur in the western part of the network. **b**, East components of intersite vectors for EGAN-FOOT (red), ELKO-GOSH (green), GARL-HEBE (blue), and MINE-SMEL (purple). GARL-HEBE, which spans the entire network east-west, and EGAN-FOOT, which spans a short distance in the centre of the network show nearly identical deviations, indicating an abrupt boundary for velocity changes in eastern Nevada. **c**, Regionally averaged non-linear deviations of N68°E position. Red: Eastern BARGEN (HEBE, FOOT, COON, CAST, CEDA, SMEL, GOSH, and RUBY). Green: TUNG, ELKO, EGAN, LEWI, NEWP, GARL, UPSA, and SHIN. Blue: Same as green plus SLID. Only data from a common epoch range (1997.86–2005.18) were used. The figure demonstrates that the velocity change has moved the western part of the network, on average 3–4 mm eastward or northeastward compared to the eastern part of the network. The shorter period features that are anticorrelated are artefacts of the spatial filtering technique, but may indicate regional coherence on these time scales at amplitudes less than ~1 mm. **d,** N38°E position time series for three groups of sites. Red: eastern sites RUBY, FOOT, and HEBE. Blue: western sites EGAN, MINE, and GARL. Green: Site SLID.

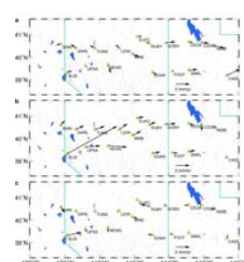

Differences of horizontal velocity for one-year periods relative to the average velocities for the period 1997.0-2002.0. a) Differences for the calender year 2002. b) 2003. c) 2004. 1 sigma errors for each component are ~0.4 mm yr-1 Note "displacement wave" beginning with eastward motion of Utah sites in 2002 prior to SLID's large motion in 2003 (correponding to a magmatic injection event beneath Lake Tahoe), which accompanied by west by eastward motion of all Nevada and some Utah sites. This behavior suggests largely aseismic transfer of strain energy at 1000 km length scale.

The current project plan, as both TO and PBO sites come on-line, is to begin archiving and annual processing of data from the group of sites shown in the map below and listed in the table below, which consists of approximately 35 sites. In conjunction with this work, we hope to begin an investigation of the only major normal fault along the transects for which no paleoseismological slip estimate is available, the Ruby Valley fault zone. This fault bounds the east side of the Ruby Mountains, Nevada, just west of site Ruby (Figure 1). In addition, over the next year we will begin dislocation modeling efforts to test the hypothesis that velocity changes are the result of rapid transient slip (of order cm/yr) on the down-dip extensions of the large active normal faults along the transect (see below).

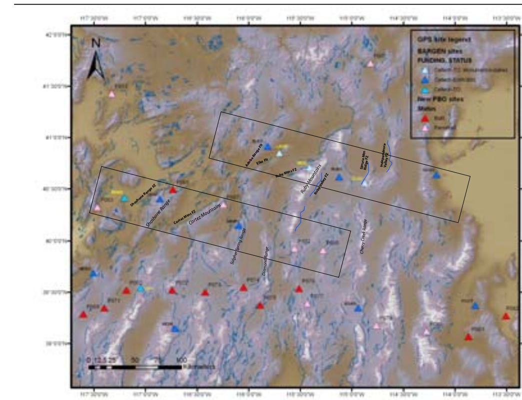

Siting for three new continuous TO sites (CLOV, MOIL and LACR) was completed in early fall 2005, densifying the existing BARGEN transect that includes sites ELKO, RUBY and GOSH (see above). Permits were secured by the summer of 2006, and monumentation has been completed. Electronics installation and bringing the sites on-line will begin in early November 2006. Close coordination between TO and the PBO siting committee enabled all of the earlier proposed densification of the Mount Lewis area to be absorbed by PBO, such that the transect including TO sites BAMO and TOIY will be densified to ~30 km station spacing. The close station spacing will permit robust testing of elastic dislocation models for individual faults, including the western range front faults for the Ruby Mountains, Cortez Range and Shoshone Range, as well as comparison of geodetic rates with previous estimates of late Cenozoic strain release rates from paleoseismological methods. Robust velocity estimates (± 0.2 mm/yr intersite velocity) will be available by fall 2008.

Are Basin and Range normal faults creeping episodically in their lower regions?

The original BARGEN network included site spacing across central Nevada of about 80 km, with significant (1-2 mm/yr, about 10 sigma) amplitude of velocity variations for sites near latitude 40°N. This is a surprising result because overall this part of Nevada is not systematically deforming, i.e. the velocities as a whole define a remarkably stable tectonic block (red curve, showing west velocities as a function of longitude, diagram at lower right). The simplest hypothesis to explain these variations is rapid, transient creep on the deep portions of Basin and Range normal faults in the area, which would be most obvious in a slowly straining region. Calculations of surface deformation due to deep crustal creep on a Basin and Range faults (below, right) show that at 80 km spacing we are sampling at less than half the Nyquist frequency for the waveforms predicted by fault creep at depth. With the strategic augmentation of three new TO continuous GPS sites (coming on-line in November 2006) and about five sites from the national PBO, we will have about 14 sites at ~40 km spacing covering the geodetically complex region of contractile and extensional strain near BARGEN sites TUNG, LEWI, MINE, ELKO, RUBY, and GOSH. These stations from two en echelon arrays that cross the major normal faults in the region (see site location figure). With this station spacing, we will be able to indentify and test physical models that might explain such waveforms. The high velocity accuracy we expect after about 2 years (roughly, the size of the triangles shown on the models below), the GPS data will rigorously limit the range of possible models.

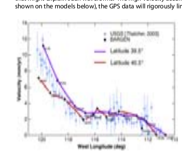

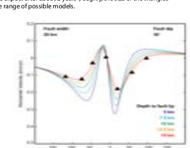

new PBO sites

PBO Dot #	Status	or earliest data	Longitude (deg. E)	Latitude (deg. N)	Location
P002	Built		-117.187	39.521	Austin
P005	Permitted		-115.279	39.910	Wild Horse Point
P007	Permitted		-114.820	41.724	Salmon Falls Creek
P013	Permitted		-117.329	41.428	Spring Creek
P069	Built		-117.605	39.288	Campbell Creek
P071	Built		-117.401	39.347	Railroad Pass
P072		Jun-05	-116.741	39.521	Dry Creek
P073	Built		-116.424	39.501	Twin Spring Hills
P074	Built		-116.050	39.546	Devon Peak
P075	Permitted		-115.889	39.374	Pinto Summit SW
P076		Oct-06	-115.513	39.536	Dry Mountain
P077	Permitted		-115.432	39.389	Raven Loft
P079	Permitted		-114.763	39.175	Wagner Flat
P080	Permitted		-114.277	39.119	Willow Patch Spring
P081		Apr-06	-113.871	39.067	Middle Point
P082		May-06	-113.505	39.269	Smelter Hills
P083	Permitted		-117.468	40.321	Tobin Range
P085		Sep-06	-116.736	40.495	Slaven Canyon
P087	Permitted		-116.247	40.349	Cortez Flat
P102	Permitted		-115.556	39.925	Little Bald Mtn

new Tectonics Observatory sites

SITE	Status or earliest data	Longitude (deg. E)	Latitude (deg. N)	250K_QUAD
LACR	install Nov 2006	-115.704	40.851	
MOIL	install Nov 2006	-115.411	40.710	
CLOV	install Nov 2006	-114.874	40.558	

BARGEN sites now part of PBO

SITE	Status or earliest data	Longitude (deg. E)	Latitude (deg. N)	250K_QUAD
NEWS	Oct-97	-117.509	39.686	Millett
TOIY	Feb-03	-117.049	39.542	Millett
FOOT	Mar-97	-113.805	39.369	Delta
ELKO	Oct-97	-115.817	40.915	Elko
RUBY	Jul-96	-115.123	40.617	Elko
GOSH	Jul-96	-114.180	40.640	Elko
EGAN	Mar-97	-114.939	39.345	Ely
LEWI	Jul-96	-116.862	40.404	Winnemucca
MINE	Oct-97	-116.096	40.148	Winnemucca
BAMO	Feb-03	-117.205	40.413	Winnemucca

BARGEN sites part of southern B & R network (Yucca project)

SITE	Status or earliest data	Longitude (deg. E)	Latitude (deg. N)	250K_QUAD
MONI	Mar-99	-116.716	39.148	Millett

THE "SIMEULUE SADDLE": AN ASEISMIC PATCH OF THE SUNDA MEGATHRUST?

Aron Meltzner, Kerry Sieh, Rich Briggs, John Galetzka, Willy Amidon (Tectonics Observatory, California Institute of Technology),
Bambang Suwargadi, Danny Hilman Natawidjaja, Dudi Prayudi (Indonesian Institute of Sciences – LIPI Geotechnology), and Imam Suprihanto

INTRODUCTION: THE QUESTIONS

The December 2004 and March 2005 Sunda megathrust earthquakes nucleated northwest and southeast of Simeulue island, respectively, and each ruptured bilaterally into the 100-km-long island. Uplift at the northwestern tip of Simeulue was 1.5 m during the 2004 earthquake, and uplift at the southeastern tip in 2005 was 1.5 m or more. Uplift associated with each earthquake diminished toward the center of the island, as did slip on the underlying megathrust, according to slip inversions. Cumulative uplift was as little as 0.5 m along the west coast of central Simeulue. Hence, although the 2004 and 2005 uplifted regions overlap, there is an uplift deficit, or saddle, on central Simeulue. Rupture during an M_W 7.3 earthquake in 2002 produced up to ~20 cm of uplift on the west coast of central Simeulue, near the sites of lowest uplift in 2004-2005, but even including that uplift, the saddle persists. No events similar to 2002 can be found in the historical record for at least the previous 94 years.

The occurrence of the 2002, 2004, and 2005 earthquakes, their relative locations and timing, and their associated patterns of uplift raise important questions about rupture boundaries, earthquake triggering, and long-term behavior of these patches of the fault. Why didn't the 2004 earthquake continue southward to encompass the future 2005 rupture? Why didn't the 2002 earthquake continue farther onto the 2004 or 2005 rupture planes? It does not appear that the 2002 and 2004 ruptures extended into regions of recent high slip. Could the rupture terminations have been controlled by permanent structural boundaries?

Preliminary analysis of survey data from our 2005 and 2006 field seasons and of x-rays of slabbed *Porites* coral microatolls, coupled with a paucity of large historical earthquakes in the region, suggests that the central Simeulue region may experience occasional aseismic slip events, or that moderate earthquakes (M<7) may account for a significant fraction of the uplift during a 2004- or 2005-type earthquake cycle.

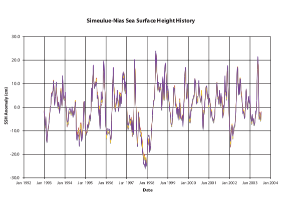

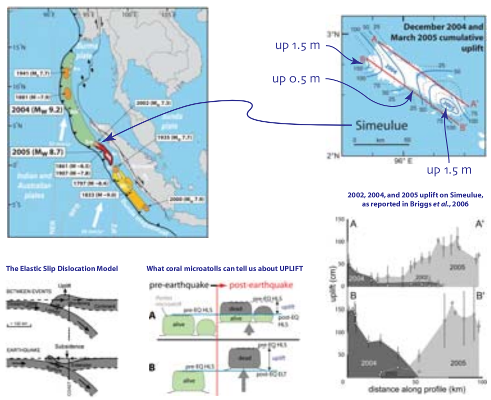

In northern Simeulue, the uplift occurred in the 2004 earthquake. In southern Simeulue, the uplift occurred in the 2005 earthquake. In central Simeulue, only a fraction of the uplift occurred.

The island's topography shows similar segmentation and suggests that central Simeulue may be a long-lived barrier to earthquakes.

OBSERVATIONS: THE WESTERN SIMEULUE SADDLE

OBSERVATIONS: THE EASTERN SIMEULUE SADDLE

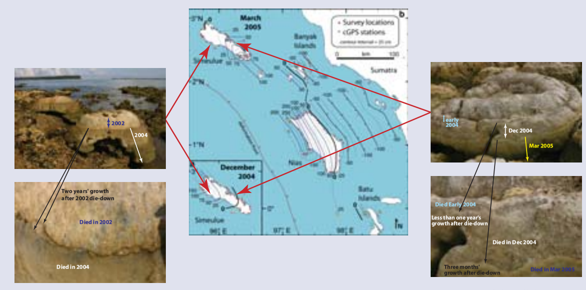

OBSERVATIONS: THE WESTERN SIMEULUE SADDLE

OBSERVATIONS: THE EASTERN SIMEULUE SADDLE

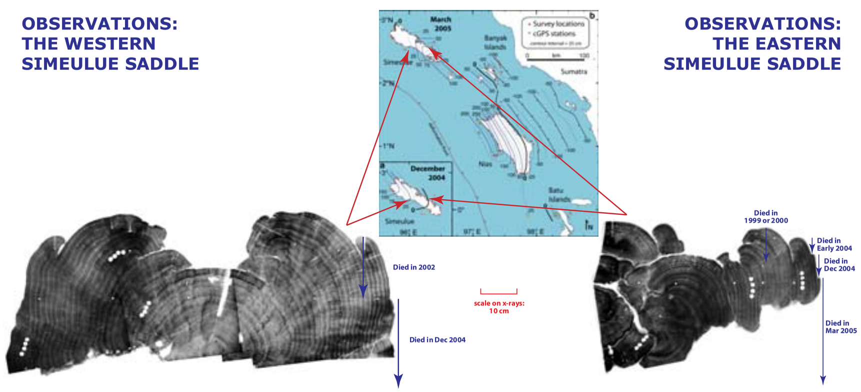

The saddle in cumulative slip at the juncture of the 2004 and 2005 ruptures under central Simeulue may be similar to the Batu Islands segment, a long-lived largely aseismic barrier to rupture during giant earthquakes.

A 100-km section of the megathrust at the Equator has been a barrier to rupture for at least the past 4 neighboring giant earthquakes.

Large uplift during the M_W 7.7 1935 earthquake

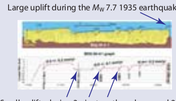

Small uplifts during 3 giant earthquakes ... and 2005

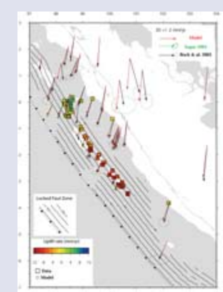

Modeling of coral and GPS data shows that the Batu islands patch is largely aseismic. The largest rupture in this patch since ~ 1750 was an M_W 7.7 in 1935.

Our hypothesis is that the Simeulue saddle, like the Batu islands patch, reflects a long-lived region of aseismic slip and moderate earthquakes

Phosphorus Zoning in Olivine: An Additional Constraint on Magmatic Processes in Arc Volcanism

Zachary T. Morgan, Edward M. Stolper, Michael B. Baker, Daniel Vielzeuf, and Fidel Costa

Introduction/Context

Arc lavas contain abundant evidence of disequilibrium processes, in the form of concentration profiles, reaction rims, and dissolution features. Many of these disequilibrium features can be used to determine the time scales of the magmatic events resulting in their formation. Previous studies have used zoning in plagioclase and/or olivine, reaction rims on olivine, and amphibole break down rims to infer the time from the disequilibrium event to eruption.

Previous work by Fidel Costa used zoning in olivine or plagioclase to infer the time scales of magmatic processes. Costa and Chakraborty (2004) looked at Fe-Mg zoning in olivine to calculate the time scales of olivine incorporation into dacite and andesite magmas. They focus on four lavas from Volcan San Pedro in the Southern Volcanic Zone of Chile (a and b). The lavas are three dacites (Qcf1, Qcf2, and Qcf3) and one andesite (Qcf4). None of these magmas lie in the low-pressure olivine phase volume so its presence is assumed to be the result of magma mixing with a more mafic magma (i.e, basaltic andesite, Costa and Chakraborty, 2004) or assimilation of mafic to ultramafic lithologies (Costa and Dungan, 2005). The Fo (or Mg#) profiles in olivine reported in Costa and Chakraborty (2004) are reproduced for each of the studied olivines. As illustrated the Fo (Mg#) zoning can be complicated, but their model focused on the outer-most zone developed during the last stage prior to eruption. The time scales calculated for olivine incorporation range from less than a year for Qcf1 to 0.8 to 91 years for Qcf2, Qcf3, and Qcf4.

Recent studies of zoning in olivine suggest that just focusing on the major elements such as FeO and MgO maybe insufficient. Certain trace elements such as the slower diffusing P_2O_5, Al_2O_3 and Cr_2O_3 may record important information about the olivine growth history that is not retained by the faster diffusing species. Milman-Barris et al. (2006) described complex zoning of P_2O_5, Al_2O_3 and Cr_2O_3 in natural olivines from Hawaiian lavas, komatiites and a Martian meteorite. In addition, their linear cooling rate experiments on a Hawaii bulk composition produced olivine with strong zoning in P_2O_5, Al_2O_3 and Cr_2O_3. They attributed the P_2O_5, Al_2O_3 and Cr_2O_3 zoning to rapid growth of the olivine.

The purpose of this study is to examine olivine from arc lavas for zoning in P_2O_5, and to explore the effects this zoning will have on the model and time scales estimated by Costa and Chakraborty (2004).

a) b)

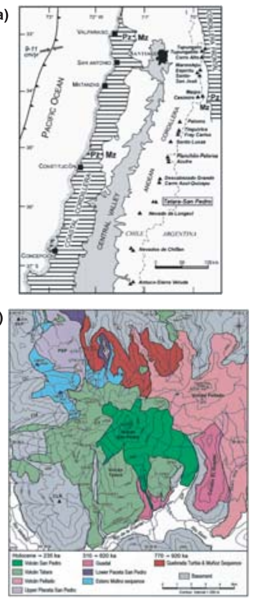

Qcf1: Dacite, SiO_2 = 65.8%, T = 850 C

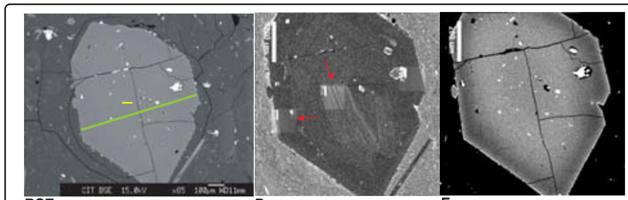

BSE | P x-ray map | Fe x-ray map

This olivine has two distinct zoning features: complex banding of P_2O_5 in the core of the grain (P x-ray map) and a 100 micron band of higher Mg (lower Fe) concentration (Fe x-ray map and Mg# profile) in which P_2O_5 zoning is absent. The red arrows on the P x-ray map point to P_2O_5 zoning in the core and the region near the rim of the grain where P_2O_5 zoning is absent. The green line on the BSE image corresponds to the Fo profile. The yellow line on the BSE image corresponds to the P_2O_5 profile. The P_2O_5 profile illustrates the detailed nature of the P_2O_5 zoning in the core of the grain.

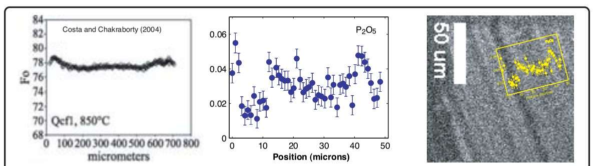

Mg# Profile | P_2O_5 Profile | P x-ray map

Qcf2: Dacite, SiO_2 = 64.5%, T = 875 C

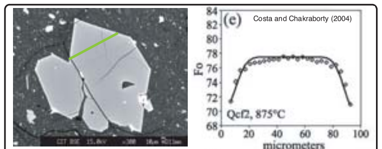

BSE

Grain 1 — P x-ray map | Fe x-ray map

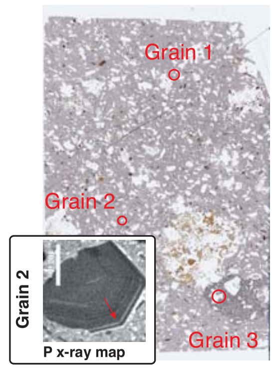

Grain 2 — P x-ray map

Grain 1: This olivine has two distinct zoning features: a higher Fe concentration rim (outer 10 microns, Fe x-ray map) where P_2O_5 zoning is absent and P_2O_5 rich zoning in the interior of the grain. The red arrows on the P Xray Map point to P_2O_5 zoning in the core of the grain. The green line on the BSE image corresponds to the Fo profile.

Grain 2: The P_2O_5 zoning in this olivine grain occurs as bands parallel to the crystal faces.

Grain 3: This grain occurs in a more mafic inclusion in the dacitic magma. The P_2O_5 zoning in this olivine is combination of patchy P_2O_5-rich zones in the interior and a faint band parallel to the crystal face. Similar to the Qcf1, there is a 100 micron band near the outer edge of the grain with lower FeO (higher Fo, Mg# profile) and an abence of P_2O_5 zoning. The red arrows on the P x-ray map point to features in the P_2O_5 zoning region. The green line on the BSE image corresponds to the Fo profile.

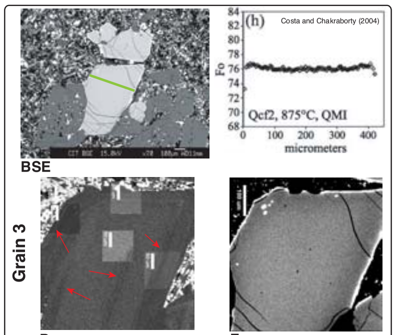

Grain 3 — BSE | P x-ray map | Fe x-ray map

Qcf3: Dacite, SiO_2 = 63.6%, T = 925 C

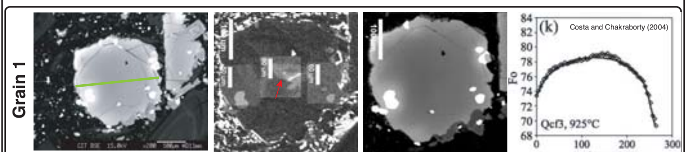

Grain 1 — BSE | P x-ray map | Fe x-ay map

These grains do not have good crystal faces. The red arrows on the P x-ray map point to features in the P_2O_5 zoning region. The P_2O_5 zoning is patchy in the interior of the grain (Grains 1 and 2); grain 2 also has a suggestion of P_2O_5 banding near the edge of the crystal. The green lines on the BSE images correspond to the Fo profiles.

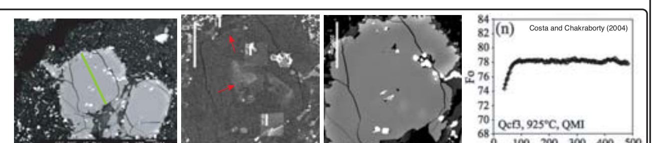

Grain 2 — BSE | P x-ray map | Fe x-ray map

Qcf4: Andesite, SiO_2 = 61.4%, T = 950 C

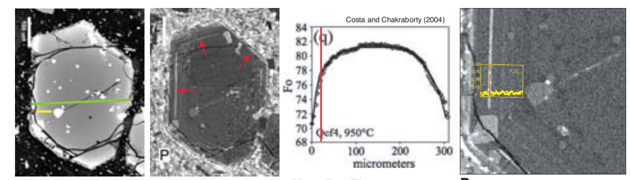

BSE | P x-ray map | Mg# Profile | P x-ray map

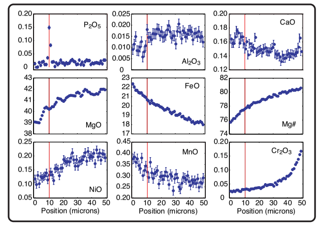

Like Qcf2 grain 2, the primary P_2O_5 zoning in this grain is P_2O_5 rich bands parallel to the crystal faces. The red arrows on the P x-ray map point to strong P_2O_5 bands. The green line on the BSE images corresponds to the Fo profiles. The red line on the Mg# Profile marks the position of the P_2O_5 rich band relative to the Fo profile. This suggests that (at least for this case) the interpretation of Costa and Chakraborty (2004) that the zoning in Fe-Mg is the result of simple diffusive exchange between the olivine and the host liquid is not correct. Instead we suggest that a new rim of olivine with a different Fo content (marked by the P_2O_5 rich band) grew on a pre-existing olivine crystal. Diffusive exchange between the new olivine rim, the pre-existing core and the host magma resulted in the observed Fo profile. However, the concentration of slower diffusing species such as P_2O_5 and Al_2O_3 did not change significantly. This suggests that the time scales estimated by Costa and Chakraborty (2004) are over estimates and the actual time was shorter.

Spinel Zoning

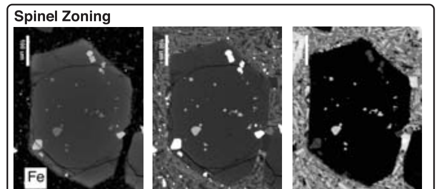

Fe x-ray map | Ti x-ray map | Al x-ray map

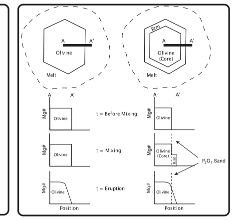

The magnified P x-ray map illustrates the P_2O_5 banding, on which I've superimposed a quantitative profile taken across a portion of the crystal. The quantitative profile illustrates the P_2O_5 concentrations that are qualitatively described by the x-ray map.

Additional evidence for our hypothesis of a later stage rim on the olivine comes from spinel inclusions hosted within the olivine grain. The Fe, Ti, Al and P x-ray maps illustrate that spinel inclusions on the outer edge of the grain have high Fe, Ti and P and low Al relative to spinel inclusions in the core of the olivine.

Summary/Future Work:

As with previously examined olivine from other tectonic environments (Milman-Barris et al., 2006), olivines from arc lavas contain complex zoning in P_2O_5. The types of P_2O_5 zoning in olivine we have observed are bands parallel to the crystal faces (Qcf2 grains 1 and 2, Qcf3 grain 2, and Qcf4), bands in the interior of the grain (Qcf1), and irregular patches in the interior of the grain (Qcf2 grain 1, and Qcf3). Ultimately, the complex zoning will better constrains the growth histories of the olivine and lead to a greater understanding processes involved the timing of mixing and eruption events in arc lavas. However, in the shorter term the P_2O_5 zoning coupled with Fe-Mg zoning can be used to refine models and estimates for olivine residence times in lavas, as is illustrated with Qcf4.

The next step of this study is to collect P x-ray maps for a population of different olivine in the same section to characterize the P_2O_5 zoning for each lava. Are the types of P_2O_5 zoning in olivine distinct for a given lava or is there a continuum of P_2O_5 zoning common to all of the lavas?

In addition, we will modify the model used by Costa and Chakraborty (2004) to estimate the olivine residence times to include a rim of new olivine similar to Qcf4. What is the effect on time estimates when a rim of new olivine is added to a pre-existing olivine? Are the changes to the olivine residence times consistent for all olivine in a given lava?

References:
Costa, F., Chakraborty, S. (2004), Decadal time gaps between mafic intrusion and silicic eruption obtained from chemical zoning patterns in olivine, *Earth Planet. Sci. Lett.*, 227, 517-530.
Costa, F., Dungan, M., (2005), Short time scales of magmatic assimilation from diffusion modeling of multiple elements in olivine, *Geology*, 33, 837-840.
Milman-Barris, M.S., Hofmann, A.E., Beckett, J.R., Morgan, Z., Baker, M.B., Daniel Vielzeuf, D., Stolper E.M., (2006), Zoning of phosphorus in magmatic olivine, Abstract, *Geol. Soc. Amer.*.

Heavenly Mountains, Down-to-Earth Job

By Elisabeth Nadin

Tien Shan is Chinese for "heavenly mountains"—the name alone reflects how hard it is to get there. In June 2006 a group of 21 Caltech students, postdocs, and professors made the trip to this remote region of northwestern China as participants in a two-week research field trip, sponsored by the Institute's Division of Geological and Planetary Sciences. After landing in Beijing, we flew to Urumqi, capital of the Xinjiang Province—where the range is located—and caught up with the 15 Chinese students and four professors who had traveled 48 hours by train from the east-coast city of Nanjing to join us. A 10-hour drive to the southwest Tien Shan foothills brought us to this arid central Asian landscape of red, yellow, and brown rocks cut by lethargic rivers.

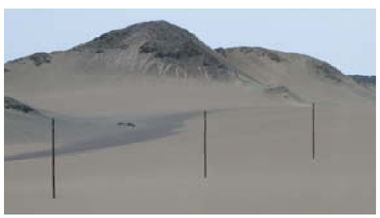

Top to bottom:
Jean-Philippe Avouac discusses the Quilitak anticline.

An Uyghur merchant passes tilted rock beds.

A spectacular scene of the stark wilderness, with Paleozoic rocks in the background.

At right, Jean-Philippe Avouac explains the interactions between the tilted rock layers and overlying terraces, as Nanjing University geology professor Shengli Wang looks on.

The banner at the top of the page shows the Tien Shan's Qilitak anticline, a large fold that formed over a blind thrust. Fault-bend folds formed the core of the field investigations. Minibuses in the foreground give a sense of how enormous it is.

Below that, a closeup of one of the limbs of the fold, showing sheared thrust offsets (tops to left) consistent with the compressive field.

Above: a map of eastern Asia—red stars show our short stops, and the blue star is on the Tien Shan.

Left: Satellite image centered on the Tien Shan.

Top left: Min Chen collects samples as Rob Clayton looks on.

Top right: Our happy home for two weeks.

Middle left: Coal mining in the Tien Shan.

Middle right: Nanjing University student Bao Xue and Caltech undergrad Sonia Tikoo check the quality of seismic images coming from geophones into a field computer.

Above: Growth strata!!

Left: A nice meal hosted by the Tarim oil company.

Top: Our happy group, at the end of a field day.

Above right: Uyghur men and their delicious fruit.

Above: Our fleet.

Left: Caltech geophysics professor Rob Clayton, with the help of two students, triggers seismic waves with the Betsy gun.

Below: Built along the Silk Road in the third century and abandoned in the tenth century when Islam became a dominant force in the region, these hillside Buddhist caves known as the Kizil grottoes still stand today, although many paintings from their ceilings and walls were plundered for their gold foil or removed by archaeologists.

Western central Andean neotectonics: What we know and where we go from here

J. Bruce H. Shyu, Mark Simons, and Jean-Philippe Avouac, Tectonics Observatory, California Institute of Technology

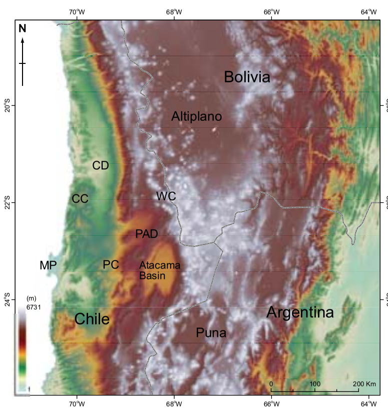

Figure 1. The western South American margin is one of the most active plate boundaries in the world. The central segment of the belt, between about 15°S and 28°S, also includes the Altiplano-Puna, one of the largest and highest plateaus in the world, where average elevation is above 4 km. Along this segment, the subducting Nazca plate has a 30° ("normal") angle of subduction. The western central Andes are characterized by several N-S trending topographic units. From west to east, these units are the Coastal Cordillera (CC), the Central Depression (CD), the Precordillera (PC), and the Western Cordillera (WC) which forms the crest of the range. Between about 22°S and 26°S, a Preandean Depression (PAD), including the Atacama Basin, appears between the Precordillera and the Western Cordillera. Also at this latitude, several normal faulted blocks form the Mejillones Peninsula (MP) that extends westward into the Pacific Ocean.

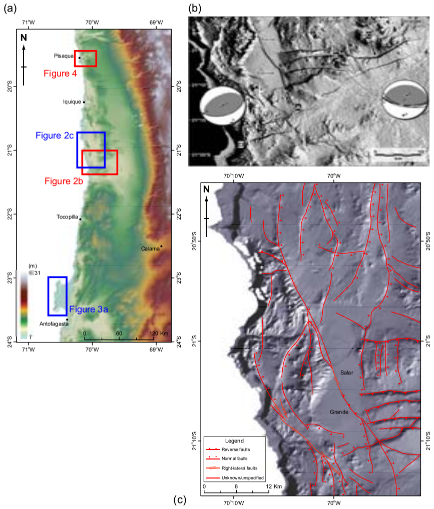

Figure 2. Selected previous mappings of possible active structures in Coastal Cordillera. (a) Shaded relief map of Coastal Cordillera. (b) Between 19°S and 21°30'S, Allmendinger et al. (2005) identified a series of E-W striking scarps, and suggested that they are reverse fault scarps, primarily on the basis of structural observations and measurements in limited outcrops. However, since these scarps are very linear and sometimes even convex toward the upthrown block, they seem more likely to be strike-slip or normal fault scarps. (c) Gonzalez et al. (2003) have produced a map of possible active structures in the Salar Grande area, on the basis of topographic features shown in the DEM. Many of the mapped structures, however, may have been active at very different times, since these structures sometimes form structurally unreasonable cross-cutting relationships.

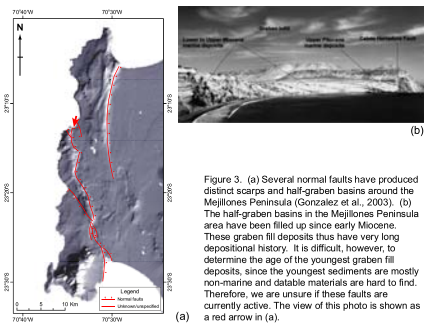

Figure 3. (a) Several normal faults have produced distinct scarps and half-graben basins around the Mejillones Peninsula (Gonzalez et al., 2003). (b) The half-graben basins in the Mejillones Peninsula area have been filled up since early Miocene. These graben fill deposits thus have very long depositional history. It is difficult, however, to determine the age of the youngest graben fill deposits, since the youngest sediments are mostly non-marine and datable materials are hard to find. Therefore, we are unsure if these faults are currently active. The view of this photo is shown as a red arrow in (a).

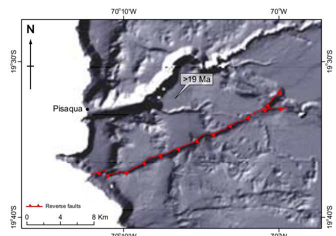

Figure 4. Although many of the previously mapped active structures were identified since they have formed scarps at the surface, the "surface" in Coastal Cordillera may in fact be very old. For example, a recent exposure dating study indicates that some of the sediments at the surface are older than 19 Myr old near Pisaqua (Dunai et al., 2005). Therefore, the fault considered to be active because they offset these surficial sediments, as mapped by Allmendinger et al. (2005) here, may have been inactive for tens of millions of years.

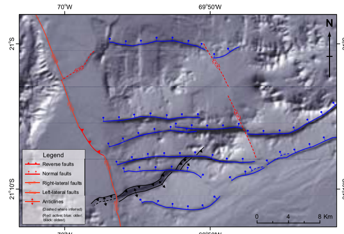

Figure 5. Occasionally, cross-cutting relationships between structures can help us distinguish systems of different ages. In this preliminary map, which has roughly the same area as shown in Figure 2b, we have identified three different structure systems that appear to be active at different times. The oldest system is a NE-SW striking reverse fault, with an anticline in its hanging-wall block. The second system is a series of E-W striking dip-slip faults with possible dextral component. The youngest system is a NW-SE striking dextral fault system, which is the only system that appears to be active currently. There are, however, many other scarps in the area that are difficult to characterize.

This experience led us to realize that, for Coastal Cordillera, due to the lack of active drainages to serve as offset markers and the fact that offset surface may be very old, we need to find structures with cross-cutting relationship in order to figure out which structure system is likely to be currently active. Such relationship is, however, not easy to find. A systematic knowledge of surface ages may therefore be needed before further neotectonic investigations of Coastal Cordillera.

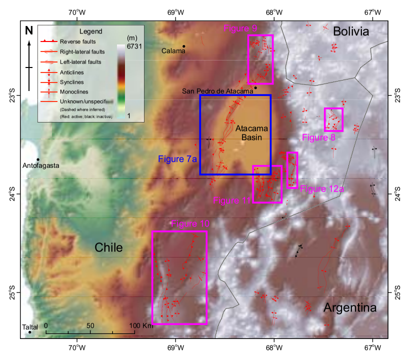

Figure 6. Unlike Coastal Cordillera, identification of possible active structures in Western Cordillera and Preandean Depression appears to have better constraint. Here we show an area with previously mapped active structures (the Atacama Basin, blue box) and five potential target areas for further investigations (pink boxes).

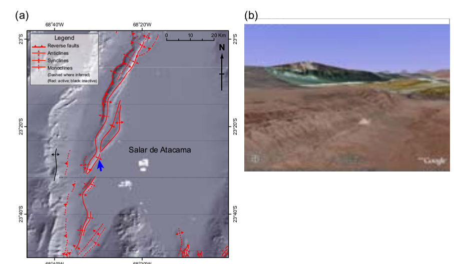

Figure 7. (a) Map of active structures in the Atacama Basin. A series of fault-propagation folds produced the approximately N-S trending ridge west of the Salar de Atacama in the basin. (b) A 3-D view of the western Atacama ridge from Google Earth. The view of this figure is shown as a blue arrow in (a). The age of the folded sediments, however, may be difficult to constrain, and may require other information such as seismic analysis of subsurface strata.

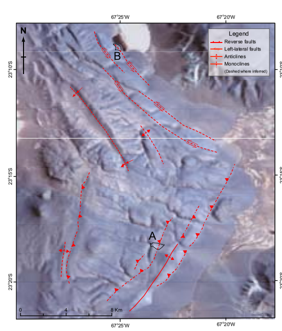

Figure 8. A detailed map of active structures of potential target area A. This area is located to the east of the Atacama Basin in Western Cordillera, and has a series of reverse faults, folds, and a left-lateral fault system in its northern part. Abandoned alluvial channel deposits (A) and alluvial fan deposits (B) may be potential dating targets to determine the ages and slip rates of the structures.

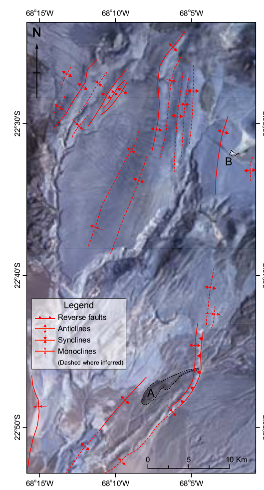

Figure 9. A detailed map of active structures of potential target area B. This area is located just north of the Atacama Basin, and has a series of folds that deformed the surface and drainage systems. A tongue-shaped lava flow (A) and lake deposits of a dammed river (B) may be potential dating targets to determine the ages and slip rates of the structures.

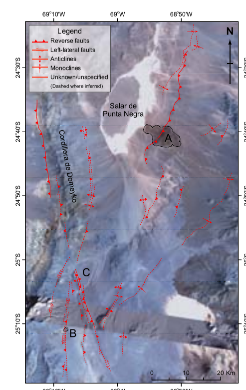

Figure 10. A detailed map of active structures of potential target area C. This area is located near the Salar de Punta Negra, south of the Atacama Basin at the southern end of Preandean Depression. The area has a west-vergent reverse fault system that borders the eastern side of the basin, and systems of reverse and strike-slip faults that run on both sides of the Cordillera de Domeyko. A lava dome (A) and a small cinder cone (B) may be potential dating targets to determine the ages and slip rates of the structures. The actively incising river system (C) may provide information of the growth of the folds.

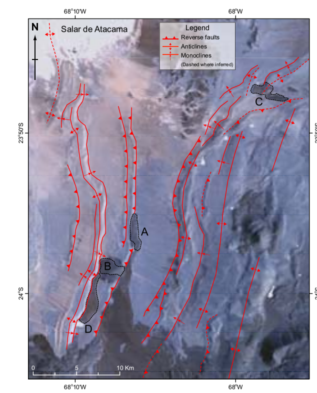

Figure 11. A detailed map of active structures of potential target area D. This area is located at the southeastern corner of the Atacama Basin, and has a series of reverse faults and related folds. An anticline appears to extend into the bed of the Salar de Atacama. Lava flows (A-C) and cinder deposits (D) may be potential dating targets to determine the ages and slip rates of the structures.

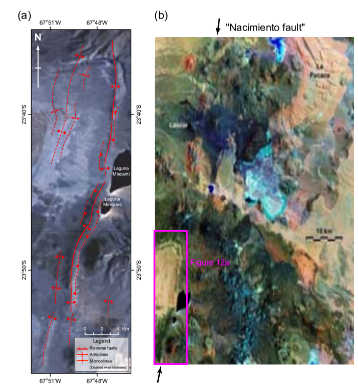

Figure 12. (a) A detailed map of active structures of potential target area E. This area is located just to the east of the Atacama Basin, and appears to be the only segment of the suspected "Nacimiento fault" that is most likely to be active. Along this segment, a series of reverse faults are producing an anticlinal ridge that dams the Laguna Miscanti and the Laguna Miniques. (b) Satellite image for the suspected "Nacimiento fault," taken from website of Randy Marrett (http://www.geo.utexas.edu/faculty/marrett/CentralAndes.htm). Although the "fault" appears as a prominent lineament in this image, we did not find a continuous active structure north of target area E.

REFERENCES

Allmendinger, R. W., G. Gonzalez, J. Yu, G. Hoke, and B. Isacks (2005), Trench-parallel shortening in the Northern Chilean Forearc: Tectonic and climatic implications, Geol. Soc. Am. Bull., 117, 89-104.

Dunai, T. J., G. A. Gonzalez Lopez, and J. Juez-Larre (2005), Oligocene-Miocene age of aridity in the Atacama Desert revealed by exposure dating of erosion-sensitive landforms, Geology, 33, 321-324.

Gonzalez, G., J. Cembrano, D. Carrizo, A. Macci, and H. Schneider (2003), The link between forearc tectonics and Pliocene-Quaternary deformation of the Coastal Cordillera, northern Chile, J. South Am. Earth Sci., 16, 321-342.

Neotectonic architecture, model, and the active Longitudinal Valley suture of Taiwan

J. Bruce H. Shyu[1], Kerry Sieh[1], Yue-Gau Chen[2], Ling-Ho Chung[2], Jean-Philippe Avouac[1], Yu Wang[1,2], Ray Y. Chuang[2], and Wen-Shan Chen[2]

1: Tectonics Observatory, California Institute of Technology; 2: Department of Geosciences, National Taiwan University

A. Neotectonic architecture and the tandem suturing model of Taiwan

Figure A1. Map of major active faults and folds of Taiwan (in red) shows that the two sutures are producing separate western and eastern neotectonic belts. Each collision belt matures and then decays progressively from south to north. This occurs in discrete steps, manifested as 7 distinct neotectonic domains along the western belt and 4 along the eastern. A particular assemblage of active structures defines each domain. For example, two principal structures dominate the Taichung Domain. Rupture in 1999 of one of these, the Chelungpu fault, caused the disastrous Chi-Chi earthquake. The black structure that runs between the Kaoping and Ilan Domains is the suture between forearc ridge and continental margin.

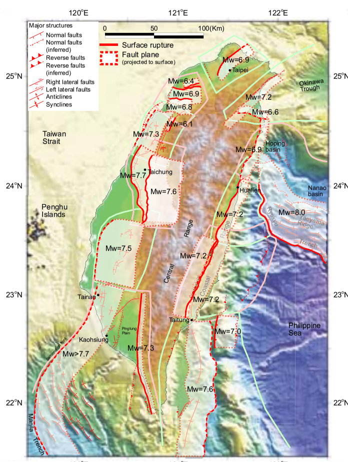

Figure A2. Proposed major sources for future large earthquakes in and around Taiwan. Bold red lines are proposed future ruptures, and the white patches are rupture planes projected to the surface. Here we have selected only a few representative scenarios to show in this figure. Earthquake magnitude of each scenario is predicted value from our calculation.

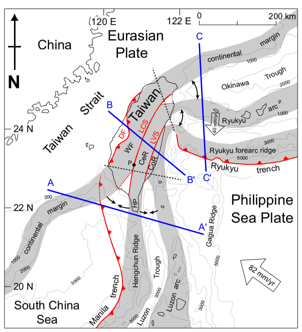

Figure A3. Taiwan is experiencing a tandem suturing of a volcanic arc and a sliver of continental crust to continental margin. In the south, the Luzon volcanic arc is converging on the Hengchun forearc ridge, which is, in turn, converging on the Chinese continental margin. Suturing of these three elements occurs in the middle of the island. In the north, both sutures are disarticulating, to form both the Okinawa Trough and troughs south of the Ryukyu island arc. Black dashed lines are the northern and western limits of the Wadati-Benioff zone of the two subducting systems, taken from the seismicity database of the Central Weather Bureau, Taiwan. Bold lines indicate cross-sections of Figure 4. DF: deformation front; LCS: Lishan-Chaochou suture; LVS: Longitudinal Valley suture; WF: Western Foothills; CeR: Central Range; CoR: Coastal Range; HP: Hengchun Peninsula; P: Outcrops of pillow lava along the western suture.

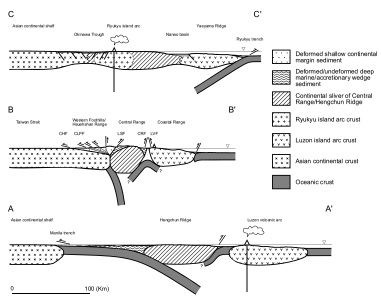

Figure A4. Three schematic crustal cross-sections across Taiwan illustrate three stages in the process of tandem suturing and disengagement. Locations of the sections are shown in Figure 3. A. Section just south of Taiwan shows the final stages of subduction and consumption of oceanic lithosphere between the three buoyant terranes. B. Section across central Taiwan shows relationship of the three terranes during suturing. C. Section north and east of Taiwan shows the subduction of the Philippine Sea plate and disengagement of the three terranes across the sutures. CHF: Changhua fault; CLPF: Chelungpu fault; LSF: Lishan fault; CRF: Central Range fault; LVF: Longitudinal Valley fault. No vertical exaggeration.

B. The Longitudinal Valley suture in eastern Taiwan: Characteristics of its major structures and the evolution of the suture

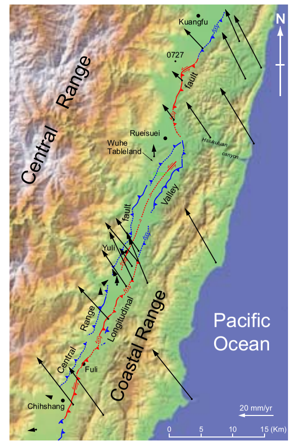

Figure B1. Map of major structures in the middle part of the Longitudinal Valley. The Longitudinal Valley fault is an east-dipping, obliquely slipping reverse fault, along which the Coastal Range is rising rapidly and moving toward the Central Range. The less prominent Central Range fault is a west-dipping reverse fault, above which many fluvial terraces and the Wuhe Tableland are rising slowly. Faults that ruptured during the 1951 earthquakes are colored red. Major faults and flexures that did not rupture in 1951 but are known to be active are colored blue. Black arrows are GPS vectors for the period 1993 to 1999. Motions are relative to station 0727, about 7 km southwest of Kuangfu. The differences between vectors indicate shortening across the valley of about 40 mm/yr.

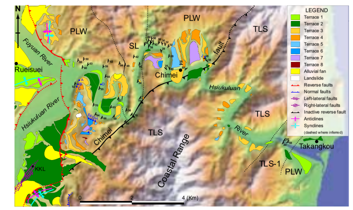

Figure B2. Since the Hsiukuluan River is the only river that flows across the Coastal Range, it provides a unique opportunity to determine the long-term rates of uplift of the range. Along the western part of its course across the range, the river has formed four deeply incised meander loops. As many as eight levels of fluvial terraces exist on both sides of the river valley. PLW: sedimentary Paliwan Formation; SL: Shuilien Conglomerate Member of the Paliwan Formation; TLS: volcanic rocks of the Tuluanshan Formation; TLS-1: a thick layer of volcanic breccia within the Tuluanshan Formation. Dark blue dots indicate where the thickness of the fluvial terrace deposit was directly measured.

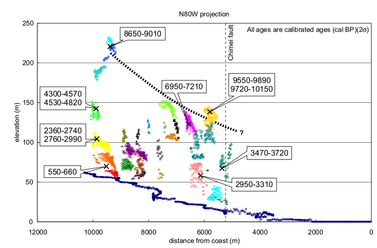

Figure B3. Preliminary correlation of river terraces along Hsiukuluan canyon. Each different color represents a different level of terraces. Solid dots represent terrace surface measurements from the DEM, and short bars represent terraces straths, measured by laser range finder. Blue dots indicate the river profile of the Hsiukuluan River. All of the terraces and the river profile were projected on to the plane in local dip direction of the bedrocks (N80W). All ages are calibrated ages (2σ), in cal BP. Our dating results and the correlation of the terraces suggests that the uplift rate of the westernmost Coastal Range is highest currently, and decreases to the east.

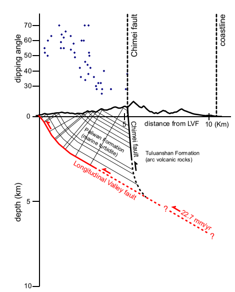

Figure B4. Reconstruction of the subsurface geometry of the Longitudinal Valley fault near Hsiukuluan canyon, from bedrock dip angles. The azimuth of the section is approximately N80W. This model indicates that the dip-slip rate along the fault is about 22.7 mm/yr and that all of the deformation is accommodated by the slip along the fault plane, with no internal deformation of the beds.

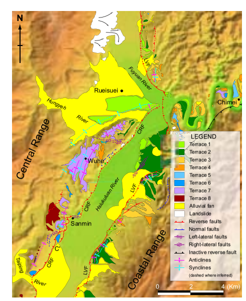

Figure B5. Detailed map of geomorphic and neotectonic features on and around the Wuhe Tableland shows deformations by young anticlines extending 13 km between the Fuyuan and Taiping Rivers. A syncline in young sediments flanks the anticlines on the northwest. These folds are formed in the hanging-wall block of the west-dipping Central Range fault (CRF). The Wuhe Tableland is a patch of uplifted lateritic fluvial terrace on the crest of a major anticline. A deformed lower and younger fluvial terrace shows that the fold extends nearly 2 km northeast of the tableland and may plunge beneath the Longitudinal Valley fault (LVF). Lateritic fluvial strath terraces along the eastern flank of the Central Range and a bedrock ridge show that the anticlines extend several kilometers southwest of the tableland.

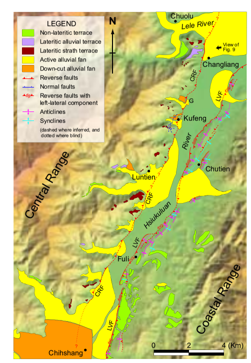

Figure B6. Detailed map of geomorphic and neotectonic features between the Lele River and Chihshang. As to the north, numerous uplifted lateritic strath terraces and deformed alluvial fans along the eastern flank of the Central Range indicate that the Central Range fault (CRF) is present along the western edge of the Longitudinal Valley. Fluvial terraces and neotectonic landforms of the east-dipping Longitudinal Valley fault (LVF), along the eastern side of the Longitudinal Valley, are also shown in the figure.

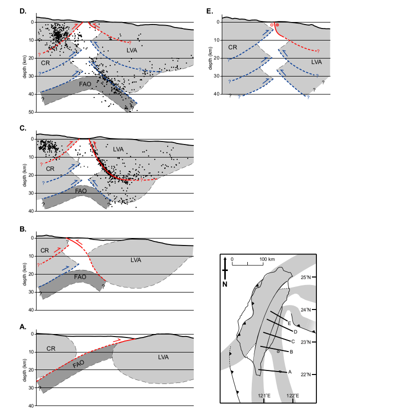

Figure B7. Schematic crustal cross-sections show our hypothesis for the evolution of the Longitudinal Valley suture. Each section is drawn using current topography and observations along the lines specified on the index map, with no vertical exaggeration. Red indicates the youngest and currently active faults in each time frame, and blue indicates older faults, which may still be active. Faults are dashed where inferred. (a) Before suturing, the Luzon forearc oceanic lithosphere (FAO) subducts beneath the Central Range continental sliver (CR). This is currently occurring at about the latitude of the southern tip of Taiwan, about 22ºN. (b) As the Luzon volcanic arc lithosphere (LVA) approaches the Central Range, an east-dipping thrust fault appears, allowing the FAO to also subduct underneath the LVA. Contemporaneously on the west side of the valley, the proximity of the LVA to the CR induces formation of a newer, shallower west-dipping thrust fault above the original one. This is the current structural geometry near the southern end of the Longitudinal Valley, between about 22º40'N and 22º50'N. (c) As the suture matures, the two non-oceanic lithospheric blocks both start to thicken by evolving multiple reverse-fault wedges, with the younger ones at shallower depth. This is the current structural geometry at the latitude of Chihshang, about 23º10'N. (d) At the latitude of the Wuhe Tableland, about 23º30'N, the suture is nearing maturity. The suture has evolved into a "Christmas tree" shape, with a thick pile of sediments between the two non-oceanic lithospheric blocks and underlain by the subducted forearc oceanic lithosphere. (e) In northern Longitudinal Valley, at the latitude about 23º45'N, the dominantly sinistral Longitudinal Valley fault appears to be the only major active structure. The west-dipping Central Range fault has become inactive, and sediments in the Longitudinal Valley are lapping on the eastern flank of the Central Range.

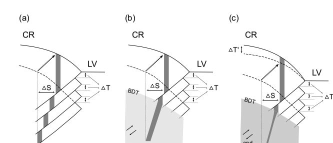

Figure B8. Cartoons show possible scenarios of crustal thickening (ΔT) and shortening (ΔS) produced by slip along the Central Range fault and by other processes. Dark gray bar indicates an originally vertical reference band. Bold dashed arrow indicates the direction of material movement. CR: Central Range; LV: Longitudinal Valley; BDT: brittle-ductile transition. (a) The Central Range fault system continues to depth, and brittle slip along the fault is responsible for all shortening and crustal thickening. (b) The Central Range fault system transforms down dip at the brittle-ductile transition into a ductile zone, where shortening and crustal thickening are accomplished by ductile simple shear. (c) Deformation occurs as in (b), but additional shortening and crustal thickening occur beneath the Central Range by pervasive pure-shear processes, which produce an arching of the upper crust (ΔT').

Acknowledgments

We greatly appreciate the assistance of C.-H. Chen, Y.-C. Chen, L.-H. Chung, C. Huang, S.-H. Huang, P.-N. Li, T. Watanuki, Y. Wang, B.C.-C. Yang, and I.-C. Yen in the field and are grateful for valuable discussions with O. Beyssac, Y.-C. Chan, H.-H. Chen, H.-T. Chu, M.-L. Hsieh, J.-C. Lee, W.-T. Liang, M.-S. Lin, R.-J. Rau, M. Simons, C.P. Stark, and S.-B. Yu. Also, we have benefited from stimulating discussions with the students of three multinational Ge122 field classes in Taiwan and a neotectonic seminar at National Taiwan University. Y.-J. Hsu and Y.-M. Wu generously provided us with their GPS and seismicity data along with valuable comments. We are grateful for financial support for our project in Taiwan from the Gordon and Betty Moore Foundation, NSF, and the Central Geologic Survey, Taiwan.

September 29, 2006

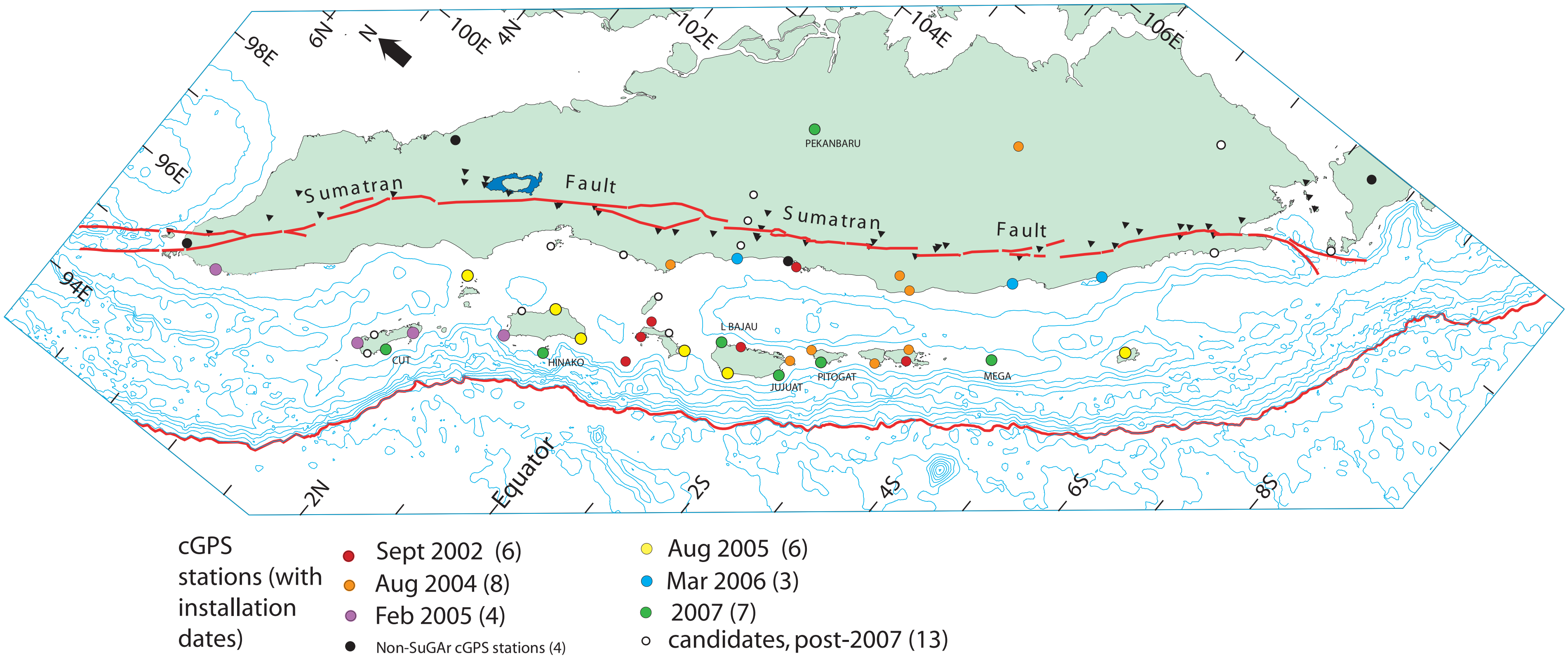

EDUCATIONAL OUTREACH in WESTERN SUMATRA

Catharine Stebbins and Kerry Sieh, Tectonics Observatory, Caltech, Pasadena, CA 91125;
Danny H. Natawidjaja and Bambang W. Suwargadi, LIPI, Bandung, Indonesia

Sumatran Project long-term Educational Outreach goals

- Produce updates of these materials as new data becomes available from GPS and coral studies
- Continue distributing posters and data sheets in the communities where research is conducted
- Provide these materials to local community groups who may find them useful in developing their own education, hazard mitigation and response plans.

2007: Going Forward

KOGAMI, a local volunteer organization based in Padang, Sumatra, has requested our Educational Outreach materials for use in their community education and hazard mitigation plans that reach the 700,000+ population of the city. The international relief organizations Mercy Corps, Geohazards International and USAID, have also requested our materials to distribute and use in their programs in Indonesia.

Through these collaborations our outreach materials will reach a much broader audience than Sumatran Project researches can access during field seasons. Providing print-ready files directly to these organizations will give them the flexibility to produce the posters on an as-needed basis.

October 2002
Sumatran Plate Boundary Project Educational Outreach

Using information provided by the Caltech and Indonesian research team and colleagues, plus feedback from people in the GPS instrumented areas, we proposed a public information poster and accompanying brochure, which address in layman's terms, the tectonic environment of coastal West Sumatra.

January 2003
Materials development

The poster is printed in English, Indonesian and Mentawai to reach the largest possible audience. The design is dense and colorful and geared toward a 6th grade level of understanding, in order to appeal to a broad range of people. The posters are meant to capture the attention and imagination, and to be studied over time.

A numbered question and answer format was used to create a conversational style appropriate to the informal nature of the presentation. This allows the viewer to look at each question separately and come back to the poster many times, each absorbing the information at their own pace.

We intend to use results from new data in future versions, developing additional posters for areas along the Sumatran Megathrust, including coastal West Sumatra.

School children on Tello Island learn about earthquakes and tsunamis, July 2004

July 2004
Mentawai Islands Poster v1 & 1.2

During the summer 2004 research field season several thousand copies of our first Educational Outreach poster were distributed in schools, churches, and to community leaders throughout the Mentawai Islands. Citizens of the islands requested more information so we began developing Mentawai Islands poster v1.2 and Nias/Simeulue Islands poster v1.1.

Mentawai Islands Poster v1.2

Mentawai Islands Poster v1

December 26, 2004
M 9.1 Aceh-Andaman Earthquake occurs off the West coast of Northern Sumatra

Press interviews with survivors make it clear that people in the affected areas had little knowledge of how to prepare for, or respond to this type of catastrophic event, confirming the need for continuing earthquake and tsunami science education in the entire region.

Lewak coral after December 2004

March 2005
Nias/Simeulue Islands poster v1.1

Building on positive feedback from recipients of the Mentawai Islands poster, our first for Nias and Simeulue islands is ready for distribution the day of the March 28, 2005 earthquake. The posters will be distributed during follow-up field research and we immediately begin planning v1.2. Because of the recent earthquakes, we change the focus in this poster from describing the general tectonic processes to showing what actually happened during and after the December 2004 and March 2005 events.

Nias/Simeulue Islands poster v1.1

March 28, 2005
M 8.7 Nias/Simeulue Earthquake occurs off the West coast of Northern Sumatra.

Nias/Simeulue Islands poster v1.2

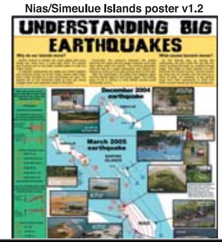

April 10, 2005
M 6.7 Mentawai region earthquake occurs, East of Siberut Island and West of Padang, Sumatra

April 2006
Nias/Simeulue Islands poster v1.2
GPS Station Data Sheets

Prototype GPS Station Data Sheet

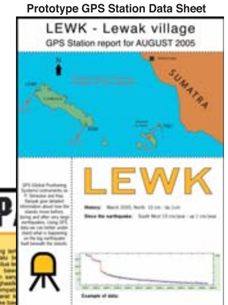

With **Nias/Simeulue Islands poster v1.2** we use photographs and area maps to show where post earthquake subsidence and uplift was measured, and how the surrounding Banyak and Batu islands were affected.

GPS station locations and data are added, describing the sinking and springing up process in more detail than in earlier versions of the posters. At this time we introduce a new outreach component, the one page **GPS Station Data Sheet** handout. Many people still misunderstand the purpose of the twenty seven GPS Stations located throughout the islands and Sumatra. They also want to know what the data show and how it might relate to them. We use the handouts to address these questions and present the data to people in communities where the stations are located. The first data sheets will be distributed early in 2007, and yearly thereafter.

October 2006
Coastal West Sumatra poster v1

For distribution in the densely populated urban centers of central West Sumatra as well as the adjacent islands, in this poster we address the likelihood that an earthquake and tsunami will occur in this region within the lifetimes of most young people living on the coast today. In particular, we describe possible tsunami scenarios and reference the historical events of 1797 and 1833 to provide context. We also show what to expect afterward and list local contacts for preparedness information.

Coastal West Sumatra poster v1

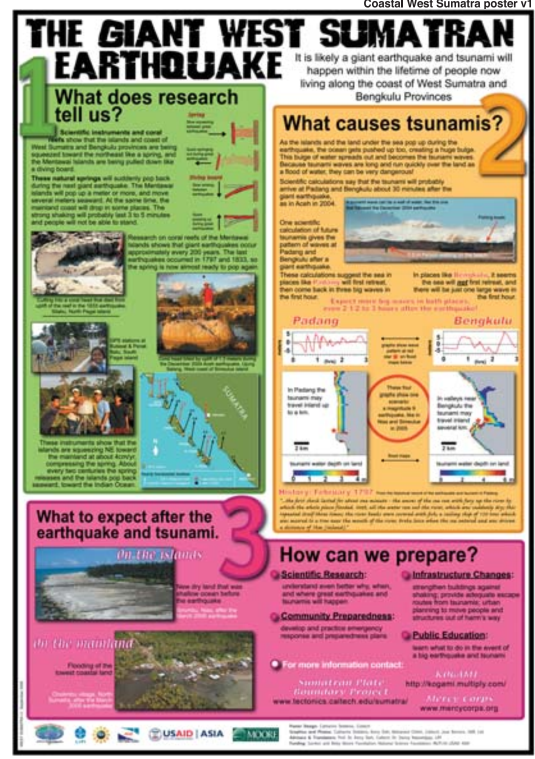

Assimilation of Plate Tectonic Reconstructions into Geodynamic Flow Models

Mark Turner, Mike Gurnis, Lydia Taylor, Vlad Manea, Sonja Kisin
Caltech, Tectonics Observatory

Dietmar Muller, Maria Sdrolias
University of Sydney, School of Geosciences

Introduction

One of our goals is to attempt to place the tectonics of individual boundaries within a global context and to understand the broader scale forces driving the deformation. There are a host of unsolved questions surrounding the causes for changes in plate motions, including the initiation of new subduction zones. In order to address these question, the CTO has been developing an entirely new generation of tools that are computationally advanced while being consistent with the actual structure and kinematics of plate boundaries. Thus far, we have made considerable progress in this direction. One goal is to assimilate plate tectonic reconstructions into global and regional geodynamic models. With the University of Sydney in Australia and the Geological Survey of Norway, the TO has been a key partner in the development of GPlates, a plate tectonic reconstruction software package. We are using GPlates as the preprocessing front end to global models of mantle convection using the CitcomS finite element code.

Using GPlates, we have developed a method for representing the evolving geometry of tectonic plates. A single plate is represented by all of the margins around the plate, reconstructed according to the euler pole of the margin, and an algorithm for computing the intersections of all of the margins. The end result is a complete evolving description of the surface of the earth without any blank spaces -- an essential prerequisite for merging dynamic models with paleo-reconstructions. We have used this software to build a global set of plates over the last 80 million years, to merge these "dynamic" plate polygons with paleo age grids, and to assimilate this data into global circulation models of the mantle. This work has given the CTO a new tool that allows us to explore the dynamics of changes in plate motions and shapes over the next several years. We are now routinely running this software on the CITerra supercomputer.

Typical Workflow Assimilating Data into Models

Data, Software & Hardware	Tectonic feature database (ridges, trenches, fractures, etc)	GPlates run on desktop	CitcomS run on CITerra
Actions & Operations	Multiple data sets, corrected, and merged with Python scripts →	Users create plate polygons and export velocity →	Postprocessing and analysis with Python scripts and GMT

GPlates: Software for Tectonic Reconstructions

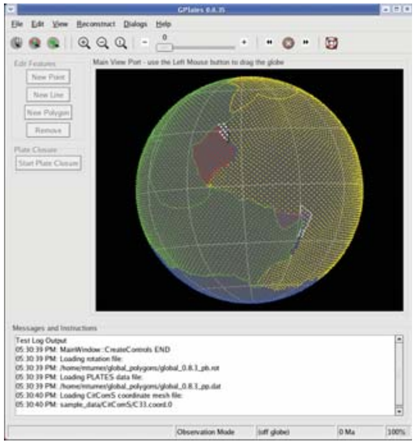

The GPlates main window has a central globe for display, controls for creation and editing of tectonic feature data, and tools for performing reconstructions and animations. Most feature data may be exported as simple GMT xy files. When combined with a CitcomS mesh, GPlates can export surface velocity vectors for each mesh point.

An idealized tectonic plate showing component margin line data features. Each line feature has its own euler pole and rotates according to the rules of plate tectonics.

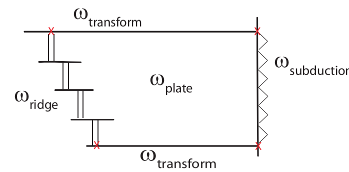

The user selects line features to create a closed plate polygon. GPlates automatically calculates the intersection points (shown as red x's) to form the complete plate polygon boundary.

Upon each reconstruction all lines rotate independently, and GPlates automatically recomputes the new plate boundary to keep the polygon closed and consistent.

The table below shows a typical plate polygon with its component margins: the IndoAustralian plate from the present day back to five million years ago.

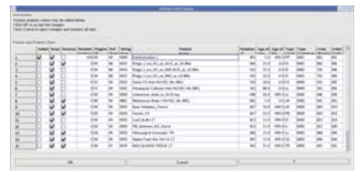

CitcomS: Mantle Convection Models

The plate tectonic reconstructions are assimilated into models of mantle convection solved with the finite element package CitcomS.py, developed at Caltech. CitcomS solves for conservation of mass, momentum and energy:

(1) $\nabla \cdot \vec{u} = 0$

(2) $\nabla \cdot \sigma = \rho_0 \alpha (T - T_0) \vec{g}$

(3) $\frac{\partial T}{\partial t} + \vec{u} \cdot \nabla T = \kappa \nabla^2 T + H$

where *u* is velocity, σ is the stress tensor, *P* is dynamic pressure, η is dynamic viscosity, *T* is temperature, κ is thermal diffusivity, *H* internal heat and *g* is the gravitational acceleration.

These equations are solved with CitcomS.py [Tan et al., 2006] with the finite element. The model domain is a spherical shell representing the entire mantle and lithosphere. CitcomS.py uses a decomposition scheme such that the spherical shell is first decomposed into 12 caps so that in map view the elements are approximately equal area over the entire surface of the sphere. Then each cap is further divided such that the edges of the cap are equally divided.

Orthographic projection of processors from a full CitcomS mesh in which there are 16 processors in map view for each cap. The CitcomS cap is shown as distinct colors while the processor domains within the caps are indicated by the intensity of the color.

This example was produced for a run with 2 processors in radius such that the total number of processors was 12x16x2=384. This is the largest model we have solved for on the CitTerra machine so far, and most of the cases have been solved with 96 processors with 128x128 elements in map view for each processor.

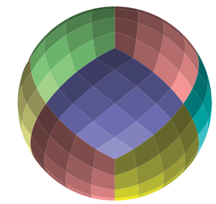

References:
Tan, E., E. Choi, P. Thoutireddy, M. Gurnis, and M. Aivazis, GeoFramework: Coupling multiple models of mantle convection within a computational framework, Geochemistry, Geophysics, Geosystems, 7, Q06001, doi:10.1029/2005GC001155, 14 pp., 2006.

Global Models with Polygons, Age Grids, and Convection

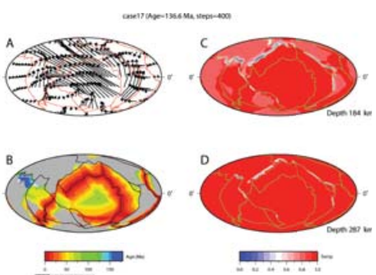

Model results incorporating the global closed plate polygons from 80 Ma to the present. The models are incorporated such that the 80 Ma reconstruction and age grid is imposed on the CitcomS model from 160 Ma to 80 Ma.

Results after 400 time steps, at '136 Ma', are shown on the left. Shown are (A) the imposed velocity field and closed polygons from GPlates, (B) the paleo-age grid, (C) the temperature field at 184 km, and (D) at 287 km.

We then show the results close to the present day (at 3 Ma) on the right. Shown are the (A) Paleoage grid, (B) temperature at 205 km depth, (C) at 410 km, and (D) at 964 km.

Early cases such as these have pointed toward the need for
(i) higher resolution, (ii) more realistic initial conditions,
(iii) closed plate polygons that extend to times earlier than 80 Ma,
(iv) more realistic rheological models for subduction boundaries.

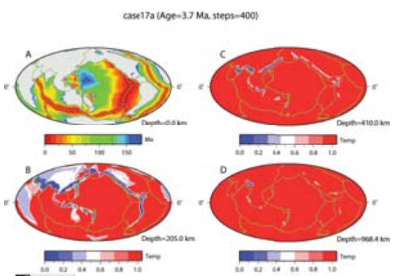

Assimilation of Age Grids

We have been developing a new method by which the paleo age grids are assimilated into the flow models. We have explored a method by a thermal model for the conductive cooling of the oceanic lithosphere (a half-space model), is used

$$T_e(z,\tau) = T_s + (T_m - T_s)\,\mathrm{erf}\left(\frac{z}{2\sqrt{\kappa\tau}}\right)$$

where Te is the expected temperature, Ts is the surface temperature, Tm is the mantle temperature, z is depth, K is the thermal diffusivity, and tau is the age of the oceanic lithosphere from the age grid. We attempt to conform the thermal structure within CitcomS to this thermal model for depths less than da, the assimilation depth. At each new time-step

$$\gamma = \frac{z}{2d_a} \qquad \text{if } z < d_a$$

$$T(z,t) = (1-\gamma)T'(z,t) + \gamma T_e(z,\tau)$$

where γ is the depth-dependent assimilation factor and T' is the temperature after the temperature is updated in the normal way by the solution of the energy equation.

In the figure on the right we show how this depth-dependent assimilation affects a simple model of cellular convection using the same set of parameters that we used in the global models, i.e. same Rayleigh number, d_a, age distribution, and resolution. What we find is that if d_a is too close to the thickness of the oceanic lithosphere for a given age, τ, then subduction is cut-off.

On the left is the temperature field for the entire model domain, while on the right we zoon in on the upper thermal boundary layer for three time steps, including the initial condition. In the contour plots on the right, we see the expected temperature contoured in green and the temperatures from CitcomS using d_a=0.005 (32 km).

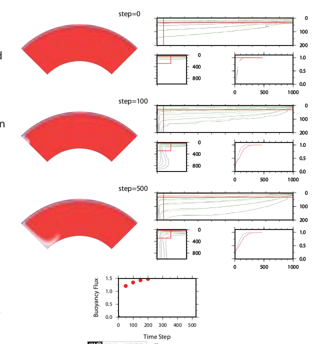

Low Viscosity Wedges

The details of plate margins, especially the introduction of low viscosity wedges (LVWs), can have a substantial influence on the dynamics of subduction zones.

These models show a method we have developed to simulate the weakening of mantle wedge by way of the dehydration of subducted oceanic crust. It relies on tracking the oceanic crust after it has subducted by way of tracers and then lowering the viscosity of the mantle above the crust in terms of pressure and distance from the trench. The method has been incorporated into the regional version of CitcomS. The models shown are effectively 2-D but the method works in 3-D as well.

In the figures at right, the oceanic crust is shown in Blue on top of the temperature field. In the case shown in (a) there is no mantle wedge and the oceanic lithosphere has been advectively thickened below the over-riding plate.

The only difference in the model shown in (b) is the incorporation of a LVW such that the viscosity between a depth of about 40 km and 300 km has had its viscosity reduced by one order of magnitude. The excessive advective thickening has vanished, the slab dips at a steeper dip into the mantle, and the slab penetrates to a greater depth into the mantle for an equal interval of time.

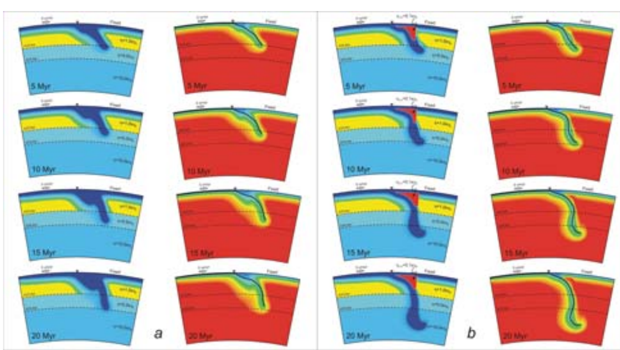

Incorporation of Asymmetric Plate Boundaries from GPlates into CitcomS

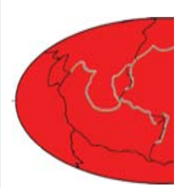

We have been able to complete the workflow from subduction zones, including their polarity from the plate tectonic reconstruction (GPlates) and merged with CitcomS (shown at left). We are currently refining the procedure.

Shown at left is an image of the material type before incorporation into CitcomS as a raster image from red (normal) to blue (weak plate boundaries). GPlates distinguishes between the closed plate polygon (black lines) and the subduction boundaries (green lines).

These material types are then processed by CitcomS with the other controls on the viscosity (pressure and temperature) to create the viscosity shown at right, with the three cross-sections with the low viscosity wedges shown as the deepest red.

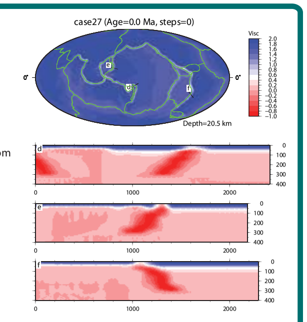

Evidence for large Moho offset in Southern California from Receiver Functions

Zhimei Yan & Robert W. Clayton

Abstract

Large offsets on the Moho are imaged among the back-azimuthal grouped Receiver Function (RF) beneath several stations in Southern California. Some of them correlate very well with the surficial geologically mapped faults, such as station TA2 on the San Andreas Fault (SAF), some of them occur in places where no surficial major faults exist, such as station DAN in Fenner Valley, Mojave Desert. Combined with synthetic RF waveform modeling, a notch structure is inferred on the eastern San Gabriel Mountains, where Moho shallows from 38 km north of the SAF, 34 km south of the San Gabriel Fault to ~29 km in between beneath the Mt. Baldy block.

Examples of large offset on the Moho

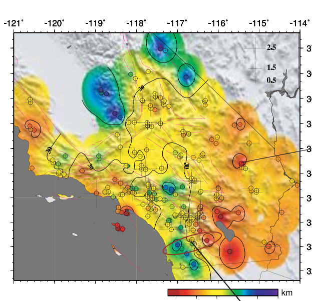

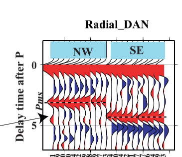

Moho Depth result
NW: 21.7 [20.7 22.6]
SE: 32.2 [30.7 33.7]

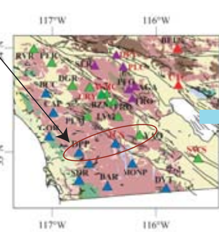

At station DAN in the Mojave Desert, a large Moho offset of ~10 is inferred. At station JCS, which locates on the Elsinore Fault, large Pms of 4.5 sec is observed for the RFs from West, while small Pms arrival of 3 sec is observed for events from SE. The large Moho offset here is confirmed by the two nearby stations DPP and YAQ.

RFs

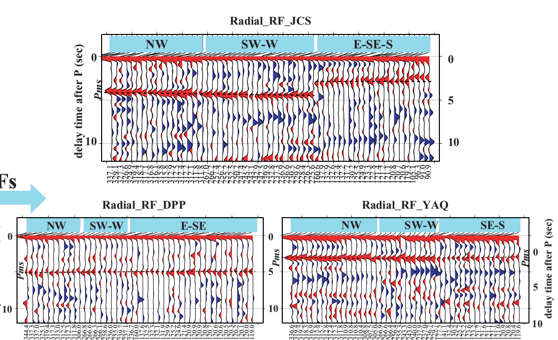

More evidence in the San Gabriel Mountains

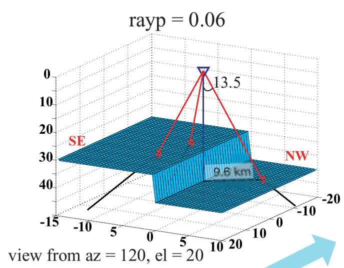

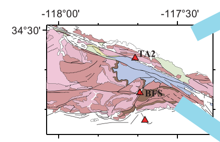

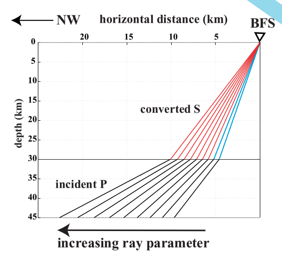

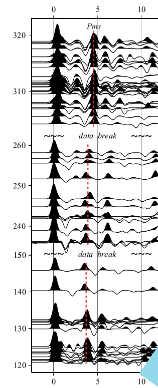

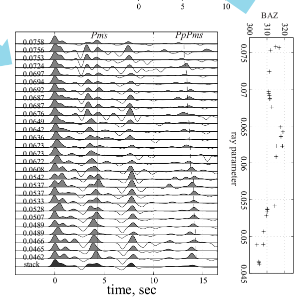

Data Summary

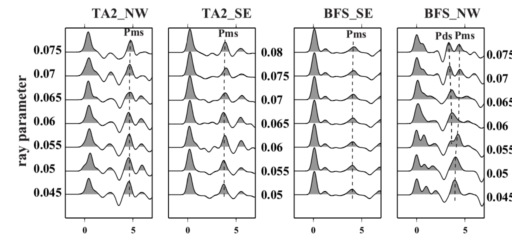

Synthetic Waveform modeling

Notch on the Moho

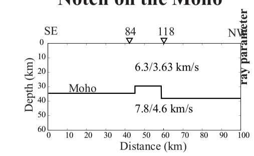

Step on the Moho

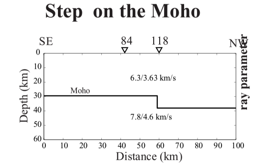

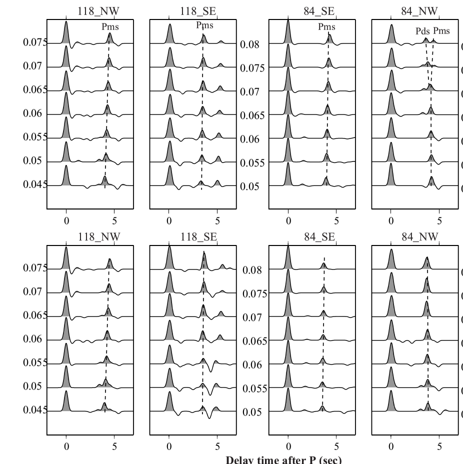

Summary

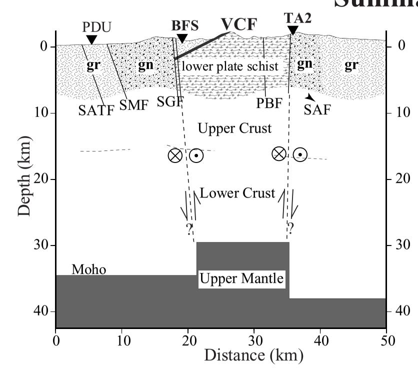

Synthetic waveform modeling for the anomalous features in the receiver functions for two stations (TA2 and BFS) in the eastern San Gabriel Mountains indicates that a notch structure exists on the Moho, where the Moho shallows from 38 km north of the SAF, 34 km south of SGF to ~29 km beneath the Mt. Baldy block. The shallow Moho correlates very well with the surifcial exposure of the lower plate Pelona Schist or places where the schist resides at very shallow depth. This is either related to the strike-slip movements along the two major faults or caused by differential uplifting.

Simulated Nonlinear Response of High-rise Buildings for the 2003 Tokachi-oki Earthquake Mw8.3

California Institute of Technology Civil Engineering
Jing Yang jingy@caltech.edu
Thomas Heaton heaton_t@caltech.edu
John Hall johnhall@caltech.edu

1. Introduction

Seismic waves from large subduction earthquakes are rich in long periods waves that may be especially large in regions with local site amplification. The long-term global goal of our research is to investigate how well-designed modern high-rise buildings may perform in giant subduction earthquakes (e.g. Cascadia). Towards this goal, we are studying the Tokachi-oki 2003 earthquake (Mw8.3) which is the largest well recorded earthquake till now and was recorded by 276 strong motion stations located in Hokkaido Island. We use records from these stations to simulate the fully nonlinear seismic responses of 6- and 20- story steel moment-frame buildings designed according to both the U.S. 1994 UBC and also Japanese building code published in 1987. We consider buildings with both perfect welds and also with brittle welds whose fracture characteristics are similar to those observed in the 1994 Northridge earthquake.

From this research, we find that although Japanese code buildings are stronger, they are also stiffer which tends to increase the global forces experienced by Japanese buildings by more than 20% compared with U.S code buildings. The net effect is that when considering collapse potential, the Japanese buildings can sustain motions about 6% larger than the U.S. buildings. Moreover, our simulations indicate the building would have been strongly excited throughout the coastal region, with the potential for collapses in some locations.

2. The 2003 Tokachi-oki Earthquake Mw8.3

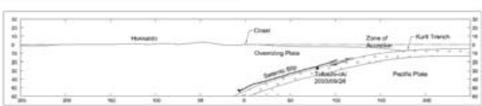

Figure 1: Cross section of the approximate geometry of the rupture surface with respect to the island of Hokkaido. This event occurred on the main subduction interface of the highly active Kuril trench. The Pacific plate is subducted toward N60 W beneath Hokkaido region at a rate of about 8 mm/year.

Table 1: Summary of maximum values for ground motions

	Maximum peak-to-peak value	Location
Ground Acceleration	1622 cm/s²	HKD100
Ground Velocity	157 cm/s	IBUH03
Ground Displacement	88 cm	HKD098
Pseudo Acceleration of Response spectra (5% damping) at 1.5 sec (natural period of U6)	1422 cm/s²	TKCH07
Pseudo Acceleration of Response spectra (5% damping) at 3.5 sec (natural period of U20)	452 cm/s²	HKD098

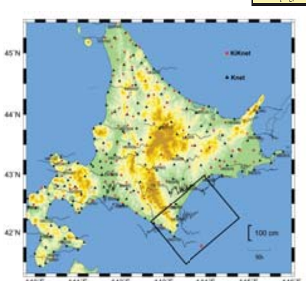

Information about this event:
Epicenter Depth: 27 km
Distance: 80 km east-south east of Cape Erimo, Hokkaido
Strike, dip, rake =230°, 20°, 109°
Source duration: 40 sec
Maximum slip: 5.8 m
Average slip: 2.6 m

Figure 2: The radial components of ground displacements for selected stations. We use the method of Boore (2001), combined with GPS data, to best determine the static displacements for selected stations.

3. Computational Models

We use Frame 2-D, a finite element method based on a fiber-element model that includes both material nonlinearities as well as geometric nonlinearities.

Steel Moment-Frame Building Models (symmetric):
Heights: 6-story and 20-story buildings (plus one basement)
Design Codes: 1994 UBC at seismic zone 4 and Japanese building code (1987)
Welds conditions: brittle (prone to fracture) and perfect (won't fracture)

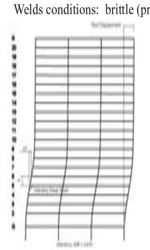

Figure 3: Definitions of the response parameters.

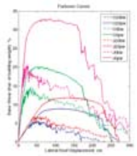

Figure 4: Pushover curves for 6-story and 20-story buildings. This analysis measures the actual strength of buildings. We can find that Japanese buildings are stronger than U.S. buildings and the presence of brittle welds significantly decreases the strength of a building.

Table 2: Property values for the building models

Building Type	U20	J20	U6	J6
Natural Period	3.5 sec	3.05 sec	1.5 sec	1.17 sec
Base Shear Yield Force (fraction of building weight) %	pw: 8.9 bw: 5.9	pw: 11.8 bw: 7.1	pw: 21.5 bw: 15.2	pw: 32.7 bw: 20.6

4. Simulated Nonlinear Responses

All eight buildings models were considered to locate at each station. The summary of their maximum response parameters are listed in table 3. The contour map of the maximum inter-story drift for the US-code 20-story buildings assuming brittle welds is shown in Figure 6.

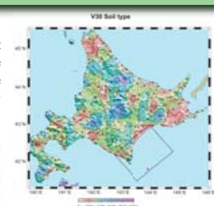

Figure 5: The distribution of average shear wave velocity of soil down to 30 m in Hokkaido area. By comparing with the soil type building response distribution, we see that basins amplify the response of high-rise buildings even far away from the epicenter.

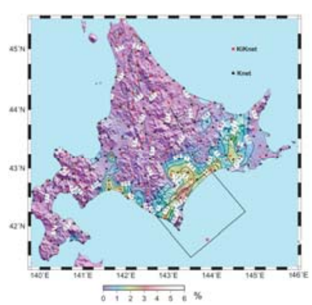

Figure 6: Maximum inter-story drift (in percent) for the U20 (20-story steel frame designed to UBC94) with brittle welds (bw). The maximum value is 3.84% and occurred at HKD098.
Notice the buildings located in the northeast and the south-west regions in Hokkaido will suffer strong shaking although they are almost 200 km away from the epicenter.

Table 3: Summary of responses for each type of buildings

Response	Building Type	Maximum Value	Location
Inter-story drift	U20 bw (brittle welds)	3.84 %	HKD098
	J20 bw	3.35 %	HKD098
	U6 bw	5.53 %	TKCH07
	J6 bw	4.75 %	IBUH03
Roof displacement	U20 bw	93 cm	HKD098
	J20 bw	103 cm	HKD098
	U6 bw	79 cm	TKCH07
	J6 bw	75 cm	IBUH03
Fracture welds	U20 bw	38 %	IBUH03
	J20 bw	36 %	IBUH03
	U6 bw	55 %	IBUH03
	J6 bw	58 %	IBUH03
Inter-story drift	U20 pw (perfect welds)	2.09 %	HKD098
	J20 pw	2.51 %	HKD098
	U6 pw	4.00 %	TKCH07
	J6 pw	2.77 %	TKCH07
Roof displacement	U20 pw (perfect welds)	129 cm	HKD098
	J20 pw	144 cm	HKD098
	U6 pw	70 cm	TKCH07
	J6 pw	49 cm	TKCH07

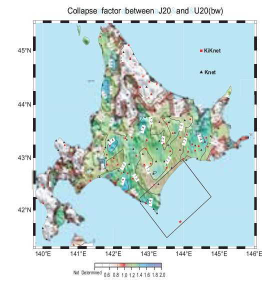

Figure 8: Collapse factor ratio between J20bw and U20bw. The white color shows where the collapse factor is too large to be of interests. As expected, in most areas, J20 is safer than U20 and the ranger is from 1 to 1.4. However for stations close to collapse, the difference between collapse factors for two codes is only 6 %, which is much smaller than the 20% difference in strength of buildings.

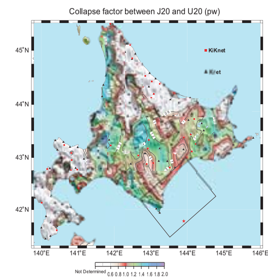

Figure. 9. Collapse factor ratio between J20pw and U20pw. The ratio at HKD098 is 1, which means that the collapse factors for J20pw and U20pw are exactly the same. Unlike figure. 8. in some strongly shaken areas, collapse factors of J20pw are even smaller than that of U20pw.

5. Collapse Factor

We introduce a new parameter named the "collapse factor" to describe the collapse possibility associated with simulated buildings. This safety factor is defined to be the scalar multiplier of the recorded ground motion that is required to cause collapse of the simulated building.

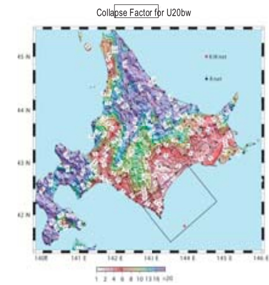

Figure 7.

Figure 7: Collapse factor for U20bw. Although no buildings shown collapse in these simulations, increasing the amplitude of station HKD098 by only 6 % caused simulated collapse for U20bw. This is well within the uncertainty of this type of calculation.

6. Future Work

We plan to simulate strong ground motions of the 2004 Sumatra earthquake by considering the strong motion recordings from the 2003 Tokachi-oki earthquake as empirical Green functions. Simulation the broad-band teleseismic body waves in the frequency band of interest is important for providing constraints on the strong motion simulation.

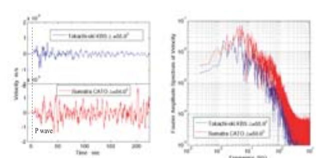

Right figure 10 show the teleseismic body waves velocities and their freuqncy contents for 2003 Tokachi-oki and 2004 Sumatra earthquakes.

7. Conclusions

- The long-period ground motions recorded in the 2003 Tokachi-oki earthquake would have caused large inter-story drifts in 20-story flexible steel moment-resisting frame buildings designed according to both current U.S. and Japanese building codes.
- Although Japanese buildings are 20%~30% percent stronger than U.S. buildings, their capacity to resist collapse does not proportionally increased. Japanese buildings with brittle welds can sustain motions only 6% larger than corresponding U.S. buildings for station with significant collapse potential. And in some areas, Japanese buildings with perfect welds can sustain motions even smaller than U.S. buildings.
- Local soil geology plays an important role in the performance of high-rise buildings. Some basin areas which locate more than 200 km away from the epicenter amplify the long period motions large enough so that one could expect irreparable damage for 20-story buildings.
- The fracture of welds in the connections of beams and columns would dramatically reduce the strength of the buildings as

ACKNOWLEDGEMENT:
We thank the Tectonics Observatory funded by the Moore Foundation. Data from NIED